

Long-range surface plasmon polariton active structures  
based on optically-pumped dye-doped polymer gain media

by

Elham Karami Keshmarzi, M.A.Sc

A thesis submitted to the Faculty of Graduate and Postdoctoral  
Affairs in partial fulfillment of the requirements for the degree of

Doctor of Philosophy

in

Electrical Engineering

Ottawa-Carleton Institute for Electrical and Computer Engineering

Carleton University  
Ottawa, Ontario

© 2017, Elham Karami Keshmarzi

## Abstract

Solid state organic gain medium using optically-pumped dye molecules doped in a polymer host is considered as the top cladding of a long-range surface plasmon polariton (LRSP) structure to enable active plasmonic devices with interesting applications operating in the near-infrared.

The gain media is a thin film of PMMA (poly (methyl methacrylate)) doped with  $\sim 0.9$  wt% organic dye molecules of IR-140 and is pump optically using 8 nsec laser pulses at 810 nm to enable stimulated emission by excited dye molecules to the LRSP mode at  $\sim 880$  nm.

The gain media was modeled through rate equations for a four-level energy system, relating the small signal gain coefficient to the dye photo-physical parameters, dye concentration and pump irradiance. Distributed Bragg reflector (DBR) and distributed feedback (DFB) lasers were proposed using Bragg reflectors based on modulation of the metal stripe width, forming a stepped-in-width Bragg grating in the LRSP waveguide. Single mode surface plasmon DFB and DBR lasers were designed at 882 nm, by applying coupled-mode theory and transfer matrix method (TMM).

The IR-140 doped PMMA gain medium was experimentally characterized. The maximum available material gain was identified for various pump intensities and two possible pump polarization in the gain media using the variable stripe length (VSL) method. The maximum available material gain agreed well with the theoretical gain modeling performed previously.

The DFB lasers and passive Bragg gratings were fabricated in the microfabrication laboratories at Center for Research in Photonics in University of Ottawa. Main fabrication processes included electron beam lithography to create stepped-in-width Bragg grating patterns with sharp corners and edges, with features as small as 150 nm.

Passive Bragg gratings were successfully characterized by my colleague showing a clear dip in the transmittance spectra ( $\sim 40\%$ ) at the designed Bragg wavelength 882 nm.

DFB lasers were characterized and successfully demonstrated a highly narrowed (FWHM  $\sim 0.2$  nm) single mode lasing peak at 882 nm. The mode profile from the DFBs' output facet was captured by an infrared camera showing a tiny bright spot surrounded with dim spontaneous emission.

Parity Time symmetry Bragg gratings using stepped-in-width metal stripe in LRSPP structures were proposed in two different configurations. In the first configuration the top cladding PMMA was alternately doped and undoped with the same period as the stepped-in-width metal stripe but was a quarter-period spatially shifted. Asymmetric reflectance with high contrast ratio was theoretically demonstrated in the proposed PT symmetry Bragg gratings with a reasonable realization margin. In a different PT symmetric Bragg grating structure, doped PMMA stripes were considered instead of alternate doped and undoped PMMA which gave the same reflectance response but with a different fabrication processes.

## **Acknowledgements**

I would like to thank my dear supervisors, Prof. Niall Tait and Prof. Pierre Berini for all their support and encouragement. I am very grateful for the trust and faith they have had in me and for their guidance throughout my Ph.D. I appreciate them for giving me the opportunity of working on an exciting research topic and having access to the leading-edge microfabrication and electro-optical test facilities. I have learned so much through long-hours research-oriented discussion with them and I am very grateful for that.

I would also like to appreciate Mr. Anthony Olivieri from University of Ottawa, who kindly walked me through so many test and fabrication equipment. I was truly a beginner in experimental research and he patiently assisted me during the past 6 years. His work ethics and persistence have always inspired me.

I am also grateful to my dear colleagues in the electro-optical laboratory at University of Ottawa, specifically to Maude Amyot-Bourgeois and Choloong Hahn. I have enjoyed discussion on scientific and extracurricular topics with them and they have been very kind to me.

I would like to thank my dear parents and my siblings back home who always cared for me and made me proud of who I am and where I come from.

At last but foremost I would like to thank my love, my dear husband for all his care and support. His hard work and curious mind always encourage me to learn more and work harder.

# Table of Contents

<b>Abstract.....</b>	<b>2</b>
<b>Acknowledgements .....</b>	<b>4</b>
<b>Table of Contents .....</b>	<b>5</b>
<b>List of Tables .....</b>	<b>7</b>
<b>List of Figures.....</b>	<b>8</b>
<b>1. Introduction.....</b>	<b>11</b>
1.1 Surface plasmon-polariton excitations .....	11
1.2 Loss compensation, amplification, and lasing with SPPs.....	12
1.3 Quantum processes involved in SPP optical amplification .....	14
1.4 Long-range surface plasmon polariton (LRSPP).....	15
1.5 Literature review .....	18
1.5.1 Single metal-dielectric interface.....	18
1.5.2 Metal slab in symmetric/asymmetric dielectric.....	22
1.5.3 Metal-cladded dielectric .....	25
1.5.4 Metal stripe in symmetric dielectric .....	27
1.5.5 Dielectric-loaded SPP waveguide .....	29
1.5.6 Hybrid SPP waveguide .....	31
1.5.7 Amplification and lasing in nano-structures .....	33
1.6 Thesis scope and outline.....	35
<b>2. Long-range surface plasmon single-mode laser concepts .....</b>	<b>38</b>
2.1 Summary.....	38
2.2 Contribution.....	38
2.3 Article .....	38
<b>3. Gain characterization of IR-140 doped PMMA slab waveguides .....</b>	<b>44</b>

3.1 Summary.....	44
3.2 Contribution.....	44
3.3 Article.....	44
<b>4. Surface plasmon DFB laser: design optimization, fabrication and test.....</b>	<b>54</b>
4.1 Summary.....	54
4.2 Contribution.....	54
4.3 Article.....	55
4.4 Surface plasmon DFB laser optimization on alternative substrates .....	63
4.4.1 DFB lasers' design using Pyrex substrate .....	63
<b>5. PT symmetry Bragg gratings based on LRSPP structure .....</b>	<b>67</b>
5.1 Summary.....	67
5.2 Contribution.....	68
5.3 Articles .....	68
5.4 Unidirectional PT symmetry breaking Bragg grating, remarks on group and energy velocities .....	78
5.4.1 Summary .....	78
5.4.2 Contribution .....	78
5.4.3 Article.....	79
<b>6. Conclusions and future work.....</b>	<b>90</b>
6.1 Concluding remarks.....	90
6.2 Future work.....	92
<b>References .....</b>	<b>95</b>

## List of Tables

Table 1 Key properties of the asymmetric  $ss_b^0$  mode compared with the symmetric  $ss_b^0$  mode

..... 18

## List of Figures

Figure 1 Optical processes occurring for dipoles (filled red circles) near a single metal–dielectric interface. The magnitude of the SPP’s transverse electric field is shown along with the associated dipole energy transition. The black dotted curves indicate energy transfer. (a) Spontaneous emission of SPPs, (b) absorption of SPPs, (c) stimulated emission of SPPs, (d) creation of electron-hole pairs, (e) spontaneous emission of radiation. (Adapted from Ref. [10]) .... 14

Figure 2 Cross section of LRSPP waveguide, with  $w = 1 \mu\text{m}$ ,  $t = 20 \text{ nm}$ , supporting a single  $ss_b^0$  mode at 882 nm..... 15

Figure 3 Electric field profiles of (a) LRSPP waveguide and (b) single mode fiber modes 17

Figure 4 Electric field profile in an LRSPP structure using 450 nm thick PMMA as the top cladding..... 18

Figure 5 (a) Attenuated total reflection configuration with  $\theta_i$  as the angle of incidence. (b) Reflectance computed versus angle of incidence ( $\theta_i$ ) and as a function of gain ( $\alpha$ ). (Adapted from Ref. [22])..... 19

Figure 6 (a) Sketch of the sample under experimental, excitation and decoupling of SPPs. (b) Spectra of SPP emission at pump intensities below and above threshold. (Adapted from Ref. [31])..... 22

Figure 7 Normalized excited state decay rates for isotropic dipole into different energy decay channels on an infinite metal slab in symmetric dielectric media. (Adapted from Ref. [42]) ..... 24

Figure 8 (a) ASE-LRSPP measurement setup in a symmetric dielectric-metal-dielectric configuration. (b) Normalized spectrum of the TM polarized component of output emission for different pump intensities. (Adapted from Ref. [43])..... 25

Figure 9 (a) Optical micrograph of the plasmonic waveguides with locations of the input and output gratings indicated. (b) A typical loss-compensation measurement showing the pump (200  $\mu\text{J}/\text{cm}^2$ ) and probe (TE and TM) for a 30  $\mu\text{m}$ -long waveguide. (c) Signal enhancement as a function of length for a pump intensity of 200  $\mu\text{J}/\text{cm}^2$ . (Adapted from Ref. [58])..... 28

Figure 10 (a) Sketch of a hybrid SPP nanolaser consisting of an InGaN/GaN core-shell gain nanorod on a thin  $\text{SiO}_2$  layer on an epitaxial Ag film. (b) Lasing spectra at 78 K with increasing pump irradiance. Inset: Far-field laser spot with contrast fringes indicative of spatial coherence resulting from lasing. (Adapted from Ref. [72])..... 32

Figure 11 (a) Schematic of a spaser using a silver nanoshell on a dielectric core, surrounded by two dense monolayers of NQDs. (b) Energy levels and transitions in a spaser. External radiation excites e-h pairs (vertical solid arrow). The e-h pairs relax to excitonic levels (dotted arrow). The exciton recombines and its energy is transferred to the plasmon excitation of the metal nanoshell through resonant coupled transitions (dashed-dotted arrows). (c), (d) Field amplitudes,  $\phi$ , around the nanoshell in two different resonant plasmon modes. (Adapted from Ref. [78]) ..... 33

Figure 12 Effective indices of TE and TM slab modes in doped PMMA on Pyrex, and the LRSPP mode's effective index supported in a 20 nm-thick, 1  $\mu\text{m}$ -wide Au and Ag stripe on Pyrex, and covered with doped PMMA. Index of Pyrex substrate is plotted for comparison and specifying the cut-off regions ..... 64

Figure 13 MPG ( $\text{cm}^{-1}$ ) versus doped PMMA thickness for the LRSPPs using 20 nm-thick, 1  $\mu\text{m}$ -wide Ag or Au on a Pyrex substrate ..... 64

Figure 14 Computed LRSP mode electric field distribution for (a) 20nm-thick, 1  $\mu\text{m}$  wide Au stripe and 700 nm-thick PMMA, (b) 20nm-thick, 1  $\mu\text{m}$  wide Au stripe and 600 nm-thick PMMA, (c) 20nm-thick, 0.5  $\mu\text{m}$  wide Au stripe and 600 nm-thick PMMA, all on Pyrex substrate<sup>65</sup>

## 1. Introduction

In this chapter the surface plasmon-polariton (SPP) excitation is introduced. The motivation for research on amplification and lasing with SPP structures is addressed and a brief description of quantum mechanical processes involved in the optical amplification of SPP is provided. Long-range surface plasmon polariton (LRSP) mode supported by a narrow thin metal stripe in a dielectric medium is described and its key properties are presented. A recent review of the literature on amplification and lasing with SPP including various SPP structures and gain media is presented. The scope and organization of the thesis is provided at the end of this chapter.

### 1.1 Surface plasmon-polariton excitations

Plasma oscillations of conduction electrons on the surface of a metallic structure can couple to incident electromagnetic fields and generate coupled excitations of transverse magnetic (TM) polarization called surface plasmon polaritons (SPPs) [1]. Metals with a negative real part of permittivity at optical and near infrared frequencies (*e.g.* Au, Ag, Al, Cu) can support SPPs. SPP fields are tightly bound to the metal's surface and decay exponentially from the metal-dielectric interface. The surface-wave nature of SPPs implies that their momenta will be larger than that of photons at the same frequency. Indeed, SPPs can be confined to subwavelength dimensions, below the diffraction limit of light. Strong field enhancement, subwavelength localization, and high sensitivity to the local dielectric environment are among the SPP's remarkable features which offer interesting applications in integrated photonics [2], bio-sensing [3], imaging [4], spectroscopy [5], and nano-lithography [6]. See also Refs. [7] and [8] for reviews of SPP applications. SPPs excited on metallic nano-particles can enable investigation of light-matter interactions on the scale of single molecules [9]. Moreover, significant improvements in nano-fabrication techniques have facilitated the construction of SPP structures.

Unfortunately, the usefulness of SPPs is limited by the fact that these excitations have a very short lifetime due to the intrinsic loss in metals. Inter-band transition absorption at short wavelengths and free electron collisions and scattering are the main sources of attenuation in metals. Although the SPP loss could be reduced by carefully selecting the operating wavelength and by improvements in fabrication techniques, they can never be fully eliminated. Increasing the SPP mode confinement increases its spatial overlap with the metal so its attenuation also increases. Therefore, a fundamental trade off always exists between SPP mode confinement versus its attenuation.

### **1.2 Loss compensation, amplification, and lasing with SPPs**

The applications of SPP excitations are greatly limited by the high attenuation in metals at optical and near-infrared frequencies. For instance, the performance of LRSPP biosensors can be highly enhanced if the mode's attenuation is reduced or removed. Reducing loss and simultaneously maintaining SPP confinement has been a topic of investigation for a long time. Compensation of the SPP loss is generally accomplished by adding optical gain to the dielectric adjacent to the metal. Optical gain has been shown to reduce or even eliminate the attenuation, producing lossless SPP propagation. Optical gain may also exceed total attenuation and produce amplification of SPPs [10]. The gain requirement varies significantly depending on the SPP structure and mode of interest. Various gain media can be used including good dyes, quantum dots and semiconductors. Dielectrics, particularly polymers, can be doped by optical dipoles such as dyes and integrated with metals. Optical pumping is usually applied to excite such materials. Epitaxial semiconductors can be pumped electrically, but their integration with metallic structures, especially buried ones, can be difficult and their gain may be polarization dependent.

SPP amplifiers can be built as stand-alone component or as a gain section integrated with other SPP devices to improve their performance. SPP lasers can also be constructed similar to conventional lasers, such that SPPs are directly excited at the interface of a metal with the gain medium within a cavity which allows SPPs to resonate. Nano-scale SPP lasers, referred as Spaser, are also feasible by coupling the surface plasmon resonance (SPR) of metallic nanoparticles to an optical gain medium and produce a high-intensity, ultrafast source of light. A new application of amplified SPPs has emerged in optical parity-time (PT) symmetric materials where the intrinsic loss of SPPs is balanced with optical gain to produce a PT symmetric media satisfying  $\varepsilon(z) = \varepsilon^*(-z)$  [11], where  $\varepsilon(z)$  is the relative permittivity of the medium as a function of spatial coordinate  $z$ . These materials exhibit extraordinary optical phenomena such as unidirectional reflectance [12].

The focus of this thesis is on excitation and propagation of SPPs in a metal stripe which is embedded in non-uniform dielectric media. This mode offers a reasonable two-dimensional confinement with relatively lower attenuation and is termed a long-range surface plasmon polariton (LRSP). LRSP amplification using IR-140 dye molecules in a solution was studied before in the Berini's group [13] and a mode power gain coefficient  $\sim 8.55$  dB/mm was demonstrated in a structure consisting a narrow, thin Au stripe on SiO<sub>2</sub>. In this thesis we extend the LRSP amplification to lasing with LRSP using an optical gain based on the same IR-140 dye molecules, but embedded in a polymer host. Through distributed feedback and distributed Bragg reflector configurations we demonstrate tunable and coherent source of SPP with good modal confinement. Moreover, we manipulate the LRSP structure by balancing the gain with the loss and exhibit a PT symmetric Bragg grating which shows unusual unidirectional reflectance.

Before going through the details of the LRSPP structure, we briefly look into the quantum processes that are involved with SPP amplification using optical dipolar gain media such as dye molecules.

### 1.3 Quantum processes involved in SPP optical amplification

Similar to light, SPPs can be quantized in energy (considering dispersion [14,15] and absorption [16]) to provide a quantitative description of microscopic interactions between SPPs and matter. The quantum nature of SPPs has been investigated and proven experimentally, for example by the excitation of a single quantum SPP along a metallic nanowire. SPPs can be created or annihilated in a medium consisting of, *e.g.*, optically-active atoms and molecules through processes such as absorption, spontaneous emission and stimulated emission. Some quantum processes that may occur for dipolar emitters near a metal-dielectric interface supporting single-interface SPPs are sketched in Figure 1.

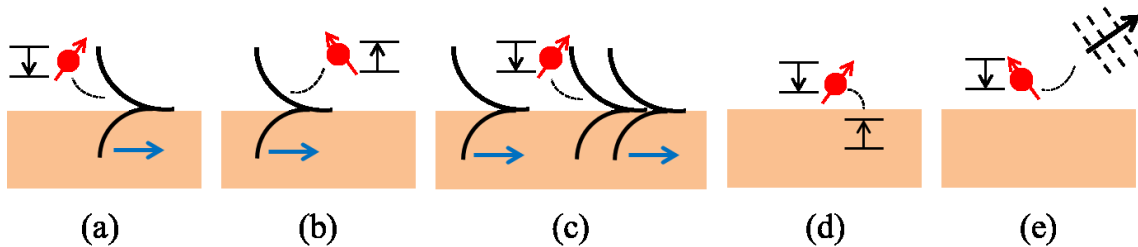


**Figure 1 Optical processes occurring for dipoles (filled red circles) near a single metal–dielectric interface.**

**The magnitude of the SPP’s transverse electric field is shown along with the associated dipole energy transition. The black dotted curves indicate energy transfer. (a) Spontaneous emission of SPPs, (b) absorption of SPPs, (c) stimulated emission of SPPs, (d) creation of electron-hole pairs, (e) spontaneous emission of radiation. (Adapted from Ref. [10])**

In close vicinity to a metallic interface, dipoles may also emit radiative modes, or interact with electron-hole pairs in the metal via dipole-dipole transitions. The photonic mode density (PMD),

which is a critical factor in the assessment of spontaneous emission rates, is modified due to the presence of a metallic interface [17].

#### 1.4 Long-range surface plasmon polariton (LRSP)

A thin metal stripe of finite width embedded in an optically infinite homogeneous dielectric can support a low loss SPP mode referred to as a long-range surface plasmon polariton (LRSP) mode [18]. This mode is also termed the  $ss_b^0$  mode since it provides a symmetric profile along both lateral dimensions; it is bound to the metal stripe and it is the lowest order SPP mode guided in this structure. A single LRSP mode can be ensured in such structures by thoughtful design of stripe dimensions (width and thickness) at a given wavelength. Figure 2 illustrates a LRSP structure similar to the one used mainly in this thesis. A 20 nm-thick, 1  $\mu\text{m}$ -wide Au stripe is laid on a 15  $\mu\text{m}$ -thick  $\text{SiO}_2$  film on a Si substrate, and covered with an optically thick polymer to guide a  $ss_b^0$  mode at around 882 nm. The top cladding polymer has to be index-matched to bottom cladding  $\text{SiO}_2$  at the wavelength of interest (882 nm) to enable propagation of the  $ss_b^0$  mode in this structure.

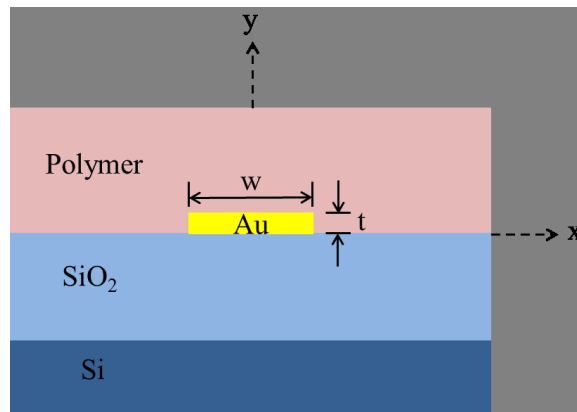


**Figure 2 Cross section of LRSP waveguide, with  $w = 1 \mu\text{m}$ ,  $t = 20 \text{ nm}$ , supporting a single  $ss_b^0$  mode at 882 nm**

The  $ss_b^0$  mode propagates in  $+z$  direction with  $e^{-\gamma z}$ , where  $\gamma = \alpha + j\beta$  is the mode's complex propagation constant,  $\alpha$  and  $\beta$  are the attenuation phase constants respectively and  $e^{+j\omega t}$  harmonic

time dependence is implied. This waveguide is modeled using the commercial numerical solver Comsol Multiphysics v.5.2 and the propagation constant at  $\lambda_0 = 882$  nm is derived. For the modeling the refractive index of Au and the surrounding media (SiO<sub>2</sub> and polymer) at  $\lambda_0 = 882$  nm are assumed as  $n_{Au} = 0.22138 - j5.3142$ , and  $n_{polymer} = n_{SiO_2} = 1.452$  respectively [19]. The  $ss_b^0$  mode effective index ( $n_{eff}$ ) and mode power attenuation (MPA) [20] are defined in Eq. 1 and Eq. 2 and obtained as  $n_{eff} = 1.4527$  and  $MPA = 2.6$  dB/mm.

$$n_{eff} = \frac{\beta\lambda_0}{2\pi} \quad (1)$$

$$MPA = \alpha \frac{20}{1000} \log_{10} e \quad (\text{dB/mm}) \quad (2)$$

The propagation length of the mode is the distance from the  $ss_b^0$  launch point to where the mode power drops by a factor of  $1/e$  and is equal  $L = 1/2\alpha$  which is found as 192  $\mu\text{m}$  for our waveguide. Comparing the LRSPP waveguide to a single interface Au/SiO<sub>2</sub> which supports a one-dimensional SPP mode at  $\lambda_0 = 882$  nm, the propagation length of the LRSPP mode is about 120 times larger indicating a much lower attenuation. We can see now that the reduced attenuation sacrifices the mode confinement. The SPP field's penetration depth into the dielectric medium  $w$  and can be approximated by Eq. 3 [21].

$$w \approx m \left[ \beta^2 - \varepsilon_d \left( \frac{\omega}{c} \right)^2 \right]^{-1/2} \quad (3)$$

where  $m = 1$  for the single interface SPP and  $m = 2$  for the LRSPP waveguide,  $\varepsilon_d = n_d^2$  is the relative permittivity of the dielectric,  $\omega = 2\pi/\lambda_0$  is the angular frequency, and  $c = 3 \times 10^8$  m/s is the speed of light in vacuum. Thus, the field penetration depth into the cladding is roughly a factor of 2 larger for the LRSPP compared to the single-interface SPP for the same materials and operating wavelength, meaning that the single-interface structure confines SPPs more strongly than an LRSPP structure.

The mode profile for the main transverse electric field component ( $E_y$ ) of  $ssb^0$  mode in LRSPP structure is plotted in Figure 3(a) and it is compared to the mode profile of a standard single mode fiber for 882 nm (*e.g.* Thorlabs 780HP). The coupling efficiency of the  $ssb^0$  mode to the single mode fiber can be estimated using Eq. 4 [20].

$$C = \frac{\iint_{A_s} E_{y_1} \cdot E_{y_2}^* dA}{\sqrt{\left(\iint_{A_s} E_{y_1} \cdot E_{y_1}^* dA\right)\left(\iint_{A_s} E_{y_2} \cdot E_{y_2}^* dA\right)}} \quad (4)$$

where  $E_{y_1}$  corresponds to main transverse electric field component of the  $ssb^0$  mode and  $E_{y_2}$  corresponds to electric field of a single mode fiber which can be defined as a Gaussian distribution aligned to the center of LRSPP waveguide (as shown in Figure 3(b)).

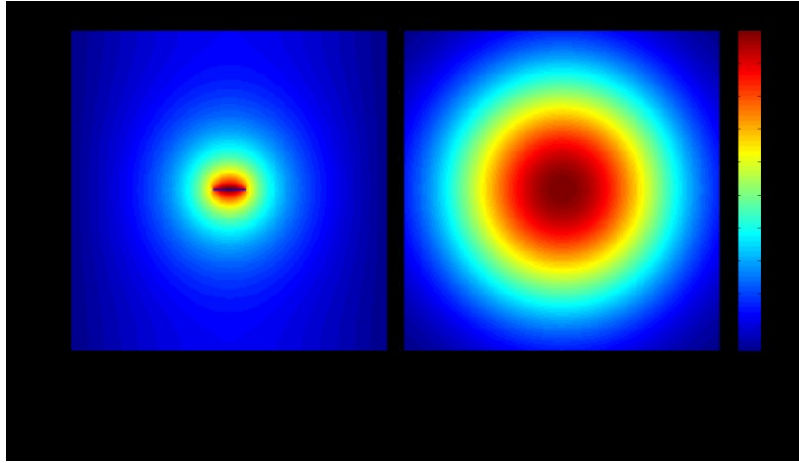


**Figure 3 Electric field profiles of (a) LRSPP waveguide and (b) single mode fiber modes**

Coupling efficiency calculation results in 94% coupling efficiency between the  $ssb^0$  mode and the single mode fiber. It should be noted here that the polymer used in this thesis was PMMA and it was doped with about 0.9wt% IR-140 dye molecules. The refractive index of dye-doped PMMA at  $\lambda_0 = 882$  nm is  $n_{PMMA} \sim 1.5$  which does not match the refractive index of  $\text{SiO}_2$  at that wavelength. No LRSPP mode can be supported using optically thick dye-doped PMMA on a  $\text{SiO}_2$  substrate due to index mismatch. The solution to this problem is to lower the thickness of

the dye-doped PMMA sufficiently so that with the air on top an effective index match with that of SiO<sub>2</sub> can be achieved. The  $ss_b^0$  mode profile in this structure does not look fully symmetric; however it has all other properties of a symmetric  $ss_b^0$  mode. The  $E_y$  profile of an asymmetric  $ss_b^0$  mode using a 450 nm-thick dye-doped PMMA is shown in Figure 4 and its key properties are summarized in Table 1.

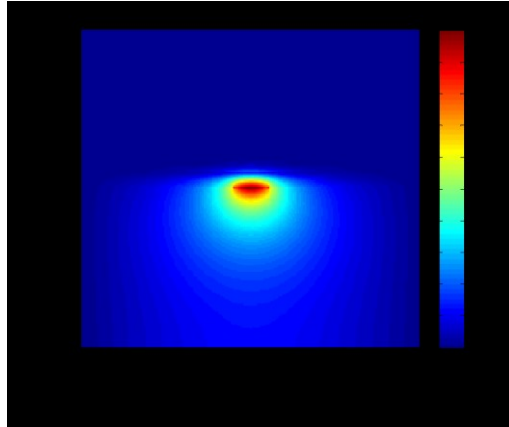


**Figure 4** Electric field profile in an LRSPP structure using 450 nm thick PMMA as the top cladding

**Table 1** Key properties of the asymmetric  $ss_b^0$  mode compared with the symmetric  $ss_b^0$  mode

	MPA (dB/mm)	L (μm)	Mode size (μm)	C
asymmetric LRSPP	4.6	110	4.1	71%
symmetric LRSPP	2.6	192	6.2	94%

## 1.5 Literature review

Numerous theoretical and experimental works have been reported on amplification and lasing with SPPs. Various SPP structures and optical gain materials have been investigated. I will classify the literature by the SPP structure and whether the SPP is confined in one, two or three dimensions.

### 1.5.1 Single metal-dielectric interface

SPP amplification in a single-interface structure comprising a thin Ag film sandwiched between a prism and a gain medium was investigated in theory by Plotz *et. al.*[22] Using Fresnel reflection formulas, they computed the reflectance of light incident onto the prism versus angle of incidence and as a function of the gain of the medium. In the passive case, near the angle for surface-plasmon excitation, the usual attenuated total reflection (ATR) associated with the SPP mode was observed. However, by increasing the gain, the ATR monotonically reduced such that above a certain gain threshold, enhanced reflectivity resulted. They also showed that above the gain threshold one could adjust the metal film's thickness to produce a singularity in the reflectance. Figure 5 shows the ATR configuration used in this modeling along with the reflectance computed as function of gain.

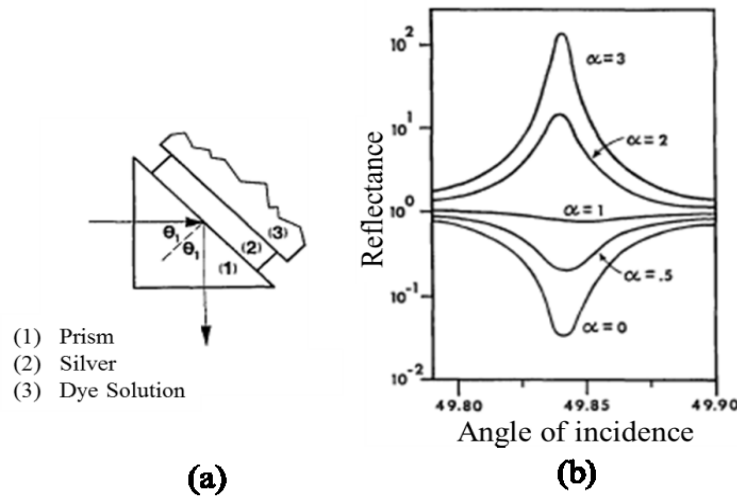


**Figure 5 (a) Attenuated total reflection configuration with  $\theta_i$  as the angle of incidence. (b) Reflectance computed versus angle of incidence ( $\theta_i$ ) and as a function of gain ( $\alpha$ ). (Adapted from Ref. [22])**

The same structure was also studied by Sudarkin and Demkovich [23] considering higher gain in the amplifying medium. They showed that at high gain the Fresnel formulas are not valid to calculate the reflectance of the incident beam, which is of limited width. They also predicted

super-luminescence of surface waves in the high gain regime and were the first to suggest a SPP laser based on this phenomenon.

The propagation properties of SPPs along a planar single interface structure were theoretically investigated by Nezhad *et al.* [24] They analyzed the case of an infinite interface between a metal and a gain medium, rigorously working with propagation constants and Poynting vectors, and found the required gain coefficient for lossless SPP propagation. A material gain of  $\sim 1260 \text{ cm}^{-1}$  was estimated for a lossless SPP propagation for an Ag-InGaAsP interface at  $\lambda_0 = 1550 \text{ nm}$ .

Kumar *et al.* [25] considered a metal-semiconductor diode structure comprising a p-n junction of GaAs adjacent to an Au substrate. The electron-hole recombination energy coupled to SPPs on the Au-GaAs interface. They showed how the carrier injection level in GaAs controlled the spontaneous emission rate and provided gain for SPP amplification. Lu *et al.* [26] considered optical parametric amplification of SPPs in a nonlinear hybrid waveguide consisting of Ag-LiNbO<sub>3</sub>. The seed and pump wavelengths required for efficient power conversion were found. They estimated  $\sim 30 \text{ dB}$  gain over 3 mm of coupling length for a pump intensity of  $\sim 50 \text{ MW/cm}^2$ . Sirtori *et al.* [27] used a single interface SPP waveguide on a quantum cascade semiconductor laser at far-infrared wavelengths ( $\lambda \sim 11 \text{ }\mu\text{m}$ ). Their goal was to increase the mode's confinement and overlap with the gain medium, while simultaneously reducing the total layer thickness in the structure. Shortly later, Tredicucci *et al.* [28] similarly proposed a single-mode SPP laser at  $\lambda_0 \sim 17 \text{ }\mu\text{m}$ , in a distributed feedback (DFB) configuration using two-metal (Ti/Au) grating adjacent to a quantum cascade active semiconductor.

Seidel *et al.* [29] experimentally demonstrated SPP stimulated emission at optical wavelengths. They used 39 and 67 nm thick Ag films in contact with liquid dye gain media

(Cresyl violet or Rhodamine 101 in ethanol) in the Kretschmann-Raether configuration. A p-polarized probe at  $\lambda_0 = 633$  nm was focused on the Ag-dye interface with a specific incidence angle near the SPP excitation angle while the dye medium was pumped at  $\lambda_0 = 580$  nm. The ATR was measured as a function of the probe incidence angle, with and without pumping the gain medium. The difference between the pumped and un-pumped cases was attributed to stimulated emission of SPPs on the Ag-dye interface. The reflectance increased over the SPP excitation angle for the 39 nm thick Ag films whereas it narrowed and deepened for the 67 nm thick Ag films, both cases in agreement with theory [23]. A similar study was conducted by Noginov *et al.* [30] but with the gain medium formed as a 10  $\mu\text{m}$ -thick film doped with Rhodamine-6G. The gain medium was pumped at  $\lambda_0 = 532$  nm by a Nd:YAG laser and a He-Ne laser beam at  $\lambda_0 = 594$  nm was illuminating the Ag-gain interface through the prism. Increased reflectance at the SPP excitation angle was observed due to the stimulated emission of SPPs on the interface. They obtained an optical gain of  $420\text{ cm}^{-1}$  with a dye concentration of  $N = 1.2 \times 10^{22}\text{ cm}^{-3}$  and a pump intensity of  $I = 1.7 \times 10^7\text{ W/cm}^2$ , which compensated  $\sim 35\%$  of the SPP loss. In another experiment [31] they excited SPPs through pumping a thinner ( $\sim 3\text{ }\mu\text{m}$ ) dye-doped polymer film at the dye's peak absorption wavelength, and decoupled spontaneously emitted SPPs to the prism in ATR configuration. They demonstrated narrowing of the SPP spectra by increasing the pump intensity, which was attributed to stimulated emission of SPPs. Figure 6(a) sketches the SPP excitation and decoupling in the ATR configuration used in the experiment. The SPP emission spectrum narrowing with increasing pump intensity from  $10.9\text{ mJ/cm}^2$  to  $81.9\text{ mJ/cm}^2$  is shown in Figure 6(b).

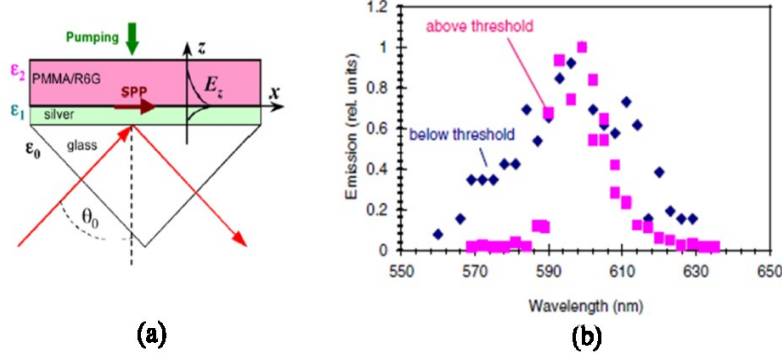


**Figure 6 (a) Sketch of the sample under experimental, excitation and decoupling of SPPs. (b) Spectra of SPP emission at pump intensities below and above threshold. (Adapted from Ref. [31])**

Amplified spontaneous emission of SPPs (ASE-SPP) at the interface of a 1  $\mu\text{m}$ -thick PMMA layer doped with PbS quantum dots (QDs) and a 100 nm thick Au film on a Silica substrate was observed by Bolger *et al.* [32] SPPs were excited at the QDs emission peak and out-coupled through a grating on the interface. The full-width half-maximum (FWHM) SPP emission was observed to decrease with increasing pump intensity as expected for ASE-SPP. The pump intensity threshold for ASE-SPP was measured as 5  $\text{W}/\text{cm}^2$ . It was found that ASE-SPP at high pump intensities limits the available gain such that only a 30% increase in SPP propagation length was obtained. The gain depletion due to ASE was suggested as the reason.

### 1.5.2 Metal slab in symmetric/asymmetric dielectric

The properties of strong optical amplification of SPPs for flat or corrugated ( $\sim 10$  nm period) Ag slabs in contact with a gain medium were investigated theoretically by Avrutsky [33]. SPP resonance was obtained at  $\lambda = 350$  nm, when the optical gain increased to  $\sim 80,000$   $\text{cm}^{-1}$ . The SPP resonance was accompanied by a huge group index ( $\sim 5.4 \times 10^4$ ), extremely low group velocity ( $\sim 1$  km/s), highly localized SPPs, and an abrupt change of positive SPP loss to negative SPP loss (meaning loss overcompensation). The large material gain required in this scheme sounds challenging, but it is interesting that such extreme confinement may be possible.

Although strongly enhanced ASE-SPP may compromise the available gain and noise performance. Nezhad *et al.* [24] considered a 40 nm Ag slab embedded in InGaAsP gain media and found that  $\sim 360 \text{ cm}^{-1}$  of gain is required for lossless LRSPP propagation at  $\lambda_0 = 1550 \text{ nm}$ . Lasing in plasmonic bandgap structures was investigated [34,35,36] using a 2D corrugated metal film sandwiched between two symmetric dielectrics doped with dye molecules. It was shown experimentally that the dye molecules' fluorescence was highly enhanced in the vicinity of the corrugated film. SPP lasing was proposed in these structure provided that the dye peak emission wavelength falls at the edge of the plasmonic bandgap, supporting a standing LRSPP mode due to highly enhanced SPP fields and lower absorption of this mode. The same concept was also considered by Winter *et al.* [37] who argued that fluorescent dye can also decay into asymmetric SRSPP guided modes reducing the available gain for stimulated emission of LRSPP.

Genov *et al.* [38] developed a new method based on a quasi-metal approximation for the explicit solution of the dispersion relation of an insulator-metal-insulator (IMI) structure, where the metal slab is bounded by multiple quantum well (MQW) gain media. Using their method, they could obtain the critical gain required for lossless SPP propagation in a thin Ag film cladded by InGaAsP, InGaN MQW gain media.

De Leon and Berini [39,40] developed a theoretical model for treating SPP amplification in planar structures where gain is provided by a laser dye solution. They assumed a four-level dipolar gain system, and accounted for the position dependency of dye molecules' lifetime as well as an inhomogeneous pump intensity distribution. Through their modeling, they predicted lossless LRSPP propagation on a Ag film bounded in symmetric dielectric media involving R6G in solvent using a modest pump intensity of  $\sim 200 \text{ KW/cm}^2$  and a reasonable dye concentration of  $N = 1.8 \times 10^{18} \text{ cm}^{-3}$ . They also considered a single interface system using the same gain media

but found that a higher dye concentration ( $N = 2.4 \times 10^{19} \text{ cm}^{-3}$ ) and a much stronger pump intensity ( $\sim 3.5 \text{ MW/cm}^2$ ) were needed for lossless SPP propagation. They later investigated the noise figure for amplified single interface SPPs and LRSPPs [41] and found that the noise figure of LRSPPs is less than that of the single interface SPPs, and that it diverges as the energy asymptote is approached in both cases due to increased spontaneous emission rate. They also showed [42] that the spontaneous decay rate into LRSPPs is lower than for decay into SRSPs in close proximity to a metal slab in a symmetric one-dimensional structure. Figure 7 shows the computed decay rates into the guided modes of an infinite metal slab in symmetric dielectric.

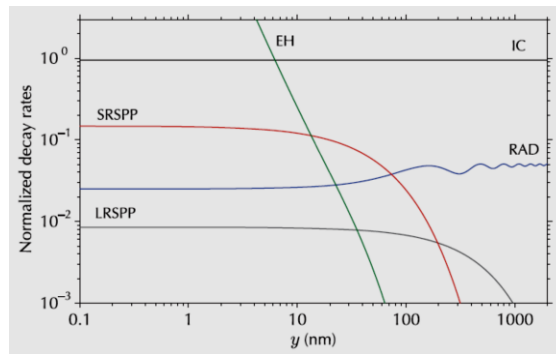


**Figure 7 Normalized excited state decay rates for isotropic dipole into different energy decay channels on an infinite metal slab in symmetric dielectric media. (Adapted from Ref. [42])**

Gather *et al.* [43] reported LRSPP gain at visible wavelengths in a symmetric structure consisting of a  $1 \mu\text{m}$  thick fluorescent polymeric gain layer and a  $4 \text{ nm}$  thick Au film. Figure 8(a) illustrates the LRSPP structure under test which was optically pumped from the top using  $5 \text{ ns}$  laser pulses at  $\lambda_0 = 532 \text{ nm}$ . They performed ASE-LRSPP measurements by increasing the pump stripe length and demonstrated the emission threshold and spectrum narrowing as plotted in Figure 8(b). They obtained an LRSPP net gain coefficient of  $\sim 8 \text{ cm}^{-1}$  at  $\lambda_0 \sim 600 \text{ nm}$ .

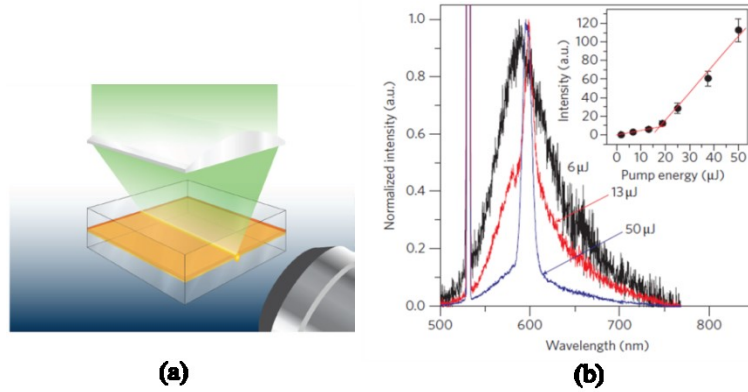


**Figure 8 (a) ASE-LRSPP measurement setup in a symmetric dielectric-metal-dielectric configuration. (b) Normalized spectrum of the TM polarized component of output emission for different pump intensities. (Adapted from Ref. [43])**

Hahn *et al.* [44] considered the interaction of the LRSPP mode with optical gain in a symmetric PMMA-Ag-PMMA structure where both claddings (top and bottom PMMA) were doped with IR-140 dye. They theoretically showed that the gain medium in the bottom cladding doubles the LRSPP gain at high pump intensities  $\sim 4 \text{ MW/cm}^2$ , even though the pump is applied from the top and is partially reflected by the Ag film. They also measured the LRSPP gain by the variable stripe length (VSL) method and found a gain coefficient of  $16.7 \text{ cm}^{-1}$  with a pump intensity of  $4 \text{ MW/cm}^2$ .

I. P. Radko *et al.* [45] implemented an asymmetric dielectric-metal-dielectric waveguide consisting of a 50 nm-thick Au film deposited on a quartz substrate and covered with a thin layer of PMMA doped with lead-sulphide (PbS) QDs. The sample was optically pumped from the top at  $\lambda_0 = 532 \text{ nm}$ , whereas a CW probe at  $\lambda_0 = 860 \text{ nm}$  was used to excite the SPP mode in the waveguide through a grating coupler. By collecting the leakage radiation from the quartz side of the sample at the Kretschmann angle they could estimate a SPP gain of  $\sim 200 \text{ cm}^{-1}$ .

### 1.5.3 Metal-cladded dielectric

Maier [46] computed the gain required for lossless SRSPP propagation in a symmetric metal-insulator-metal (MIM) heterostructure where the core material exhibits optical gain. Gain coefficients of  $1625 \text{ cm}^{-1}$  and  $4830 \text{ cm}^{-1}$  were required for lossless propagation at  $\lambda_0 = 1550 \text{ nm}$  in 500 nm-thick and 50 nm-thick semiconductor cores, respectively.

Chang and Chuang [47,48] formulated quasi-orthogonality and normalization conditions suitable for computing field-enhanced spontaneous and stimulated emission rates in micro- and nano-sized metal-cladded dielectrics. They also modified the definition of the confinement factor in SPP nano-lasers, where the group velocity is very low and the SPP fields are highly confined.

SPP amplification and lasing were investigated by Li and Ning [49] in metal-semiconductor-metal (MSM) structures. They demonstrated a SPP mode power gain 1000 times greater than the semiconductor's material gain near the energy asymptote where the group velocity is very low. They also investigated the amplification and lasing threshold conditions in these structures assuming electrical injection [50]. Khurgin and Sun [51] investigated similar MSM structures near the SPP energy asymptote. They found that a significantly high current density injection of  $\sim 100 \text{ kA/cm}^2$  is required for loss compensation due to the Purcell effect inherent to sub-wavelength confinement in these structures.

Chen *et al.* [52] used a finite difference time domain (FDTD) method to model amplified SPP propagation in MSM structures. They specifically considered an Au-InGaAs-Au structure and predicted lossless SRSPP propagation in a 75 nm-thick structure with a material gain of  $2500 \text{ cm}^{-1}$  at  $\lambda_0 = 1550 \text{ nm}$ .

Yu *et al.* [53] investigated the reflection and transmission of a short-length, metal-cladded dielectric waveguide coupled to a small cavity filled with an InGaAsP gain medium, showing that the cavity losses can be fully compensated for a material gain of  $\sim 2000 \text{ cm}^{-1}$  at  $\lambda_0 \sim 1550$

nm. The gain assisted MDM plasmonic waveguide can work as an ON/OFF switch in the presence/absence of pumping.

Hill *et al.*[54] demonstrated electrically-pumped lasing from rectangular etched InGaAs pillars coated by 20 nm silicon nitride then by a thick Ag layer. Vertical confinement was provided by steps in refractive index in the gain region, whereas sub-wavelength confinement along the horizontal direction occurs due to the Au coating. Mirrors at the end facets define a Fabry-Perot cavity. Lasing was obtained at cryogenic temperatures (10 K) observed via leakage radiation microscopy through the substrate.

#### **1.5.4 Metal stripe in symmetric dielectric**

Alam *et al.* [55] considered a 1  $\mu\text{m}$ -wide, 10 nm-thick Ag stripe on AlGaInAs multiple quantum wells (MQWs) covered by barrier material for the purpose of LRSPP amplification. The required material gain for lossless LRSPP propagation at  $\lambda_0 = 1550$  nm was found to be  $\sim 400$   $\text{cm}^{-1}$ . LRSPP whispering gallery modes in GaAs-based, micro-disk cavities incorporating a thin metal film were investigated at  $\lambda_0 = 1400$  nm by Chen and Guo [56]. They computed the resonator's Q and lasing gain threshold as  $\sim 4000$  and  $\sim 200$   $\text{cm}^{-1}$  respectively.

Experimental demonstration of the stimulated emission of LRSPPs on a 8  $\mu\text{m}$ -wide, 20 nm-thick Au stripe cladded by Er-doped glass was performed by Ambati *et al.* [57] at  $\lambda_0 = 1532$  nm. Probe and pump signals were both coupled to the waveguide LRSPP mode. By applying a maximum pump power of 266 mW, the probe signal was enhanced to  $\sim 50\%$ .

De Leon and Berini [13] reported LRSPP amplification in a waveguide comprising a 1  $\mu\text{m}$ -wide, 20 nm-thick Au stripe on a 15  $\mu\text{m}$ -thick  $\text{SiO}_2$  on Si, and covered by IR-140 dye in solvent index-matched to  $\text{SiO}_2$ . The structure was probed at  $\lambda_0 = 882$  nm using butt-coupled polarization maintaining, single-mode fibers and pumped optically from the top at  $\lambda_0 = 808$  nm

using  $20 \text{ mJ/cm}^2$ , 8 ns laser pulses. A small-signal mode power gain coefficient of  $\gamma = 8.55 \text{ dB/mm}$  was obtained in this experiment.

A direct observation of plasmonic gain was reported by Kéna-Cohen *et al.* [58] in an asymmetric structure consisting of a  $1 \text{ }\mu\text{m}$ -wide,  $21 \text{ nm}$ -thick Au stripe of different lengths on a glass substrate and covered by a thin polymeric gain medium (Alq3:DCM). The thickness of the optically pumped gain medium was selected to support a confined LRSPP mode. Grating couplers were used to probe the waveguide using broadside incident beams and the pump was applied to the top. Figure 9(a) sketches the waveguides in top view with input and output grating couplers indicated. A typical loss-compensation measurement showing the pump ( $200 \text{ }\mu\text{J/cm}^2$ ) and probe (TE and TM) for a  $30 \text{ }\mu\text{m}$ -long waveguide is sketched in Figure 9(b).

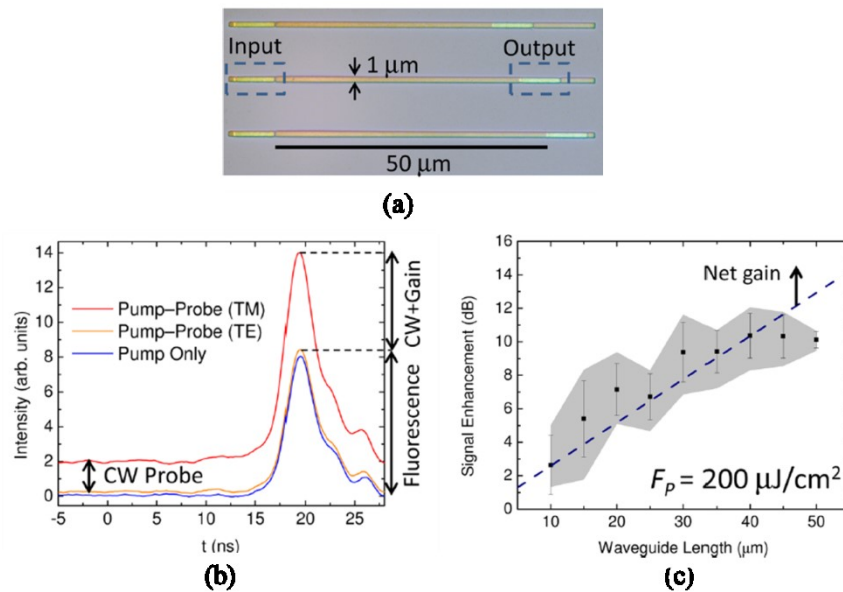


**Figure 9 (a) Optical micrograph of the plasmonic waveguides with locations of the input and output gratings indicated. (b) A typical loss-compensation measurement showing the pump ( $200 \text{ }\mu\text{J/cm}^2$ ) and probe (TE and TM) for a  $30 \text{ }\mu\text{m}$ -long waveguide. (c) Signal enhancement as a function of length for a pump intensity of  $200 \text{ }\mu\text{J/cm}^2$ . (Adapted from Ref. [58])**

Direct fluorescence is observed for both pump–probe (TE) and pump only configurations. However, for the pump–probe (TM) arrangement, the DC contribution due to the CW probe is seen and the additional signal in the presence of the pump corresponds to both the CW contribution and gain, giving a signal enhancement factor of  $F = 3.2 \pm 0.1$ . Using systematic measurements of the signal enhancement as a function of waveguide length, they measured a net gain of  $(3.4 \pm 16)$  dB/mm at  $\lambda_0 = 633$  nm using  $200 \mu\text{J}/\text{cm}^2$  pump intensity as shown in Figure 9(c).

Flynn *et al.* [59] demonstrated LRSPP lasing at  $\lambda_0 \sim 1.46 \mu\text{m}$  in a symmetric structure based on InP and consisting of a 15 nm-thick Au film placed between MQW heterostructure layers with a minimum lateral width of  $100 \mu\text{m}$ . A 1 mm long Fabry-Perot structure formed a LRSPP laser cavity which emitted a TM-polarized light under optical pumping from the top at  $\lambda_0 = 1.06 \mu\text{m}$  with 140 ns pulses. The emitted spectrum narrowed with increasing pump intensity, and the emitted power was linearly dependent on the pump intensity beyond a clear threshold.

### 1.5.5 Dielectric-loaded SPP waveguide

Dielectric-loaded SPP waveguides (DLSPPW) using 600 nm thick, 400 nm-wide PMMA stripes, doped with PbS quantum dots (QDs), and deposited on a 40 nm-thick Au film were investigated by Grandidier *et al* [60] Optical gain was provided by pumping QDs in the waveguide from the top at  $\lambda_0 = 532$  nm. Stimulated emission of the SPP guided mode was qualitatively confirmed by linewidth narrowing of the SPP mode. The SPP propagation length was measured versus pump irradiance exhibiting a linear increase of propagation length above the pump threshold  $\sim 500 \text{ W}/\text{cm}^2$ . A maximum increase in propagation length of  $\sim 27\%$  was obtained. The gain coefficient of the amplified waveguide versus the pump irradiance was also measured near the QD peak emission ( $\lambda_0 \sim 1550$  nm). They subsequently studied PMMA stripes doped with CdSe/ZnSe QDs

deposited on a 50 nm-thick Ag film. Their work was based on leakage radiation microscopy combined with surface plasmon coupled emission. They reported a similar increase in SPP propagation length at  $\lambda_0 = 632.8$  nm [61].

C. Garcia *et al.* [62] considered a DLSPW at  $\lambda_0 \sim 860$  nm comprising a 300 nm-thick, 300 nm-wide PMMA ridge doped with PbS QDs deposited on a 70 nm-thick Au film on a glass substrate. They similarly used leakage radiation microscopy to study stimulated emission of SPPs in the waveguide. About a 33% increase in the propagation length of SPPs was reported for a probe power of 16 mW and pump intensity of  $\sim 4460$  W/cm<sup>2</sup> which produced an optical gain of  $\sim 143$  cm<sup>-1</sup>.

Colas des Francs *et al.* [63] modeled in general the local density of guided modes for two-dimensional SPP waveguides incorporating a gain medium. They assumed a 4-level dipolar gain medium to describe spontaneous and stimulated emission rates into SPPs. They specifically applied their model to a DLSPW reported earlier [60] and deduced the stimulated emission cross-section of PbS QDs.

Rao and Tang [64] derived conditions for lossless SPP propagation in a single metal dielectric structure assuming stimulated emission in the active dielectric. They considered a wide range of wavelengths in the visible and infrared regions, and various metals. In particular they studied lossless propagation at extremely short wavelengths near the energy asymptote. Using their model, they designed a nanoscale DLSPW with a dielectric cross section of  $22 \times 20$  nm<sup>2</sup> and computed a required optical gain of  $\sim 5 \times 10^4$  cm<sup>-1</sup> in the dielectric to produce lossless sub-wavelength propagation at  $\lambda_0 = 450$  nm.

Hahn *et al.* [65] proposed a dielectric-loaded LRSPP waveguide in a symmetric PMMA-Ag-PMMA structure, where a top PMMA ridge is used to laterally confine a LRSPP mode. Both

the top and bottom PMMA layers were assumed to be doped with IR-140 dye molecules and the waveguide is pumped optically from the top. They introduced single-mode DFB lasers by stepping the width of the top PMMA while optical gain is provided in both PMMA regions.

### 1.5.6 Hybrid SPP waveguide

Hybrid SPPs are a coupled TM-polarized wave, guided in a nanoscale low-index dielectric gap between a high-index dielectric and a metal surface. It is a super-mode excited by coupling the SPP mode on a metal-gap interface to the photonic mode of high-index dielectric [66,67,68]. Loss compensation or lasing with hybrid SSPs is possible if the high-index region provides optical gain over which the hybrid SPP overlaps sufficiently.

Oulton *et al.* [69] reported an experimental demonstration of a nanoscale laser in hybrid plasmonic structures consisting of a high-gain CdS nanowire separated from a Ag substrate by a 5 nm-thick MgF<sub>2</sub> gap. Multi-mode lasing at  $\lambda_0 \sim 489$  nm was observed from the end facets of the nanowire under a  $\sim 76.25$  MW/cm<sup>2</sup> pump irradiance. Other designs for lasing using CdS nano-squares [70] and an embedded waveguide (WEM) [71] were also reported in hybrid structures.

A hybrid SPP laser consisting of an InGaN/GaN core-shell nanorod separated from an Ag film by a thin SiO<sub>2</sub> layer was demonstrated by Lu *et al* [72]. The nanorod as well as the Ag film were epitaxially grown to provide the atomic-scale smoothness necessary for reducing diffraction loss and providing low threshold CW lasing. Figure 10(a) sketches the hybrid SPP structure showing the field concentration in the low-index region but also significant overlap with the nanorod in order to provide gain. Figure 10(b) shows lasing emission spectra with increasing pump irradiance at 78 K. Bimodal lasing at 510 and 522 nm was obtained with a CW pump intensity of  $\sim 26$  KW/cm<sup>2</sup> at 78 K as seen in Figure 10(b).

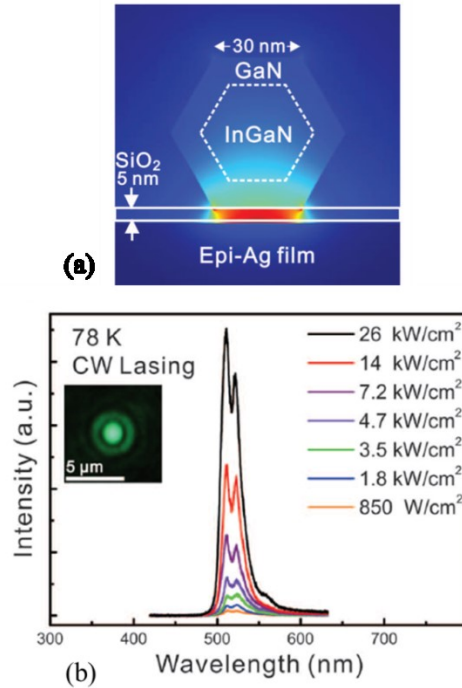


**Figure 10 (a)** Sketch of a hybrid SPP nanolaser consisting of an InGaN/GaN core-shell gain nanorod on a thin SiO<sub>2</sub> layer on an epitaxial Ag film. **(b)** Lasing spectra at 78 K with increasing pump irradiance. Inset: Far-field laser spot with contrast fringes indicative of spatial coherence resulting from lasing. (Adapted from Ref. [72])

Sidiropoulos *et al.* [73] reported ultra-fast (shorter than 800 fs) hybrid SPP lasing using ZnO nanowires separated from a Ag substrate by a thin LiF gap. ZnO excitons at room temperature lie near the SPP frequency in the hybrid SPP laser, and strong mode confinement leads to accelerated spontaneous emission recombination. The dynamics of the ZnO nanowire SPP laser were compared to those of conventional ZnO nanowire photonic lasers revealing a sub-picosecond pulse width for the SPP nanolaser but a much broader pulse width for the corresponding photonic nanolaser.

A low loss hybrid SPP laser design using MQWs in a P-N heterojunction and electric pumping was reported by Li and Huang [74]. Their design optimized the hybrid SPP mode's overlap with the P-N active region.

### 1.5.7 Amplification and lasing in nano-structures

Conduction electrons in metal nanoparticles irradiated by linearly polarized light form dipolar oscillations is referred to as a surface plasmon resonance (SPR) [75,76]. Resonant surface plasmons are supported by metal nanoparticles smaller than the skin depth ( $\sim 25$  nm) so that optical fields can penetrate throughout their volume and drive electron oscillations. SPRs of high quality in proximity to a gain medium can lead to surface plasmon amplification by stimulated emission of radiation (spaser) [77,78]. Figure 11 sketches the spasing mechanism as explained by Stockman [78] in a spaser composed of a silver nanoshell covering a dielectric core of 10–20 nm radius, and surrounded by two dense monolayers of nanocrystal quantum dots (NQDs).

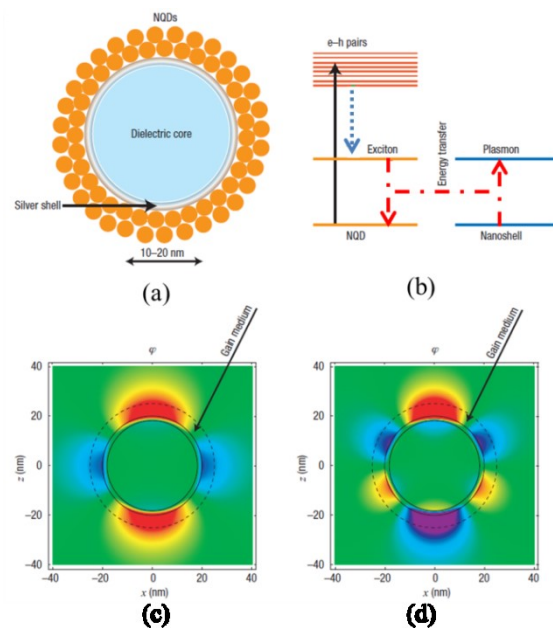


Figure 11 (a) Schematic of a spaser using a silver nanoshell on a dielectric core, surrounded by two dense monolayers of NQDs. (b) Energy levels and transitions in a spaser. External radiation excites e–h pairs (vertical solid arrow). The e–h pairs relax to excitonic levels (dotted arrow). The exciton recombines and its energy is transferred to the plasmon excitation of the metal nanoshell through resonant coupled transitions (dashed-dotted arrows). (c), (d) Field amplitudes,  $\phi$ , around the nanoshell in two different resonant plasmon modes. (Adapted from Ref. [78])

Pumping the gain medium (optical or electric) excites electron-hole (e-h) pairs (solid arrow). The e-h pairs relax to excitonic levels (dotted arrow). The excitons recombine and their energy is transferred to the plasmon excitation of the metal nanoshell through resonant coupled transitions (dashed-dotted arrows).

Noginov *et al.* [79] demonstrated a spaser using spherical nanoparticles consisting of a 14 nm Au core, coated with a 15 nm SiO<sub>2</sub> shell and doped with Oregon Green 488 dye. The quality factor of nanoparticles was found as  $\sim 13.2$ . Stimulated emission of SPPs at  $\lambda \sim 531$  nm by individual nanoparticles was reported. Meng *et al.* [80] considered a monolayer of randomly oriented Au nanorods embedded in the mesopores of a silica shell dispersed on a glass substrate and covered with a 200 nm thick R6G-doped PVA film to supply gain. The spaser emission was tunable from 562 to 627 nm with a spectral line width narrowed down to 5 -11 nm. In a theoretical study by Khurgin and Sun [81], they showed that lasing in electrically-pumped semiconductor spasers has an extremely high current threshold of  $\sim 105$  A/cm<sup>2</sup>. They attributed the high current threshold to gain depletion caused by enhanced spontaneous emission.

Dorfman *et al.* [82] proposed a low threshold and efficient spaser using quantum coherence in a three-level quantum emitter based gain medium coupled to plasmonic nanostructures. Ginzberg and Zayats [83] developed a theory to obtain the linewidth and its enhancement in semiconductor spasers. They specifically considered bulk GaAs as the active medium of a spaser and estimated a linewidth enhancement of  $\sim 3-6$  which is about an order of magnitude larger than that predicted by the Shawlow-Townes theory. Single molecule detection based on surface enhanced Raman scattering (SERS) is possible using spasers as they can produce near-singular scattering hot spots [84,85,86]. Array of nanoparticles for improved spaser quality has also been investigated. Suh *et al.* [87] reported coherent and directional emission

from optically pumped arrays of Au bowtie resonators on slabs of IR-140 doped polyurethane on a Si substrate and covered with a dielectric over-layer. Zhou *et al.* [88] reports a two-dimensional plasmonic lattice consisting of a pattern of Au nanoparticles on a glass substrate, covered by a polyurethane layer doped with IR-140. Their structure features high directionality due to lattice bandedge lasing and ultrafast response due to plasmonic-enhanced localization. Loss compensation in extraordinary optical transmission (EOT) systems was theoretically studied by Marani *et al* [89]. They specifically analyzed the spectral response of an optically pumped periodic array of subwavelength slits in an opaque Au film sandwiched between two thin layers of Rh800-doped polymer. They showed that this structure can behave as an absorber, laser or amplifier due to strong spatial hole-burning effects, depending on the pump intensity.

Van Beijnum *et al.* [90] demonstrated laser emission in the near infrared from an array of subwavelength holes in a Au film on an optically pumped InGaAs/InP gain medium at 150 K. Linewidth narrowing and lasing threshold were observed with increasing pump power, and surface plasmon lasing was justified by experimental observations.

Highly directional single-mode spasing at red wavelengths ( $\lambda \sim 620$  nm) was demonstrated at room temperature by Meng *et al.* [91], where the plasmonic nano-cavity was formed by a periodic subwavelength hole array perforated in a Ag film supporting SPP Bloch waves at  $\lambda \sim 620$  nm. They suggested that the optical feedback for spasing was provided by SPP Bloch waves in the hole array nano-cavity rather than the plasmonic resonance in individual holes.

### **1.5.8 Thesis scope and outline**

This thesis aims to investigate incorporation of optical gain in the form of optically-pumped IR-140 doped PMMA in a two-dimensional LRSPP structure based on stepped-in-width metal stripe, to develop and demonstrate active LRSPP devices with interesting applications at near

infrared. Theoretical and experimental studies are conducted to characterize and evaluate the gain media for plasmonic applications. Active LRSPP devices based on the described gain media are proposed and designed. Transmission matrix method (TMM) and Coupled-mode theory are widely used in this thesis for Bragg grating design and simulation.

This thesis consists of a collection of scientific articles, each of them presented as a chapter. The remainder of this document is organized as follows. Chapter 2 describes design of single mode DBR and DFB lasers operating in LRSPP structure. The devices' architecture and design methodology is discussed in this chapter. Also, the IR-140 doped PMMA gain media is theoretically modelled and LRSPP mode power gain is derived. Single mode lasing, low noise performance and thermal tuning are the key properties of the LRSPP lasers proposed and designed in this chapter. In chapter 3, IR-140 doped PMMA is investigated experimentally and the maximum material gain versus the pump intensity, dye concentration in the PMMA, and the pump polarization in the PMMA is identified. The experimental work is based on variable stripe length (VSL) method in which the output amplified spontaneous emission (ASE) intensity that is collected from the gain PMMA slab waveguide is proportional to the length of the pump stripe applied on the gain media. In chapter 4, Ag and Au DFB lasers are designed and optimized in a non-uniform LRSPP structure. Fabrication processes are described and scanning electron microscope and atomic force microscope images of Ag and Au DFB patterns are presented. Moreover, Ag and Au DFBs are tested and results including, lasers' L-L curves, emission spectra, and output facet's mode profile are presented. Chapter 5 introduces the concept of PT symmetry in optics and its importance in suggesting extraordinary optical phenomena. Two different PT symmetric Bragg gratings based on LRSPP waveguides are proposed and designed in this chapter. Asymmetric reflectance with high contrast ratio is demonstrated theoretically in

these structures by operating the PT symmetric Bragg gratings near a so-called exceptional point. A journal article co-authored with Choloong Hahn on unidirectional PT symmetry Bragg gratings is also presented in chapter 5 providing a comprehensive literature review on optical PT symmetric systems with emphasis on the group and energy velocity dispersion behavior near the PT symmetry breaking threshold. Conclusion and future work are provided finally in chapter 6.

## **2. Long-range surface plasmon single-mode laser concepts**

### **2.1 Summary**

Single mode double-DBR, single-DBR and DFB lasers are proposed at near infrared in a LRSPP waveguide consisting a 20 nm-thick, 1  $\mu\text{m}$ -wide Ag stripe bounded by a layer of IR-140 doped PMMA on top and a passive index-matched cladding on the bottom [92]. The index-matched top and bottom claddings enable a symmetric  $ss_b^0$  mode in the waveguide. The Bragg grating used in all proposed devices is implemented by stepping the width of Ag stripe periodically which produces a high reflectance over a very narrow bandwidth. Lasers are designed for  $\lambda_0 = 882$  nm but wavelength tuning is envisioned through current injection into the Ag stripe resulting in thermal modulation of the cladding material's refractive index. Ease of fabrication, and low noise performance in these structures yield useful, cost-effective, near infrared plasmonic sources for optical integrated circuits and improvement of the plasmonic biosensors' performance.

### **2.2 Contribution**

The results provided in this chapter were published in the journal of Applied Physics. I modeled the gain coefficient of IR-140 doped PMMA, derived the LRSPP mode power gain (MPG) and designed LRSPP Bragg gratings using TMM and coupled-mode theories. I generated and interpreted the design and modeling results, and wrote the manuscript. Dr. Tait and Dr. Berini contributed to the device proposal, the interpretation of the results, and revised the manuscript.

### **2.3 Article**

The published article follows verbatim.

## Long-range surface plasmon single-mode laser concepts

Elham Karami Keshmarzi,<sup>1</sup> R. Niall Tait,<sup>1</sup> and Pierre Berini<sup>2</sup>

<sup>1</sup>Department of Electronics, Carleton University, 1125 Colonel By Dr., Ottawa, Ontario, Canada

<sup>2</sup>School of Electrical Engineering and Computer Science, University of Ottawa, 800 King Edward Ave. Ottawa, Ontario, Canada and Department of Physics, University of Ottawa, Ottawa, Ontario, Canada

(Received 9 August 2012; accepted 22 August 2012; published online 21 September 2012)

Near infrared single-mode lasers based on long-range surface plasmon-polariton waveguides and step-in-width Bragg gratings implemented with thin Ag stripes are proposed. The gain medium assumed is a polymer (poly(methylmethacrylate)) doped with organic laser dye molecules (IR-140). Three cavity resonator configurations have been investigated based on distributed feedback or distributed Bragg reflectors. Narrow line-width single-mode lasing is guaranteed by appropriately trading-off the length of the active region against the threshold lasing gain and designing gratings of sufficiently narrow bandwidth. Laser wavelength tuning through thermal modulation of the polymer refractive index by injecting current along the Ag gratings is briefly described. © 2012 American Institute of Physics. [http://dx.doi.org/10.1063/1.4754417]

### I. INTRODUCTION

A thin narrow metal stripe embedded in a homogeneous dielectric medium supports a long-range surface plasmon polariton (LRSPP) mode over a broad optical wavelength range.<sup>1</sup> This mode exhibits useful characteristics such as low attenuation relative to conventional SPPs and efficient end-fire coupling to optical fibres. Thoughtful selection of stripe dimensions (width and thickness) ensures propagation in a single LRSPP mode with good confinement. Several passive elements including Bragg gratings have been implemented and operated in this mode.<sup>1</sup> Step-in-width gratings, where the stripe width is stepped over a length, can produce a high reflectance (>90%) over a narrow bandwidth (FWHM <1 nm).<sup>2,3</sup> Such gratings can be tuned thermally by injecting current along the metal to heat the claddings with near-perfect overlap with the LRSPP mode (cf. Ref. 4). These attributes along with ease of fabrication render the gratings attractive as distributed Bragg reflectors (DBRs) for external cavity lasers (ECLs), or as the feedback element in distributed feedback (DFB) lasers.

Incorporating gain media with SPP structures is of strong current interest to compensate loss or enable novel sources.<sup>5-7</sup> Specifically, several studies have been conducted on compensating the propagation loss of LRSPPs by introducing gain into a cladding, culminating in the recent demonstration of net LRSPP amplification<sup>8,9</sup> and oscillation.<sup>10</sup> Although it is natural to combine SPP gratings with amplification to create a laser, little has been done along this direction. Reports include far-infrared DFB lasers based on quantum-cascade active materials integrated with a step-in-thickness metal grating,<sup>11</sup> a proposal for integrating gain with a corrugated LRSPP grating,<sup>12</sup> and a multimode ECL using a step-in-width LRSPP DBR.<sup>13</sup>

In this paper, we propose 3 single-mode LRSPP near-infrared lasers based on step-in-width Bragg gratings. The first 2 lasers employ DBRs in the ECL architecture while the third is based on the DFB configuration.

### II. LASER CONCEPTS

A 3D sketch of the 1st laser configuration is shown in Fig. 1(a). A thin Ag stripe LRSPP waveguide is employed in the laser's active region and in DBRs constituting the cavity. In the active region (of length  $L_A$ ), the Ag stripe is bounded by a layer of IR-140 doped (PMMA) poly-methylmethacrylate on top and by a passive index-matched cladding on the bottom (e.g., undoped PMMA on Si or FK51A glass substrate<sup>14</sup>) to provide the refractive index symmetry around the Ag stripe which is necessary to support LRSPPs.<sup>1</sup> Undoped PMMA covers the structure. Using two DBRs to define the cavity allows wide laser tunability.<sup>15</sup>

The 2nd configuration is the same as the 1st except that one of the DBRs is replaced by a high reflection coating (HRC). This configuration shortens the laser cavity (increasing the mode spacing) at the expense of less tunability. The 3rd configuration consists of a step-in-width grating overlapping the active region over the full length to produce a DFB laser. The DFB laser has better single-mode performance

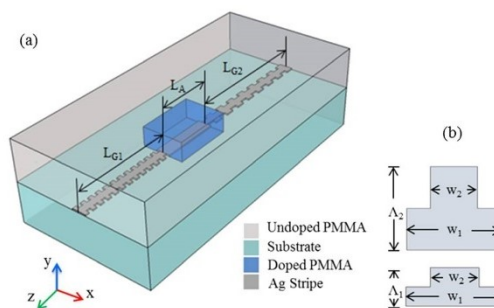


FIG. 1. (a) 3D sketch of a LRSPP laser using 1st and 3rd order DBRs of length  $L_{G1}$  and  $L_{G2}$ , bounding the amplifying region of length  $L_A$ . An optical pump is assumed applied to the top. (b) Top view of the fundamental cell of DBR<sub>2</sub> (3rd order,  $A_2$ ) and DBR<sub>1</sub> (1st order,  $A_1$ ).

compared to DBR (ECL) lasers because its center wavelength has a lower threshold gain than other longitudinal modes; however, it is less tunable.<sup>16</sup>

Conveniently, the 3 configurations can be tuned thermally by heating the gratings directly. Thermal tuning is very efficient (due to near-perfect overlap between the thermal distribution and the LRSPP mode<sup>4</sup>) and cost effective. The proposed devices are also convenient in terms of fabrication. The structures can be fabricated by spin-coating/curing the claddings and evaporation/lift-off for the single-layer Ag features; the lasers should thus be inexpensive and disposable. These lasers should also have low noise performance, since corresponding LRSPP amplifiers have produced a low noise figure due to the low spontaneous emission rate of dipoles into LRSPPs.<sup>17</sup> These low noise optical lasers could be used in optical integrated circuits and to improve the performance of biosensors.

The lasers' active region is taken as a PMMA layer doped with dye, particularly IR-140 for which gain has been demonstrated in the near infrared.<sup>18,19</sup> (IR-140 and PMMA can be dissolved in a common solvent, e.g., dichloromethane<sup>18,19</sup>.) The desired free-space lasing wavelength is  $\lambda_0 = 882$  nm, which was the operating wavelength in our previous work with IR-140 in solvent.<sup>8</sup> At this wavelength a  $1 \mu\text{m}$  wide  $20$  nm thick Ag stripe provides a good compromise between LRSPP confinement and attenuation, along with good overlap to a butt-coupled single-mode fibre. The thickness of the active PMMA layer is chosen as  $2 \mu\text{m}$ , which is sufficient to contain the top half of the LRSPP. This layer is perpendicularly pumped through the top by an appropriate source to excite IR-140 and enable stimulated emission of LRSPPs in our laser. The pump irradiance along with the dye's concentration and quantum efficiency determine the gain of the medium.

### A. Modal gain calculations

To perform modal gain calculation, the refractive index of the layers in the active region is required. The refractive indices of PMMA, FK51A and Ag were obtained from Ref. 20 at  $\lambda_0 = 882$  nm. The refractive index of doped PMMA was calculated following Ref. 21, where the small-signal amplification coefficient of a dye gain medium is related to the pump irradiance, dye concentration, and dye photophysical parameters, via<sup>21</sup>

$$\alpha_e = N \frac{I_p \tau \sigma_p \sigma_e - \sigma_a \hbar \omega_p}{\hbar \omega_p + I_p \tau \sigma_p}, \quad (1)$$

where  $N$  is the total dye molecular density,  $I_p$  is the pump irradiance,  $\tau$  is the excited-state lifetime,  $\sigma_e$  and  $\sigma_a$  are, respectively, the emission and absorption cross-sections at  $\lambda_e$ ,  $\sigma_p$  is the absorption cross section at  $\lambda_p$ ,  $\omega_p$  is the pump angular frequency, and  $\hbar$  is the reduced Planck constant.  $\lambda_e$  and  $\lambda_p$  are dye emission and absorption wavelengths, respectively. The photophysical parameters of IR-140 were obtained from Ref. 8, as  $\tau = 240$  ns,  $\sigma_p \approx 5.7 \times 10^{-16}$  cm<sup>2</sup>, and  $\sigma_a \approx 4 \times 10^{-16}$  cm<sup>2</sup>. These parameters have been measured using pump and probe sources at  $\lambda_p = 808$  nm and

$\lambda_e = 882$  nm, respectively. The small-signal amplification coefficient is found versus dye molecular density and pump intensity (Eq. (1)), from which the relative permittivity of the doped PMMA is obtained as<sup>21</sup>

$$\varepsilon_{r,e} = \varepsilon'_{r,e} + i \frac{\lambda_e}{2\pi} \alpha_e \sqrt{\varepsilon'_{r,e}}, \quad (2)$$

where  $\varepsilon'_{r,e}$  is the relative permittivity of the host medium (PMMA). After finding the relative permittivity of the doped PMMA, the gain of the propagating mode (LRSPP) in the active region can easily be computed using an appropriate numerical method.

Generally, for dye molecules above a metallic interface, the excited-state lifetime is dependent on the distance between the molecules and the interface. The lifetime position dependence shows an oscillatory behaviour due to interference between directly radiated emission and that being reflected from the metal, and due to different decay channels becoming active at different distances from the metal interface.<sup>22</sup> For distances above  $1 \mu\text{m}$ , the main decay is into radiative modes of the structure and the lifetime is practically unaffected, whereas for distances below about  $10$  nm, the main decay is the creation of electron-hole pairs in the metal, strongly quenching emission.<sup>8</sup> Under perpendicular incidence, the pump flux intensity in the dye-doped medium exhibits standing wave behaviour due to reflection from the metal.<sup>21</sup>

In this paper, for simplicity, we treated the pump irradiance as uniform as it enters the medium. We also neglected the position dependence of the dye lifetime. This overestimates the mode power gain (MPG) of the LRSPP but in practice ample pump power is available.

The LRSPP MPG was calculated versus pump irradiance and dye concentration for the Ag stripe of interest, using a commercial mode solver based on the finite element method, and is plotted in Fig. 2. We find, e.g., that a  $1$  mM dye concentration and a modest  $500$  kW/cm<sup>2</sup> pump irradiance yields  $\text{MPG} \approx 20$  cm<sup>-1</sup>. Under these conditions, the LRSPP's effective index is  $n_{\text{eff}A} = 1.48413 + j1.043 \times 10^{-4}$  ( $e^{-j\omega t}$  time harmonic form implied,  $\text{MPG} = 2\text{Im}\{n_{\text{eff}A} \times 2\pi/\lambda_0\}$ ).

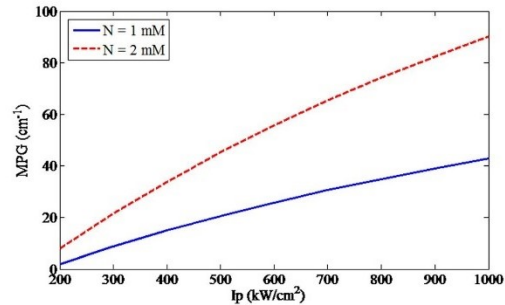


FIG. 2. Computed LRSPP MPG versus pump irradiance and dye concentration at  $\lambda_0 = 882$  nm for a  $1 \mu\text{m}$  wide  $20$  nm thick Ag stripe covered by  $2 \mu\text{m}$  of doped PMMA on FK51A glass.

## B. ECL configurations

In the ECL configuration, gratings are separated from the active region. In configuration 1, passive uniform 1st and 3rd order DBRs are obtained by stepping the width of the Ag stripe periodically over the lengths  $L_{G1}$  and  $L_{G2}$  respectively (Fig. 1(a)). The unit cell of both gratings (Fig. 1(b)) is selected as a concatenation of stripes of width  $w_1 = 1 \mu\text{m}$  and  $w_2 = 0.5 \mu\text{m}$  of equal length (50% duty cycle). The LRSPP propagates over stripes of such width with effective indices  $n_{eff1} = 1.48413 - j2.823 \times 10^{-5}$  and  $n_{eff2} = 1.48312 - j5.526 \times 10^{-6}$  at  $\lambda_0 = 882 \text{ nm}$ . The period  $\Lambda$  of a grating is related to its Bragg wavelength  $\lambda_B$  via<sup>3</sup>

$$\lambda_B = \frac{2n_{ave}\Lambda}{O}, \quad (3)$$

where  $O$  is an integer ( $O \geq 1$ ) corresponding to the order of the grating and  $n_{ave}$  is the average of the real effective indices in the grating, i.e.,  $n_{ave} = \text{Re}\{n_{eff1} + n_{eff2}\}/2 = 1.4836$ . Figs. 3(a) and 3(b) plot the LRSPP's main transverse electric field component ( $|E_y|$ ) over stripe cross-sections of width  $w_1 = 1 \mu\text{m}$  and  $w_2 = 0.5 \mu\text{m}$ .

The LRSPP resembles a  $y$ -polarised plane wave propagating longitudinally along the stripe with most of its fields residing in the background dielectric.<sup>1</sup> A simple equivalent dielectric stack model can thus be applied to model the gratings.<sup>3</sup> In this model, each stripe section of width  $w_i$  ( $i = 1, 2$ ) is equivalent to a dielectric layer of refractive index equal to the complex effective index of the mode on the stripe  $n_{effi}$  ( $i = 1, 2$ ) and of thickness equal to the corresponding length of stripe. The equivalent stack is then analysed by the transmission matrix method (TMM) under perpendicular incidence to determine the reflectance/transmittance of the gratings.<sup>3</sup>

The length of the active region and of the gratings ( $L_A$ ,  $L_{G1}$ ,  $L_{G2}$ ), along with the period of the gratings ( $\Lambda_1$ ,  $\Lambda_2$ ), and the threshold gain, must be determined. This is carried out by ensuring that the lasing gain and phase conditions<sup>16</sup> are met. The gain condition dictates the gain required from the active region to overcome the total loss of the laser. In other words, the total round-trip gain of the medium must exceed the overall round-trip loss. This leads to the following condition on the MPG:

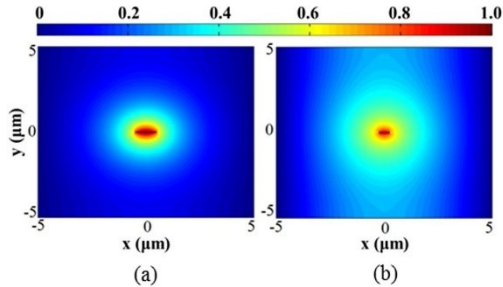


FIG. 3.  $|E_y|$  of the LRSPP at  $\lambda_0 = 882 \text{ nm}$  on (a)  $w_1 = 1 \mu\text{m}$  Ag stripe and (b)  $w_2 = 0.5 \mu\text{m}$  Ag stripe. The stripe is  $20 \text{ nm}$  thick in both cases.

$$MPG > \frac{1}{2L_A} \ln\left(\frac{1}{|R_1 R_2|}\right), \quad (4)$$

where  $R_1$  and  $R_2$  are the complex reflectance of DBR<sub>1</sub> and DBR<sub>2</sub>. We choose  $|R_1| = 0.85$  for the highly reflective DBR<sub>1</sub>, and  $|R_2| = 0.45$  for the partially reflective DBR<sub>2</sub> from which the output is taken. Using these values with  $MPG = 20 \text{ cm}^{-1}$  (Fig. 2) in Eq. (4) gives the minimum length of the active region as  $L_A > 240 \mu\text{m}$ .

The maximum length  $L_A$  is limited by the phase condition and the requirement for single-mode lasing. The phase condition, which specifies the laser's longitudinal resonance frequencies, states that lasing can occur only at frequencies where the round-trip phase is equal to multiple integers of  $2\pi$ ; i.e.,  $2\beta_A L_A - \varphi_{G1} - \varphi_{G2} = 2\pi q$ , where  $q$  is an integer,  $\beta_A$  is the phase constant of the LRSPP in the active region ( $\beta_A = \text{Re}\{n_{effA} \times 2\pi/\lambda_0\}$ ), and  $\varphi_{G1}$  and  $\varphi_{G2}$  are the reflectance phases of DBR<sub>1</sub> and DBR<sub>2</sub>, respectively. Manipulation of the phase condition identifies the laser's resonance frequencies as

$$\nu_q = \frac{qc_0}{2L_T}, \quad (5)$$

where  $c_0$  is the speed of light in free space and

$$L_T = \text{Re}\{n_{effA}\}L_A + \text{Re}\{n_{effG1}\}L_{effG1} + \text{Re}\{n_{effG2}\}L_{effG2} \quad (6)$$

is the total effective length of the laser,  $\text{Re}\{n_{effG1}\} = \text{Re}\{n_{effG2}\} = n_{ave}$  are the LRSPP's average effective index in DBR<sub>1</sub> and DBR<sub>2</sub>,  $L_{effG1} = -\partial\varphi_{G1}/\partial\beta_{G1}$  and  $L_{effG2} = -\partial\varphi_{G2}/\partial\beta_{G2}$  are the effective lengths of DBR<sub>1</sub> and DBR<sub>2</sub>, and  $\beta_{G1}$  and  $\beta_{G2}$  are the phase constants of the LRSPP thereon ( $\beta_{G1} = \beta_{G2} = n_{ave} \times 2\pi/\lambda_0$ ). Equation (5) implies a resonant mode spacing (in terms of wavelength) of

$$\Delta\lambda_0 \approx \frac{\lambda_0^2}{2L_T}. \quad (7)$$

The number of lasing modes is given by  $M = 1 + \Delta\lambda_B/\Delta\lambda_0$ , where  $\Delta\lambda_B$  is the bandwidth overlap between DBR<sub>1</sub> and DBR<sub>2</sub>. It is required that  $M < 2$  (i.e.,  $\Delta\lambda_B < \Delta\lambda_0$ ) in order to obtain single-mode lasing.

DBR<sub>1</sub> and DBR<sub>2</sub> were designed to have their Bragg wavelengths close to the desired lasing wavelength  $\lambda_B = \lambda_0 = 882 \text{ nm}$ . From Eq. (3), the period of DBR<sub>1</sub> and DBR<sub>2</sub> are obtained as  $\Lambda_1 = 297.2 \text{ nm}$  and  $\Lambda_2 = 891.7 \text{ nm}$ . Using the TMM, the number of unit cells required to produce  $|R_1| = 0.85$  and  $|R_2| = 0.45$  were found to be  $N_1 = 3200$  and  $N_2 = 1500$ . The physical length, effective length, and FWHM of these DBRs were deduced as  $L_{G1} = 951.2 \mu\text{m}$ ,  $L_{effG1} = 212.7 \mu\text{m}$ ,  $\Delta\lambda_{BG1} = 0.56 \text{ nm}$ , and  $L_{G2} = 1337.6 \mu\text{m}$ ,  $L_{effG2} = 504.5 \mu\text{m}$ ,  $\Delta\lambda_{BG2} = 0.22 \text{ nm}$ . The FWHM of DBR<sub>2</sub> is narrower and taken as the bandwidth overlap with DBR<sub>1</sub> ( $\Delta\lambda_B = \Delta\lambda_{BG2}$ ). For single-mode lasing, it is thus required that  $\Delta\lambda_0 > 0.22 \text{ nm}$ , which, from Eqs. (6) and (7), implies that  $L_A < 475 \mu\text{m}$ . We chose  $L_A = 400 \mu\text{m}$ , which yields  $L_T = 1660 \mu\text{m}$  and  $\Delta\lambda_0 = 0.23 \text{ nm}$  or  $M = 1.95$ , guaranteeing single-mode lasing.

At this point, our rationale for choosing 1st and 3rd order gratings to implement the DBRs should be clear: The 1st order grating produces a strong reflectance in a short length whereas the 3rd order grating produces less reflectance (the output is taken from this port) over a narrower bandwidth. The reflection bandwidth is given by the width of the bandgap as<sup>23</sup>

$$\Delta\lambda_B = \frac{4\lambda_B}{O\pi} \sin^{-1} \left( \frac{\Delta n_{eff}}{2n_{ave}} \right), \quad (8)$$

where  $\Delta n_{eff} = |n_{eff1} - n_{eff2}|$ . For gratings of similar  $\Delta n_{eff}$  and  $n_{ave}$ , the bandwidth drops with increasing order  $O$ . Thus, using a 3rd order grating for DBR<sub>2</sub> makes it easier to satisfy the single-mode lasing condition ( $M < 2$ ).

Fig. 4(a) gives the location of the cavity modes and plots the reflection response of DBR<sub>1</sub> and DBR<sub>2</sub>. It is noted that the desired lasing wavelength (882 nm) coincides with a cavity mode and that only one of the latter overlaps with DBR<sub>2</sub> thus confirming single-mode lasing.

In the 2nd configuration, DBR<sub>1</sub> is replaced with a HRC with everything else remaining the same. The total effective length of the laser is then reduced to  $L_T = 1310 \mu\text{m}$ . Consequently,  $\Delta\lambda_0 = 0.29 \text{ nm}$ ,  $M = 1.75$ , and the single-mode

lasing condition is satisfied with greater margin. Fig. 4(b) shows the position of the cavity modes and the reflection response of DBR<sub>2</sub>.

### C. DFB configuration

In the 3rd configuration, the DBRs are removed altogether and a uniform 1st order grating is distributed under the active region, both extending over the full length, forming a DFB laser. Analysis of this structure is carried out by coupled mode theory<sup>24</sup> which states that a periodic perturbation of the medium generates an infinite set of diffraction modes. In the vicinity of  $\lambda_B$ , only two modes are phase synchronous: they are counter-propagating (forward and backward) modes which amplify due to the gain medium and couple energy to each other via Bragg scattering.

The periodic perturbation of a DFB laser can be represented as a Fourier series of the refractive index and gain constant of the structure<sup>24</sup>

$$n(z) = n + n_1 \cos(2\beta_\Lambda z), \quad (9a)$$

$$\alpha(z) = \alpha + \alpha_1 \cos(2\beta_\Lambda z), \quad (9b)$$

where  $n$  and  $\alpha$  are the average real refractive index and gain constant of the medium and  $n_1$  and  $\alpha_1$  are the real refractive index and gain constant spatial modulation;  $\beta_\Lambda = \pi/\Lambda$  is the grating constant. The coupling coefficient determines the strength of feedback (per unit length) provided by the structure and is given by  $\kappa = \pi n_1/\lambda_B + j\alpha_1/2$ . In our DFB laser, we used a 1st order grating similar in design to DBR<sub>1</sub> (20 nm thick Ag stripe uniformly stepped in width from  $w_1 = 1 \mu\text{m}$  to  $w_2 = 0.5 \mu\text{m}$  with a 50% duty cycle,  $\lambda_B = 882 \text{ nm}$ ) and we assumed the same gain medium as in the 1st configuration. The effective indices of the LRSPP in the stripe sections of the unit cell were computed as  $n_{eff1} = 1.4841 + j1.7153 \times 10^{-4}$  and  $n_{eff2} = 1.4834 + j1.2884 \times 10^{-4}$ , respectively. Thus, the average and spatial modulations of the real refractive index and gain constant are obtained as  $n = 1.4838$ ,  $n_1 = 5.048 \times 10^{-4}$  and  $\alpha = 21.4 \text{ cm}^{-1}$ ,  $\alpha_1 = 1.936 \text{ cm}^{-1}$ , respectively, from which the coupling coefficient of the DFB laser is determined as  $\kappa = 18 + j1 \text{ cm}^{-1}$ . This coupling coefficient reveals that index coupling is greater than gain coupling ( $\text{Re}\{\kappa\} \gg \text{Im}\{\kappa\}$ ). Fig. 8 of Ref. 24 gives a plot of the gain at threshold versus the coupling strength for various longitudinal modes in the case of index coupling; for operation in the first longitudinal mode, we find from this figure that  $1.2 < \alpha L < 1.8$ , where  $L$  is the physical length of the DFB. Using  $\alpha = 21.4 \text{ cm}^{-1}$  yields  $561 \mu\text{m} < L < 841 \mu\text{m}$ .

### D. Thermal tuning

Thermal tuning of all configurations is possible by injecting current along the Ag stripe and gratings, thereby increasing the temperature of the claddings. Raising the temperature of PMMA by  $100^\circ\text{C}$  would decrease its refractive index by  $\sim 0.012$ .<sup>25</sup> A simple analysis shows that this decrease blue-shifts  $\lambda_B$  by  $\sim 8 \text{ nm}$ . This range may be extended by using sampled gratings and Vernier leveraging in configuration 1, following Ref. 15, and mode-hop free

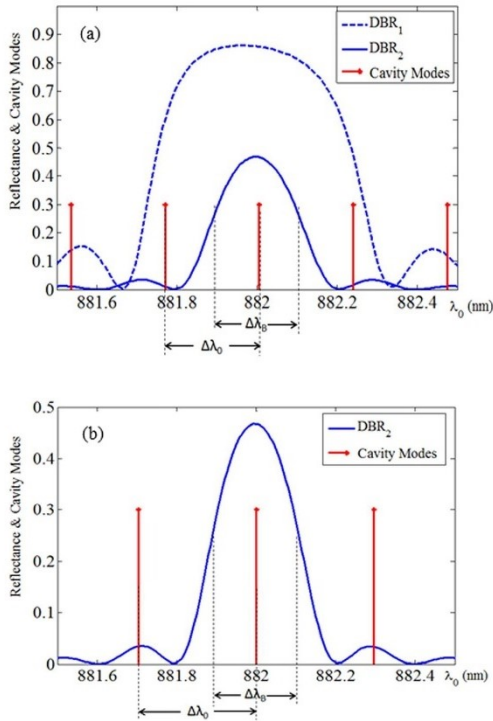


FIG. 4. (a) Location of cavity modes and reflection response of DBR<sub>1</sub> (1st order) and DBR<sub>2</sub> (3rd order) for the 1st LRSPP laser configuration. (b) Same as (a) but for the 2nd LRSPP laser configuration.

operation could be ensured by heating the stripe in the active region simultaneously using it as a phase shifter.

### III. CONCLUSION

In summary, we have proposed three single-mode LRSPP lasers, operating near  $\lambda_0 = 882$  nm, based on step-in-width Ag stripe gratings, and IR-140 doped PMMA. Laser tuning via thermal modulation of the refractive index of PMMA can be conveniently achieved by injecting current directly along the gratings. The lasers should be attractive as a low-cost tunable and disposable high-quality source, and can be integrated with other LRSPP or integrated circuit elements.

<sup>1</sup>P. Berini, *Adv. Opt. Photon* **1**, 484 (2009).

<sup>2</sup>S. Jetté-Charbonneau, R. Charbonneau, N. Lahoud, G. Mattiussi, and P. Berini, *Opt. Express* **13**, 4674 (2005).

<sup>3</sup>S. Jetté-Charbonneau and P. Berini, *J. Opt. Soc. Am. A* **23**, 1757 (2006).

<sup>4</sup>G. Gagnon, N. Lahoud, G. A. Mattiussi, and P. Berini, *J. Lightwave Technol.* **24**, 4391 (2006).

<sup>5</sup>D. J. Bergman and M. I. Stockman, *Phys. Rev. Lett.* **90**, 027402 (2003).

<sup>6</sup>P. Berini and I. De Leon, *Nature Photon* **6**, 16 (2012).

<sup>7</sup>R. F. Oulton, *Mater Today* **15**, 26 (2012).

<sup>8</sup>I. De Leon and P. Berini, *Nature Photon.* **4**, 382 (2010).

<sup>9</sup>M. C. Gather, K. Meerholz, N. Danz, and K. Leosson, *Nature Photon.* **4**, 457 (2010).

<sup>10</sup>R. A. Flynn, C. S. Kim, I. Vurgaftman, M. Kim, J. R. Meyer, A. J. Mäkinen, K. Bussmann, L. Cheng, F. S. Choa, and J. P. Long, *Opt. Express* **19**, 8954 (2011).

<sup>11</sup>A. Tredicucci, C. Gmachl, F. Capasso, A. L. Hutchinson, D. L. Sivco, and A. Y. Cho, *Appl. Phys. Lett.* **76**, 2164 (2000).

<sup>12</sup>T. Okamoto, F. H'Dhili, and S. Kawata, *Appl. Phys. Lett.* **85**, 3968 (2004).

<sup>13</sup>S. Jetté-Charbonneau and P. Berini, *App. Phys. Lett.* **91**, 181114 (2007).

<sup>14</sup>H. Bach and N. Neuroth, *The Properties of Optical Glass* (Springer, Berlin, 1998).

<sup>15</sup>L. Coldren, *IEEE J. Sel. Top. Quantum Electron.* **6**, 988 (2000).

<sup>16</sup>L. A. Coldren and S. W. Corzine, *Diode Lasers and Photonic Integrated Circuit* (Wiley, Toronto, 1995).

<sup>17</sup>I. De Leon and P. Berini, *Phys. Rev. B.* **83**, 081414(R) (2011).

<sup>18</sup>J. Thompson, M. Anni, S. Lattante, D. Pisignano, R. I. R. Blyth, G. Gigli, and R. Cingolani, *Synth. Met.* **143**, 305 (2004).

<sup>19</sup>P. Del Carro, A. Camposeo, R. Stabile, E. Mele, and L. Persano, *Appl. Phys. Lett.* **89**, 201105 (2006).

<sup>20</sup>See [www.refractiveindex.info](http://www.refractiveindex.info) for refractive indices of materials as a function of wavelength.

<sup>21</sup>I. De Leon and P. Berini, *Phys. Rev. B.* **78**, 161401R (2008).

<sup>22</sup>G. W. Ford and W. H. Weber, *Phys. Rep.* **113**, 195 (1984).

<sup>23</sup>P. Yeh, *Optical Waves in Layered Media* (Wiley, Toronto, 1988).

<sup>24</sup>H. Kogelnik and C. V. Shank, *J. Appl. Phys.* **43**, 2327 (1972).

<sup>25</sup>J. M. Cariou, J. Dugas, L. Martin, and P. Michel, *Appl. Opt.* **25**, 334 (1986).

### **3. Gain characterization of IR-140 doped PMMA slab waveguides**

#### **3.1 Summary**

Organic gain media are greatly attractive for their large transition cross section and wide chemical tunability and new organic lasers have been developed with great potential in integrated optics applications [93]. The gain behaviour of optically-pumped, solid-state IR-140 doped PMMA was experimentally characterized for applications in active LRSPP structures [94]. Thin, IR-140 doped PMMA films were created on SiO<sub>2</sub> substrate by spin coating and curing and cleaving the sample's to produce a good quality optical facet. The optical pump was perpendicularly applied to the gain film from the top using a cylindrical lens and a variable slit to form a 300 μm-wide pump stripe of variable length on the sample. Pump intensity varies from ~ 1 mJ/cm<sup>2</sup> to ~ 45 mJ/cm<sup>2</sup> and its polarization can be parallel with or perpendicular to the pump stripe. The output amplified spontaneous emission (ASE) was passed through an objective followed by a polarizer and sent to a spectrograph. A variable stripe length (VSL) method was used to derive the ASE gain coefficient with respect to the pump intensity and pump polarization for gain films of different dye concentrations. Maximum available gain and gain anisotropy were derived and discussed.

#### **3.2 Contribution**

The results provided in this chapter were published by OSA in the journal of Optics Express. I fabricated the slab waveguides, designed and implemented the experimental setup, generated the experimental results, and fit them to the theoretical models. I also interpreted the results, and wrote the manuscript. Dr. Tait and Dr. Berini contributed to the interpretation of the results, and revised the manuscript.

#### **3.3 Article**

## Near infrared amplified spontaneous emission in a dye-doped polymeric waveguide for active plasmonic applications

Elham Karami Keshmarzi,<sup>1,2</sup> R. Niall Tait,<sup>1</sup> and Pierre Berini<sup>2,3,4,\*</sup>

<sup>1</sup>Department of Electronics, Carleton University, 1125 Colonel by Dr., Ottawa, Canada

<sup>2</sup>School of Electrical Engineering and Computer Science, University of Ottawa, 800 King Edward Ave., Ottawa, Canada

<sup>3</sup>Department of Physics, University of Ottawa, Ottawa, Canada

<sup>4</sup>Centre for Research in Photonics at the University of Ottawa, Ottawa, Canada  
berini@eecs.uottawa.ca

**Abstract:** Near-infrared amplified spontaneous emission (ASE) from an optically-pumped dye-doped polymeric slab waveguide, consisting of IR-140 in PMMA on a glass substrate, has been characterised. The ASE gain was measured using the variable stripe length method. Linewidth narrowing with increasing pump intensity was observed, indicating ASE gain in this material. The effects of the dye concentration and pump intensity on the gain were investigated under linear operation. The maximum achieved gain coefficient is  $\gamma \sim 68 \text{ cm}^{-1}$  for a film with 0.8wt % of IR-140 to PMMA for a pump intensity of  $43.4 \text{ mJ/cm}^2$ . The polarisation dependence of the ASE gain was also investigated by measuring the gain coefficient of orthogonal TE and TM modes and varying the pump polarisation relative to the amplifier length. It was observed that there is some degree of gain anisotropy when the pump polarisation is aligned perpendicular to the length, but that the gain was isotropic when the pump polarisation is aligned parallel the length. The applicability of IR-140 doped PMMA for active plasmonic applications is discussed.

©2014 Optical Society of America

OCIS codes: (250.5403) Plasmonics; (250.4480) Optical amplifiers.

### References and links

1. S. Chénais and S. Forget, "Recent advances in solid-state organic lasers," *Polym. Int.* **61**(3), 390–406 (2012).
2. V. G. Kozlov, V. Bulović, P. E. Burrows, and S. R. Forrest, "Laser action in organic semiconductor waveguide and double-heterostructure devices," *Nature* **389**(6649), 362–364 (1997).
3. G. Somasundaram and A. Ramalingam, "Gain studies of Rhodamine 6G dye doped polymer laser," *J. Photochem. Photobiol. A* **125**(1-3), 93–98 (1999).
4. T. Grossmann, S. Schleede, M. Hauser, M. B. Christiansen, Ch. Vannahme, C. Eschenbaum, S. Klinkhammer, T. Beck, J. Fuchs, G. U. Nienhaus, U. Lemmer, A. Kristensen, T. Mappes, and H. Kalt, "Low-threshold conical microcavity dye lasers," *Appl. Phys. Lett.* **97**(6), 063304 (2010).
5. M. Karimi, N. Granpayeh, and M. K. Morraveg Farshi, "Analysis and design of a dye-doped polymer optical fiber amplifier," *Appl. Phys. B* **78**(3-4), 387–396 (2004).
6. A. Costela, O. García, L. Cerdán, I. García-Moreno, and R. Sastre, "Amplified spontaneous emission and optical gain measurements from pyrromethene 567--doped polymer waveguides and quasi-waveguides," *Opt. Express* **16**(10), 7023–7036 (2008).
7. J. Thompson, M. Anni, S. Lattante, D. Pisignano, R. I. R. Blyth, G. Gigli, and R. Cingolani, "Amplified spontaneous emission in the near infrared from a dye-doped polymer thin film," *Synth. Met.* **143**(3), 305–307 (2004).
8. K. Yamashita, T. Kuro, K. Oe, and H. Yanagi, "Low threshold amplified spontaneous emission from near-infrared dye doped polymeric waveguide," *Appl. Phys. Lett.* **88**(24), 241110 (2006).
9. S. Yuyama, T. Nakajima, K. Yamashita, and K. Oe, "Solid state organic laser emission at 970 nm from dye-doped fluorinated-polyimide planar waveguides," *Appl. Phys. Lett.* **93**(2), 023306 (2008).
10. E. K. Keshmarzi, R. N. Tait, and P. Berini, "Long-range surface plasmon single-mode laser concepts," *J. Appl. Phys.* **112**(6), 063115 (2012).

11. M. A. Noginov, G. Zhu, M. Mayy, B. A. Ritzo, N. Noginova, and V. A. Podolskiy, "Stimulated Emission of Surface Plasmon Polaritons," *Phys. Rev. Lett.* **101**(22), 226806 (2008).
12. J. K. Kitur, V. A. Podolskiy, and M. A. Noginov, "Stimulated Emission of Surface Plasmon Polaritons in a Microcylinder Cavity," *Phys. Rev. Lett.* **106**(18), 183903 (2011).
13. M. C. Gather, K. Meerholz, N. Danz, and K. Leosson, "Net optical gain in a plasmonic waveguide embedded in a fluorescent polymer," *Nat. Photonics* **4**(7), 457–461 (2010).
14. S. Xiao, V. P. Drachev, A. V. Kildishev, X. Ni, U. K. Chettiar, H. K. Yuan, and V. M. Shalaev, "Loss-free and active optical negative-index metamaterials," *Nature* **466**(7307), 735–738 (2010).
15. J. K. Kitur, G. Zhu, Y. A. Barnakov, and M. A. Noginov, "Stimulated emission of surface plasmon polaritons on smooth and corrugated silver surfaces," *J. Opt.* **14**(11), 114015 (2012).
16. S. Kéna-Cohen, P. N. Stavrinou, D. D. C. Bradley, and S. A. Maier, "Confined Surface Plasmon-Polariton Amplifiers," *Nano Lett.* **13**(3), 1323–1329 (2013).
17. I. De Leon and P. Berini, "Surface plasmon-polariton amplifiers and lasers," *Nat. Photonics* **6**, 16–24 (2012).
18. I. De Leon and P. Berini, "Amplification of long-range surface plasmons by a dipolar gain medium," *Nat. Photonics* **4**(6), 382–387 (2010).
19. L. Dal Negro, P. Bettotti, M. Cazzanelli, D. Pacifici, and L. Pavesi, "Applicability conditions and experimental analysis of the variable stripe length method for gain measurements," *Opt. Commun.* **229**(1-6), 337–348 (2004).
20. I. De Leon and P. Berini, "Spontaneous emission in long-range surface plasmon-polariton amplifiers," *Phys. Rev. B* **83**(8), 081414 (2011).
21. G. Somasundaram and A. Ramalingam, "Gain studies of Coumarin 503 dye-doped polymer laser," *Opt. Lasers Eng.* **33**(2), 157–163 (2000).
22. K. C. Reizer and L. W. Casperson, "Polarization characteristics of dye-laser amplifiers II. Isotropic molecular distributions," *J. Appl. Phys.* **51**(12), 6083 (1980).
23. B. Valeur, "Molecular Fluorescence, Principles and Applications," Wiley-VCH, (2002).
24. G. Mourou and M. M. Denariez-Roberge, "Polarization of Fluorescence and Bleaching of Dyes in a High-Viscosity Solvent," *IEEE J. Quantum Electron.* **9**(8), 787–790 (1973).

## 1. Introduction

Solid-state organic lasers and amplifiers based on incorporating dye molecules in an appropriate solid host such as a polymer in the form of a thin film has been an attractive research area over the last decade [1]. Such a medium amplifies at low optical pump intensity with relatively high gain. As a compact, cost-effective and maintenance-free gain medium, these amplifiers are good candidates as an alternative to liquid dye lasers and can be integrated with other optical structures (active or passive) within a planar guided-wave paradigm.

Amplified spontaneous emission and lasing action from dye-doped polymeric films has been researched and observed mostly at visible wavelengths [2–6]; reports on ASE and optical gain of near-infrared emitting molecules are limited. Thompson et al. [7] earlier reported polymer thin films doped with a near-infrared emitting organic dye which generated a maximum gain of  $6.6 \text{ cm}^{-1}$  at 960 nm. Yamashita et al. [8] demonstrated low threshold ASE gain from a polymeric dye-doped waveguide at about 800 nm with a maximum gain of  $35 \text{ cm}^{-1}$ . Yuyama et al. [9] reported ASE gain and lasing from dye-doped fluorinated-polyimide (FPI) waveguides at 970 nm with a low lasing threshold of  $0.22 \text{ mJ/cm}^2$ .

Our motivation is to investigate near-infrared emitting dye-doped polymers as the gain medium for active plasmonic applications, particularly, solid-state long-range surface plasmon polariton (LRSP) lasers and amplifiers [10]. Optically-pumped dye-doped polymer has been used in plasmonic structures to enable stimulated emission of SPPs at visible wavelengths [11–16], but no studies have been reported on near-infrared dye-doped polymers for plasmonics. The near-infrared is of interest because plasmonic systems generally have lower loss in this region of the spectrum compared to the visible, and because many plasmonic applications exist in this range, including biosensors. To be suitable for plasmonic applications a gain medium must exhibit several characteristics, including high gain because plasmonic structures can have high loss, transverse-magnetic (TM) gain because surface plasmons are TM-polarised waves, and the ability to easily integrate the medium with metal features on a substrate [17]. Dye-doped polymers potentially offer all of these characteristics.

IR-140, a commercially available organic dye emitting around 880 nm, had been previously used in solution to form an active medium for LRSP amplifiers [18]. In this paper, we study the ASE properties of optically-pumped thin films of poly (methyl methacrylate) (PMMA) doped with IR-140 deposited on a glass substrate. Our goal is to measure the films' polarisation-dependent and -independent material gains, as a function of IR-140 concentration, pump intensity, and pump polarisation, in order to determine whether this medium is suitable for active plasmonics. In order to investigate the effect of dye concentration on the gain coefficient, four different dye concentrations were used in the films. ASE gain measurements were performed on the films following the variable stripe length method. Several ASE curves were obtained on each sample for incremental pump intensities in order to find the largest gain coefficient before saturation. The polarisation dependence of the ASE was also studied. ASE gain measurements were obtained for TE and TM modes separately, for cases where the pump polarisation was aligned perpendicular or parallel to the pump length (stripe).

## 2. Experiment

### 2.1 Sample preparation and setup

Poly (methyl methacrylate) (PMMA), of average molecular weight ( $M_w$ )  $\sim 350000$ , and IR-140 were purchased from Sigma-Aldrich and Exciton respectively and used as received. Four different solutions were prepared by dissolving 200 mg of PMMA in 2 ml dichloromethane and adding IR-140 to PMMA with a weight ratio of 0.4wt %, 0.8wt %, 1.2wt % and 1.6wt %, respectively. The corresponding IR-140 molecular concentration in the polymer is then  $2.6 \times 10^{18} \text{ cm}^{-3}$ ,  $5.2 \times 10^{18} \text{ cm}^{-3}$ ,  $7.8 \times 10^{18} \text{ cm}^{-3}$  and  $10.4 \times 10^{18} \text{ cm}^{-3}$ , respectively. Solutions were then spin-coated on clean standard microscope glass slides, provided by Fisher Scientific, for 50 sec at 3000 rpm and baked at  $170^\circ\text{C}$  for 2 mins to produce samples A, B, C and D corresponding to the dye concentrations mentioned above. The resulting films' thickness was measured as  $5 \pm 0.3 \mu\text{m}$  using a profilometer. In order to avoid artefacts due to beading of the spin-coated polymer at the glass edge, the glass slides after spin-coating were scribed and broken carefully along the middle, and the emission was collected from the broken edges.

The combination of glass, doped PMMA and air forms an asymmetric slab optical waveguide. At the emission wavelength of IR-140 ( $\sim 880 \text{ nm}$ ), the glass slides have a slightly higher refractive index ( $\sim 1.5$ ) than the doped-PMMA film ( $\sim 1.49$ ) such that the emitted mode leaks slightly into the substrate. However, numerical modeling shows that the fundamental TE and TM modes of the slab exhibit very strong localisation to the dye-doped PMMA film. Although the waveguide is not single-moded, the mode of interest is the fundamental mode.

The fabricated samples are optically pumped at 810 nm using laser pulses of 10 ns duration (FWHM) and 10 Hz repetition rate from a tunable dye laser system (Sirah, Mod. Cobra-Stretch). Figure 1 sketches part of the experimental setup for the ASE measurements showing how the pump beam is applied to the sample. A solid metallic plate attached to an electro-mechanical actuator (SW) is used to blank the pump beam as needed. The output pulse energy and polarisation are controlled with a  $\lambda/2$  wave plate (WP) followed by a Glan-Laser polarizing beam splitter (PBS). Using mirrors  $M_1$  and  $M_2$ , the pump beam is directed to a spherical lens ( $L_1$ ) of  $f = 5 \text{ cm}$  to enlarge the beam's spot on the mirror  $M_3$ . The reflected beam from  $M_3$  is passed through a cylindrical lens ( $L_2$ ) with  $f = 5 \text{ cm}$  to be converted to a narrow stripe. The variable slit (VS) is used to define the width and length of the pump stripe on the dye-doped polymer sample which is located on a fixed sample holder. The slit's width is  $300 \mu\text{m}$  and the length is variable from 0 to 6 mm. Spontaneous emission is gain-guided and amplified along the pump stripe to the sample edge. The pump polarisation on the surface of sample is linear and aligned either along ( $\parallel$ ) or perpendicular ( $\perp$ ) to the pump stripe. A multimode fiber is aligned with the sample edge and the pump stripe to collect the emission.

An optical spectrometer (Newport, Mod. OSM2-400 VIS/NIR), with 1 nm spectral resolution is used to capture and display the spectra.

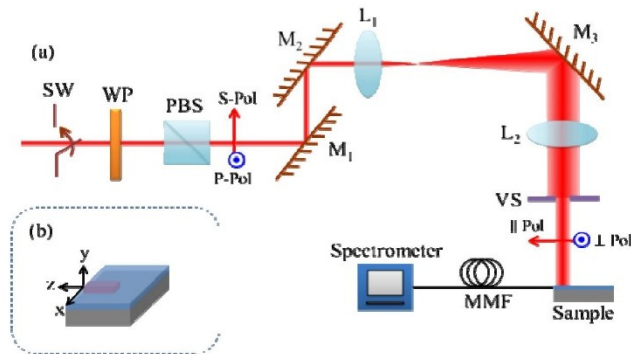


Fig. 1. (a) Experimental setup for ASE gain measurements showing how the pump is applied to the sample under test. (b) 3D sketch of sample with the pump stripe and a reference coordinate.

## 2.2 Measurements and results

The pump beam polarisation is initially set as vertical (S-Pol) using the wave plate (WP) and polarizing beam splitter (PBS) in Fig. 1. In this case the pump polarisation will be parallel to the pump stripe after being reflected from mirror ( $M_3$ ).

In the first step, emission spectra were obtained for samples A, B, C and D at a fixed length of the pump stripe. Figure 2 shows growing ASE spectra with increasing pump energy for a stripe length fixed to 0.635 mm.

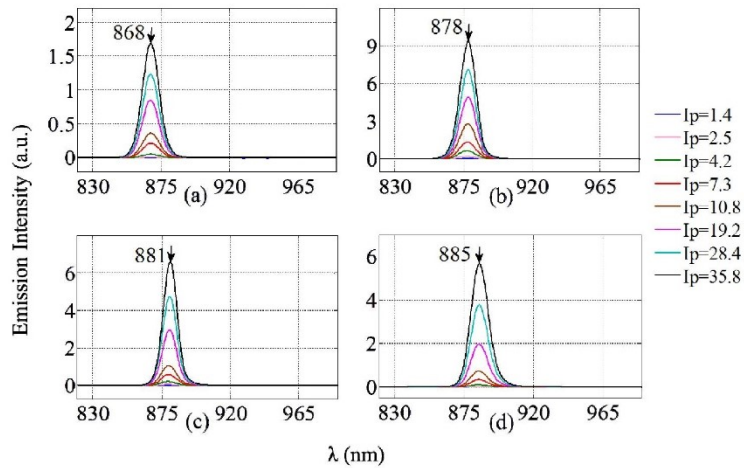


Fig. 2. Growing ASE spectra in optically pumped IR-140-doped polymeric waveguides at various pump intensities ( $\text{mJ}/\text{cm}^2$ ) for (a) Sample A, (b) Sample B, (c) Sample C and (d) Sample D.

By increasing the pump energy the emission spectra grows and the peak emission intensity appears at about 868 nm, 878 nm, 881 nm and 885 nm for films A, B, C and D, respectively. The maximum emission intensity under equal pump energy is observed from film B with 0.8wt % IR-140 to PMMA, whereas film A with 0.4wt % IR-140 to PMMA has the minimum emission intensity. The fluorescence efficiency increases with increasing dye concentration up to 0.8wt %; however, above 0.8wt % other phenomena, such as self-absorption and quenching, contribute to a slow drop in emission intensity. The red-shift in peak emission wavelength could be also attributed to these phenomena.

Emission spectrum narrowing provides strong evidence of ASE. This was observed by comparing the fluorescence spectrum (spontaneous emission) to the ASE spectra of the samples. The fluorescence signal was collected in the same manner as the ASE signal, from the sample edge by a multimode fiber, but while pumping with a white light source from the top. The normalized spectra of the fluorescence and ASE (the latter measured at  $I_p = 4.2 \text{ mJ/cm}^2$  for a stripe length of 0.635 mm) both obtained from sample B, are plotted in Fig. 3. The fluorescence spectrum is about  $6\times$  wider than the ASE spectrum.

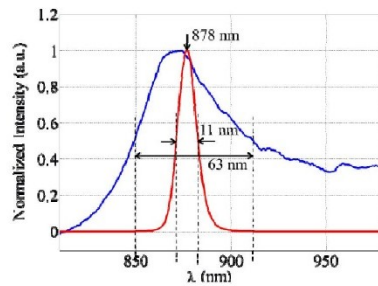


Fig. 3. Comparison of FWHM of fluorescence (blue) and ASE (red) spectra from Sample B.

Figure 4 plots the emission intensity of IR-140-doped PMMA waveguides at their peak emission wavelength as a function of pump intensity. The pump stripe length remains fixed at 0.635 mm.

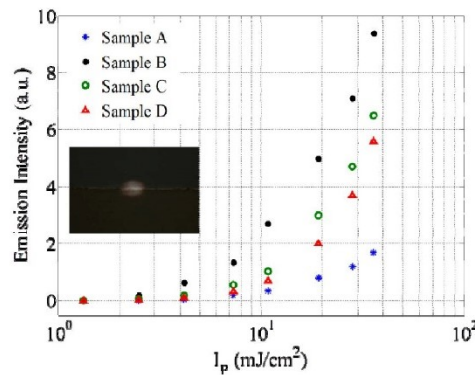


Fig. 4. Dependency of emission intensity on pump intensity at the peak emission wavelength for a fixed length of the pump stripe for samples A, B, C and D, inset: ASE intensity distribution at the output facet of sample B captured by CCD camera.

The emission strength grows drastically when the pump intensity exceeds the threshold which is slightly different for samples of different dye concentration. A distinct change of slope is observed at the threshold for each curve which is another signature of ASE. Above the threshold level, stimulated emission dominates over spontaneous emission and ASE in the polymeric waveguide is observed. The inset in Fig. 4 shows the emission intensity profile at the output facet of sample B captured by a CCD camera.

The small-signal gain coefficient of the IR-140-doped PMMA waveguides was measured using the variable stripe length (VSL) method. In this method the sample is pumped at fixed intensity, the pump stripe's length is varied, and the emission intensity (at the peak emission wavelength) is measured from the sample edge as a function of stripe's length.

In the linear operating region of the amplifier, the emission intensity ( $I_{ASE}$ ) is related to the stripe's length ( $l$ ) as follows:

$$I_{ASE}(l) = \frac{J_{SP}}{\gamma} [\exp(\gamma l) - 1] \quad (1)$$

where  $\gamma$  is the gain coefficient and  $J_{SP}$  is a constant proportional to the pump intensity that affects the excited state population and rate of the spontaneous emission [19].

The measured output intensity versus length was fitted to Eq. (1) using the nonlinear least squares (NLS) algorithm to extract the gain coefficient for the fabricated films while the excitation intensity ( $I_p$ ) was varied in the range from 5.8 mJ/cm<sup>2</sup> to 43.4 mJ/cm<sup>2</sup>. Results of the VLS measurements for samples A, B, C and D are plotted in Figs. 5(a)-5(d) respectively.

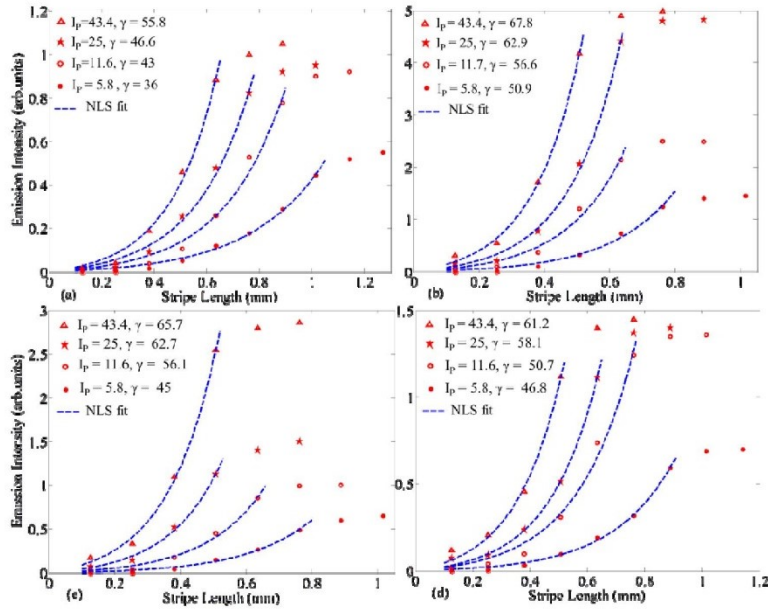


Fig. 5. Emission intensity as a function of pump length. Red markers represent the measured output intensities. The pump intensity ( $I_p$ ) was varied from 5.8 to 43.4 mJ/cm<sup>2</sup>. The gain coefficient ( $\gamma$ ) is obtained in cm<sup>-1</sup> by fitting the measured emission intensity to Eq. (1). Measurements are repeated for samples of different IR-140 concentration (a) Sample A, (b) Sample B, (c) Sample C, (d) Sample D.

The stripe's length was varied from 0.127 mm to about 1.2 mm in a step of 0.127 mm. The emission spectrum taken for each length was averaged over 5 s. At a rate of one pulse every 100 ms, 50 pump pulses illuminate the sample for each length. Measurements were performed on each sample for 8 lengths on average. Thus, an entire experiment took about 40 s for each sample corresponding to 400 pump pulses. No photo-bleaching was observed in the samples during this time interval.

As Fig. 4 shows, the emission intensity grows with increasing excitation length, eventually saturating. Increasing the pump intensity decreases the saturation length. Emission intensities in the saturation region, where the curves' slope start dropping, have been excluded from NLS fitting. The gain coefficient ( $\gamma$ ) is thus obtained in  $\text{cm}^{-1}$  under the small-signal regime of the amplifier. As the pump intensity increases, so does the gain coefficient. Increasing the pump intensity beyond  $43.4 \text{ mJ/cm}^2$  did not produce a higher emission intensity, so we limited the experiments to  $I_p = 43.4 \text{ mJ/cm}^2$ .

The maximum gain coefficient is  $\gamma \sim 68 \text{ cm}^{-1}$  at  $I_p = 43.4 \text{ mJ/cm}^2$  observed from sample B with 0.8wt % IR-140 to PMMA. Samples C, D and A are ranked from second to last in terms of gain coefficient. These results are consistent with the previous results of Fig. 2 and 3. Evidently, sample B is the best among those fabricated, which means that increasing the dye concentration leads to a larger gain coefficient up to a maximum, beyond which the gain coefficient begins to decrease.

Table 1 summarizes the gain coefficient ( $\gamma$ ) and spontaneous emission constant ( $J_{sp}$ ) versus  $I_p$  for samples A, B, C and D.

**Table 1. Gain Coefficient ( $\gamma$ ) and Spontaneous Emission Constant ( $J_{sp}$ ) Versus  $I_p$  for Samples A, B, C and D**

$I_p$ (mJ/cm <sup>2</sup> )	Sample A		Sample B		Sample C		Sample D	
	$\gamma$	$J_{sp}$	$\gamma$	$J_{sp}$	$\gamma$	$J_{sp}$	$\gamma$	$J_{sp}$
5.8	36.0	0.04	50.9	0.13	49.9	0.06	46.8	0.04
11.6	43.0	0.08	56.6	0.35	56.1	0.14	50.7	0.14
25	46.6	0.11	62.9	0.52	62.7	0.30	58.1	0.17
43.4	55.8	0.15	67.8	0.93	65.7	0.61	61.2	0.32

As mentioned earlier, an IR-140-doped PMMA film on glass operates as a leaky optical waveguide. Thus, the maximum achieved gain coefficient of  $\gamma \sim 68 \text{ cm}^{-1}$  corresponds to the modal gain of leaky TE and TM modes, and thus underestimates the material gain, although probably only slightly - modal modelling of the slab reveals that the fundamental TE and TM modes are strongly localised to the PMMA core. Nonetheless, numerical computations indicate that a material gain of  $68 \text{ cm}^{-1}$  is more than sufficient for active LRSPP plasmonics [9].

IR-140 had been previously used in a solution of ethylene glycol and dimethyl sulfoxide as the gain medium for an LRSPP amplifier [20]. The ASE gain coefficient of the LRSPP mode was reported as  $16.9 \text{ cm}^{-1}$ , using a dye concentration and pump intensity of  $3 \times 10^{17} \text{ cm}^{-3}$  and  $10 \text{ mJ/cm}^2$ , respectively. The material gain of this medium is deduced as  $47.8 \text{ cm}^{-1}$  through numerical modeling. Comparing the material gain of the IR-140 doped solution with that of the PMMA films indicates that the IR-140 concentration in polymer must be at least 10 times higher than in solution in order to provide the same material gain. In other words the gain coefficient in polymer is about 10 times lower than it is in a solution of the same dye concentration and under the same pump intensity. This may be due to the reduction of dye quantum efficiency in a solid-state medium where dye molecules interact with the host matrix. The triplet state of the dye molecules is also more easily accessible when the dye is embedded in a solid matrix, which increases the triplet loss and decreases the gain [21].

### 3. ASE polarisation

The absorption and emission processes in a dye-doped medium are modelled by elementary oscillating dipoles [21]. In such a medium if the pump signal is linearly polarized, the probability of excitation of dye molecules is proportional to  $\cos^2\theta_A$  where  $\theta_A$  is the angle between the electric field vector of the pump and the molecules' absorption transition moment [23]. Thus, illuminating dye molecules by a linearly polarized incident light, excites those molecules whose transition moments are oriented in a direction close to that of the electric field vector of the incident beam. Since the excitation mechanism is anisotropic, the emitted fluorescence will be also anisotropic.

As there is no phase relation between the light emitted by different molecules, the total fluorescence is considered as the superposition of three independent sources polarised along the  $x$ ,  $y$  and  $z$  directions (refer to Fig. 1(b) for the reference coordinate). Thus, the total intensity of the emitted light is [23]:

$$I = I_x + I_y + I_z \quad (2)$$

For a linearly polarized excitation, the direction of pump polarisation will set the axis of symmetry for the emitted fluorescence, according to the Curie principle. The emitted intensities perpendicular to the axis of symmetry are identical ( $I_{\perp 1} = I_{\perp 2} = I_{\perp}$ ). The emission anisotropy is then defined as [23]:

$$r = \frac{I_{\parallel} - I_{\perp}}{I_{\parallel} + 2I_{\perp}} \quad (3)$$

where  $I_{\parallel}$  and  $I_{\perp}$  are the emitted intensities in the directions parallel and perpendicular to the excitation polarisation respectively.

The ASE polarisation with respect to the pump polarisation in our IR-140-doped PMMA films was also investigated. Using the wave plate (WP) and polarizing beam splitter (PBS) in Fig. 1, the pump polarisation could be set as vertical or horizontal. If the pump is vertically (horizontally) polarized, it will be aligned parallel with (perpendicular to) the pump stripe after being reflected from the mirror ( $M_3$ ). The output emission was passed through an analyser in order to study the ASE gain of the orthogonal TE and TM modes. For this purpose an objective lens (20x) and another polarizer were added to the setup in Fig. 1 before the multimode fiber. The ASE gain coefficient was obtained for TE and TM modes separately under the cases in which the pump polarisation is aligned parallel or perpendicular to the pump stripe. Sample B with 0.8wt % IR-140 to PMMA, as the best performing sample, was used in this experiment.

Figures 6(a) and 6(b) show the gain measurement results using the VSL method for pump intensities of  $I_p = 22 \text{ mJ/cm}^2$  and  $I_p = 43.4 \text{ mJ/cm}^2$  respectively. This figure exhibits very interesting results. When the pump polarisation is aligned parallel to the pump stripe (dashed curves in Fig. 6), the emission intensity and the gain coefficient of TE and TM modes are almost equal. In other words the emitted fluorescence is unpolarised. This is because the main transverse electric field components of the TE and TM modes ( $E_x$  and  $E_y$ , respectively) are both perpendicular to the pump polarisation. Emission of the TM mode is slightly stronger, probably due to weak coupling to the  $E_z$  field component of this mode which is parallel to the pump polarisation. When the pump polarisation is perpendicular to the stripe, the emitted fluorescence is polarised mainly in TE mode. This result is also reasonable because the main electric field component of TE mode ( $E_x$ ) is aligned with the pump polarisation whereas both components of TM mode are perpendicular to the pump polarisation.

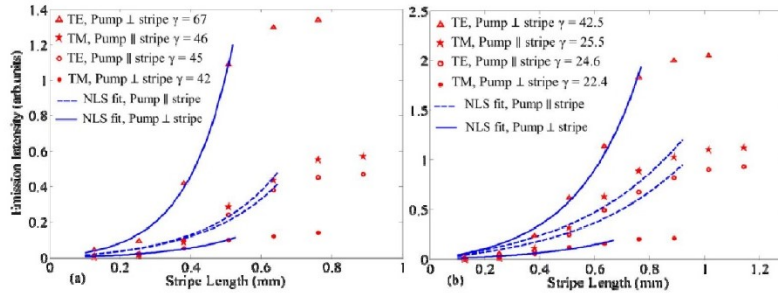


Fig. 6. ASE gain of the TE and TM modes. The pump polarisation is either parallel (||) or perpendicular ( $\perp$ ) to the pump stripe. (a)  $I_p = 22 \text{ mJ/cm}^2$ , (b)  $I_p = 43.4 \text{ mJ/cm}^2$

Comparing dash curves in Fig. 6(b) with corresponding curve in Fig. 5(b), when the pump polarisation is parallel to the stripe length, the level of emission intensity and also ASE gain coefficient have dropped by considerable amount. Adding the objective lens and polarizer before the multimode fiber in polarization study setup, introduces loss ( $\sim 3 \text{ dB}$ ) but the main reason could be the degradation of our samples in a 2 week time. The results of ASE polarisation experiment of IR-140-doped PMMA are consistent with previous experiment with this dye in solution [16].

A pump polarisation aligned parallel to the pump stripe is a good choice for plasmonic applications because more TM gain is available in this configuration (and surface plasmon waves are TM-polarised). Pumping from the top in the manner applied here is convenient - lateral or longitudinal pumping could potentially lead to more TM gain but the pump is not as easy to apply in these cases.

#### 4. Conclusion

ASE in the near-infrared from optically pumped IR-140-doped PMMA films was investigated. Thin films  $5 \mu\text{m}$  thick were deposited on standard microscope glass slides by spin-coating and curing a solution of PMMA, IR-140 and dichloromethane. Four dye concentrations were considered, corresponding to IR-140 to PMMA weight ratios of 0.4wt %, 0.8wt %, 1.2wt % and 1.6wt %. Linewidth narrowing with increasing pump intensity was observed in all films, which indicates ASE. ASE gain measurements using the variable stripe length method was performed on the samples of different dye concentration by increasing the pump intensity in an incremental manner. The ASE gain coefficient grows by increasing the dye concentration up to 0.8 wt % beyond which the gain coefficient starts decreasing. By increasing the pump intensity, the ASE gain coefficient increases up to pump intensities of  $I_p = 43.4 \text{ mJ/cm}^2$  beyond which it does not grow anymore. The maximum attained gain coefficient is  $\gamma \sim 68 \text{ cm}^{-1}$  for the sample of 0.8wt % at  $I_p = 43.4 \text{ mJ/cm}^2$ . This gain is sufficient for certain active plasmonics applications particularly involving LRSPPs. ASE polarisation was also investigated as a function of pump polarisation relative to the pump stripe. The ASE is unpolarised when the pump polarisation is parallel to the pump stripe whereas it is more TE polarized when the pump polarisation is perpendicular to the pump stripe.

## 4. Surface plasmon DFB laser: design optimization, fabrication and test

### 4.1 Summary

A distributed feedback (DFB) laser using stepped-in-width Ag stripe in a uniform long-range surface plasmon polariton structure was proposed in chapter 2. In this chapter realization of the DFB laser at  $\lambda_0 = 882$  nm is presented, using both Ag and Au metal stripes and in a non-uniform LRSPP structure. The non-uniform LRSPP structure refers to the index mismatch between the top cladding gain media, IR-140 doped PMMA, and the bottom cladding  $\text{SiO}_2$  at  $\lambda_0 = 882$  nm. The non-uniform cladding prevents the  $ss_b^0$  mode from being excited unless the top cladding's thickness is reduced sufficiently, as was explained in section 1.2. The DFB laser design is optimized to remove any TM polarized slab mode emission in the IR-140 doped PMMA top cladding, and simultaneously maximize the LRSPP mode power gain in the structure. Using coupled-mode theory the minimum and maximum DFB length is determined for single mode lasing. DFB lasers were fabricated and tested. The fabrication processes, experimental setup, and results are fully described in this chapter. Electron beam lithography is used to create stepped-in-width Ag/Au DFBs with a spatial period of  $\Lambda \sim 303$  nm. It will be seen that Au DFBs are produced with better quality, with less roughness and well defined corners compared to Ag DFBs. However; both Ag and Au DFBs exhibit single, narrow emission peaks at around  $\lambda_0 = 882$  nm. The light-light plots show a clear lasing threshold of  $\sim 7.8$  mJ/cm<sup>2</sup> and  $\sim 10.4$  mJ/cm<sup>2</sup> for Ag and Au DFBs, respectively.

### 4.2 Contribution

I modeled, designed and optimized the DFB structures. I produced IR-140 doped PMMA with 0.9wt% dye concentration and through an ASE characterization I obtained the extinction coefficient of this material. The real index of IR-140 doped PMMA was measured accurately

using ellipsometry by Choloong Hahn, the post-doctoral fellow in the Berini's group. I fabricated and tested the DFB samples. Anthony Olivieri and Dr. Berini provided very helpful fabrication hints. Choloong Hahn and Maude Amyot-Bourgeois also offered very useful suggestion for experimental setup. I wrote the DFB laser's manuscript. Dr. Tait and Dr. Berini contributed to the interpretation of the results and revised the manuscript.

### **4.3 Article**

The manuscript presented in this section is going to be submitted for publications.

# Surface Plasmon Single-Mode Distributed Feedback Lasers

Elham Karami Keshmarzi, R. Niall Tait

*Dept. of Electronics, Carleton University, 1125 Colonel By Dr., Ottawa, ON, Canada*

Pierre Berini

*School of Electrical Engineering and Computer Science, University of Ottawa, 800 King Edward Ave. Ottawa, ON, Canada,*

*Department of Physics, University of Ottawa, Centre for Research in Photonics, University of Ottawa*

Single-mode distributed feedback lasers are realized in the near infrared as a two-dimensional, non-uniform long-range surface plasmon polariton structure supporting a transverse magnetic polarized surface wave. The surface plasmon structure consists of a 20 nm-thick, 1  $\mu\text{m}$ -wide metal stripe (Ag or Au) on a silica substrate, where the stripe is stepped in width periodically, forming a 1<sup>st</sup> order Bragg grating. Optical gain is provided by optically pumping a 450 nm-thick IR-140 doped PMMA layer as the top cladding, which covers the entire length of the Bragg grating, thus creating a distributed feedback laser. The design, fabrication and experimental results are presented. These lasers are suitable as a highly coherent single-mode source of surface plasmons, or for integration with other surface plasmon elements of similar structure.

## I. INTRODUCTION

Surface plasmon-polaritons (SPPs) are transverse magnetic (TM) polarized surface waves propagating along a metal-dielectric interface and their fields are coupled to the electron plasma oscillations in the metal<sup>1</sup>. SPPs exhibit unique properties including strong field enhancement, subwavelength confinement and high sensitivity to the bounding dielectric environment. However, SPP excitations are highly dissipative which constrains their applications. Significant theoretical and experimental work has been conducted over the past decade to compensate for SPP loss or even produce amplification and lasing with surface plasmons<sup>2</sup>. Indeed, lasing with surface plasmons is of strong current interest because the structures can be miniaturised, potentially offering compact coherent sources for photonic integrated circuits. Surface plasmon lasers involving the interaction of an amplifying medium with plasmonic nano-particles were proposed<sup>3,4</sup> and demonstrated<sup>5</sup> as nano-scale, ultra-fast and low-threshold surface plasmon sources, referred to as spasers. Array of nano-particles for improved spaser quality has been investigated. Coherent and directional band-edge lasing in two-dimensional plasmonic lattices were reported using IR-140 doped polyurethane gain media.<sup>6,7</sup> Spasers based on hybrid dielectric-metal structures involving a high-gain nano-scale dielectric waveguide separated from a metal substrate by a very thin gap were also proposed and demonstrated.<sup>8-14</sup> It was shown that in close proximity to a metal film, the spontaneous emission rate in these structures is significantly enhanced and the lasing threshold is reduced. Lasing with surface plasmons in single-interface metal-semiconductor structures was reported at far infrared wavelengths, where the metal was used as a way to increase the mode confinement and overlap with the gain medium, while simultaneously reducing the total layer thickness of the structure.<sup>15,16</sup> There are also reports of surface plasmon lasing in symmetric metal-dielectric-metal<sup>17</sup> and dielectric-metal-dielectric<sup>18</sup> structures forming Fabry-Perot cavity

resonators. Moreover, the use of distributed feedback (DFB) to enable surface plasmon lasing was proposed in metal-insulator-metal<sup>19</sup>, dielectric-loaded SPPs<sup>20</sup>, single metal-dielectric interface SPPs<sup>21</sup>, and in long-range surface plasmon polariton (LRSP) structures, where low noise performance is expected due to the low spontaneous emission into the LRSP lasing mode<sup>23</sup>.

In this paper we report the realization of optically-pumped surface plasmon DFB lasers based on a step-in-width metal stripe grating, operating at room temperature in the near infrared. The metal stripe is embedded in non-uniform dielectric media and confined SPP propagation is achieved by using a thin upper cladding similar to the SPP amplifier discussed in Ref. [24]. Optical gain is provided by laser dye molecules in a dielectric host (a polymer film); the same molecules were used in a liquid solvent in previous work on SPP amplification<sup>25</sup>. This laser configuration is interesting because it can emit a single lasing mode with high coherence. Single mode lasing peaks of very narrow linewidth are demonstrated using Ag and Au DFBs at  $\sim 882$  nm. Kinks in the light-light curves are observed at threshold pump energy densities of  $\sim 7.8$  and  $\sim 10.4$  mJ/cm<sup>2</sup> for Ag and Au DFBs respectively. The lasing emission is exclusively TM polarized.

The organization of this paper is as follows. In section II the theory related to the design and modeling of the lasers is presented. Section III describes the fabrication details and the experimental results. Finally, conclusions are drawn in Section IV.

## II. THEORETICAL

### A. Laser Architecture

A 3D sketch of the laser architecture is shown in Fig. 1. A 20 nm-thick, 1  $\mu\text{m}$ -wide metal stripe (Ag or Au), is formed on a 15  $\mu\text{m}$ -thick SiO<sub>2</sub> substrate. The metal stripe is periodically stepped in width from 1 to 0.5  $\mu\text{m}$  in a pitch of  $\Lambda \sim 303$  nm and duty cycle of  $\sim 50\%$ , forming a

1<sup>st</sup> order Bragg grating with a Bragg wavelength of  $\lambda_B \sim 882$  nm.

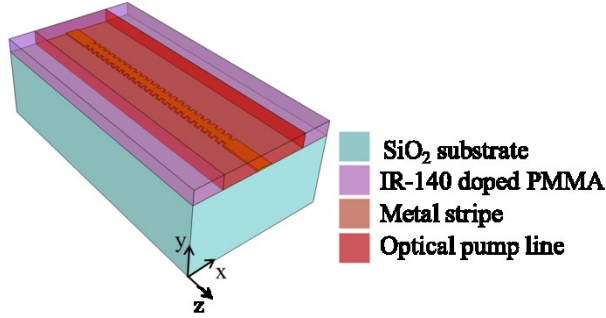


Fig. 1 Sketch of a plasmonic DFB laser comprising a step-in-width metal stripe Bragg grating on a SiO<sub>2</sub> substrate and covered with a layer of IR-140 doped PMMA as the optical gain medium. The structure is pumped optically from the top by a  $\sim 400$   $\mu\text{m}$ -wide pump line as shown.

The structure is covered with a thin film of IR-140 doped PMMA as the laser active medium. This gain medium provides  $\sim 81$  cm<sup>-1</sup> of material gain at a peak wavelength of  $\sim 880$  nm<sup>26</sup>. The gain medium is pumped optically from the top by a 400  $\mu\text{m}$ -wide pump line of length equal to that of the step-in-width metal grating. The grating is terminated at each end by uniform metal stripes about 200  $\mu\text{m}$  long, reaching to the end facets of the device. All dimensions are selected such that the fundamental LRSPP (the  $ss_b^0$  mode<sup>27</sup>) propagates as the only long-range mode in the structure.

### B. Laser Design

Our DFB lasers operating with LRSPPs are designed using the theory of coupled modes in a Bragg grating with a periodic perturbation of the refractive index<sup>28</sup>. In this theory, a complex coupling coefficient is defined which is proportional to the modulation of real (index) and imaginary (gain) refractive index in the periodic structure. The coupling coefficient measures the strength of coupling between the forward and backward propagating modes in a DFB configuration, and as it increases, stronger feedback is provided for lasing which decreases the lasing threshold.

In our modeling approach, we use an equivalent dielectric stack where each dielectric layer represents a section of metal stripe waveguide of width  $w_i$  ( $i = 1, 2$ ;  $w_1 = 1$   $\mu\text{m}$ ,  $w_2 = 0.5$   $\mu\text{m}$ ). Specifically, the refractive index of a dielectric layer in the stack is taken as the complex effective index,  $n_{effi}$  ( $i = 1, 2$ ), of the LRSPP mode propagating in a corresponding waveguide section, and the thickness of the dielectric layer is taken equal to the corresponding length of waveguide<sup>22</sup>. Mode analysis using a numerical solver (COMSOL Multiphysics v5.2) is performed to calculate the LRSPP mode's effective index on the metal stripes. For modal analysis, the refractive indices of the materials used (Fig. 1) were taken from Ref. [29] at our wavelength of interest,  $\lambda_0 = 882$  nm, which corresponds to the peak emission

wavelength of IR-140 molecules in PMMA<sup>30</sup>. However, the refractive index of our gain medium (IR-140:PMMA) was found experimentally. As discussed in Section III, our gain medium consists of PMMA doped with  $\sim 0.9$  %wt IR-140. This dopant alters the refractive index of PMMA, which we have found to be  $n = 1.5$  using ellipsometry and  $k = +5.5 \times 10^{-4}$  deduced by measuring the amplified spontaneous emission (ASE) response<sup>30</sup> using the variable stripe length (VSL) method<sup>31</sup>.

The refractive index of IR-140 doped PMMA, as stated above, does not match the refractive index of the SiO<sub>2</sub> lower cladding at  $\lambda_0 = 882$  nm. The LRSPP mode is unguided for optically-thick doped PMMA with SiO<sub>2</sub> as the lower cladding due to index mismatch. The solution to this problem is to lower the thickness of the dye-doped PMMA sufficiently so that in combination with air (above) an effective index match to that of SiO<sub>2</sub> can be achieved.

The finite thickness of the IR-140 doped PMMA layer creates a slab waveguide on both sides of the metal stripe which can support transverse electric (TE) and transverse magnetic (TM) slab modes. It is desired to cut-off these slab modes because they can collect strong ASE under pumping. Fig. 2 shows the computed effective index of the TE<sub>0</sub> and TM<sub>0</sub> slab modes along with that of the LRSPP mode on 20 nm-thick, 1  $\mu\text{m}$ -wide metal stripes formed of Au and Ag, vs. the thickness of the doped PMMA layer. The refractive index of fused silica (FS) is also plotted and used to identify the cut-off points of the modes. The modes become radiative into the silica lower cladding when their effective index drops below the refractive index of fused silica.

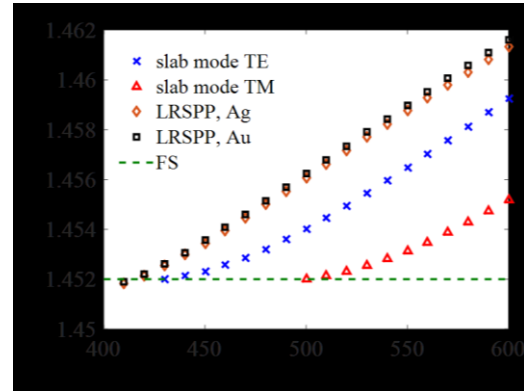


Fig. 2 Effective index of TE<sub>0</sub> and TM<sub>0</sub> slab modes along with that of the LRSPP mode supported in a 20 nm-thick, 1  $\mu\text{m}$ -wide Au or Ag stripe. The index of fused silica (FS) defines the mode cut-off points.

According to Fig. 2, the TE<sub>0</sub> and TM<sub>0</sub> modes are cut-off for PMMA thicknesses below 430 and 500 nm respectively, whereas the cut-off thickness for the LRSPP mode for Au or Ag stripes is about 410 nm. Since the LRSPP is a TM mode, we can simply filter the TE<sub>0</sub> slab mode using a polarizer at the output facet of the structure. The cut-off thickness to consider is that of the TM<sub>0</sub> mode (500 nm), so the thickness of the doped

PMMA layer should be selected within the range from 410 to 500 nm.

In this range of thickness there is an optimum where the LRSPP mode power gain (MPG) is maximised. Fig. 3 plots the computed MPG of the LRSPP mode for Au and Ag stripes, with the red and black dashed lines bounding the design range. The MPG must be positive, so for the case of Au stripes the thickness of the doped PMMA is limited to  $t_{PMMA} < 470$  nm. For Ag stripes, the upper range is determined by the  $TM_0$  cut off thickness,  $t_{PMMA} < 500$  nm. The smallest thickness of the doped PMMA layer for both Ag and Au stripes is limited to 410 nm in order for the LRSPP to remain guided. The maximum MPG for Au and Ag stripes occurs at  $t_{PMMA} \sim 450$  nm, as observed in Fig. 3.

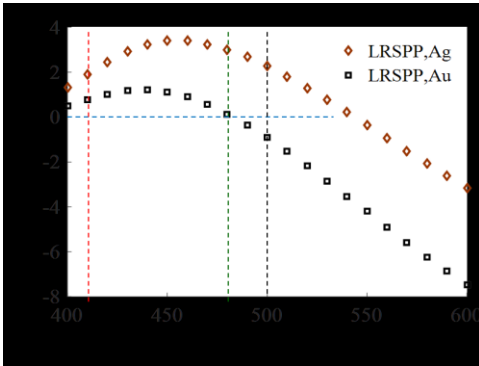


Fig. 3 MPG in  $\text{cm}^{-1}$  of the LRSPP mode on Au and Ag stripes vs. the thickness of the doped PMMA layer. The red and black dashed lines identify the design range based on mode cut-off. The green dashed line identifies the transparency thickness (MPG = 0) for the case of the Au stripe.

We proceed with DFB design using a doped PMMA thickness of  $t_{PMMA} = 450$  nm. The distribution of the main transverse electric field component ( $E_y$ ) of the LRSPP mode, computed at  $\lambda_0 = 882$  nm for Ag stripe widths of  $w_1 = 1 \mu\text{m}$  and  $w_2 = 0.5 \mu\text{m}$ , is shown in Figs. 4(a) and (b), respectively. The use of the equivalent dielectric stack model is justified by considering that the LRSPP modes in Figs. 4(a) and (b) resemble a  $y$ -polarised plane wave propagating longitudinally along the metal stripe. Most of the fields in the LRSPP are located in the background dielectric<sup>27</sup>. The LRSPP mode size in Fig. 4 (a) is about  $4 \mu\text{m}$  and it can be shown that it can couple to Gaussian beams and single mode fibers at  $\lambda_0$  with coupling efficiency around 0.95%<sup>32</sup>.

The average real effective refractive index for the Au and Ag step-in-width gratings is found to be  $n_{ave} = (n_{eff1} + n_{eff2})/2 = 1.4528$ , similar for Au and Ag stripes. The pitch of the first order Bragg grating used in our DFB lasers is then computed  $\Lambda = \lambda_0/2n_{ave} = 303$  nm. Using the coupled-mode formulation in Ref. [28], the coupling coefficients for DFB lasers based on our stepped-in-width Au and Ag gratings are found as  $\kappa_{Au} = 36 \text{ cm}^{-1}$  and  $\kappa_{Ag} = 34 \text{ cm}^{-1}$ . The mode gain coefficient on the Au and Ag gratings are  $\alpha_{Au} = 1.2 \text{ cm}^{-1}$  and  $\alpha_{Ag} = 1.8 \text{ cm}^{-1}$ , respectively (averaged over the two stripe widths used

within a unit cell). Fig. 8 in Ref. [28] was used to find the minimum and maximum grating lengths for single (longitudinal) mode lasing:  $L_{min-Ag} = 2.7$  mm,  $L_{max-Ag} = 6.1$  mm for Ag DFBs, and  $L_{min-Au} = 4.2$  mm,  $L_{max-Au} = 9.2$  mm for Au DFBs.

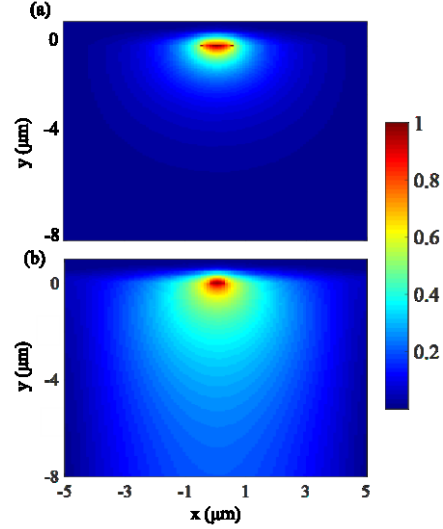


Fig. 4 Computed distribution of the main transverse electric field component ( $E_y$ ) of the LRSPP mode on 20 nm-thick, (a)  $1 \mu\text{m}$ -wide, and (b)  $0.5 \mu\text{m}$ -wide Ag stripes on  $\text{SiO}_2$ , covered with a 450 nm-thick doped PMMA layer.

### III. EXPERIMENTAL

#### A. Device Fabrication

DFB lasers as described in Section II were fabricated in a standard clean room. Four inch Si wafers bearing a  $15 \mu\text{m}$ -thick thermally grown  $\text{SiO}_2$  layer were cleaved into  $2 \text{ cm} \times 2 \text{ cm}$  samples and cleaned thoroughly in Acetone, Isopropanol, and DI water baths. After dehydration on a hot plate, two layers of PMMA (Mw: 950K / Mw: 495K) were spun on the sample, baked, and used as the positive resist for electron beam lithography (two molecular weights are used to produce a re-entrant profile). Layouts of 1<sup>st</sup> order stepped-in-width gratings of three pitches (293, 303 and 313 nm) were prepared for electron beam lithography. An equal spacing of  $400 \mu\text{m}$  was introduced between adjacent DFBs. The Ag and Au step-in-width gratings comprised  $N_{Ag} = 9,000$  and  $N_{Au} = 15,000$  unit cells, resulting in  $\sim 3.0$  mm-long and  $\sim 4.8$  mm-long Ag and Au DFBs, respectively. Immediately before electron beam lithography, a thin layer of conducting polymer (E-Spacer) was spun on the PMMA bilayer on the sample to avoid charging during electron beam exposure. The sample was patterned by electron beam, then developed in a solution of MIBK:IPA at  $20 \text{ }^\circ\text{C}$  for 2 min, resulting in the creation of step-in-width grating patterns. A 20 nm thick Au or Ag film was then deposited via thermal (for Au) and electron beam (for Ag) evaporation. Immediate and gentle lift-off in an Acetone bath is then carried out to produce the metal grating pattern on the sample. Next a solution of 5 %wt PMMA in dichloroethane with 0.9

%wt IR-140 is spun and backed on the sample producing a 450 nm-thick doped PMMA film on top of the metal gratings. Finally, the sample is cleaved, producing optical quality facets. Fig. 5 summarizes the fabrication process as described.



Fig. 5 Fabrication process for realizing LRSP DFB lasers. (a) Bi-layer PMMA electron beam resist is spun and backed; (b) E-Spacer is spun; (c) electron beam lithography and development is performed; (d) metal deposition using electron beam evaporation; (e) Immediate lift-off in an Acetone bath; (f) Spin coating and backing of a 450 nm-thick doper PMMA layer.

The thickness of Ag and Au gratings were determined by atomic force microscopy (AFM) prior to coating with the doped PMMA layer, and found to be  $t_{Ag} = 21$  nm and  $t_{Au} = 22.5$  nm. Thickness of the doped PMMA film on Ag and Au dies was measured using a Dektak profilometer, and found to be  $470 \pm 15$  nm in both cases. Fig. 6(a) gives an atomic force microscope image for a Au grating, and Figs. 6(b) and 6(c) give scanning electron microscope images for Au and Ag gratings, post lift-off (step (e) in Fig. 5).

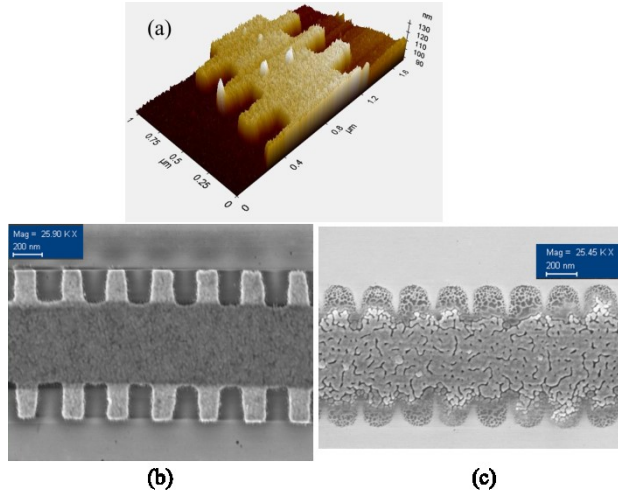


Fig. 6 (a) Atomic force microscope image of a 20 nm-thick thermal evaporated Au stepped-in-width grating; (b) Scanning electron microscope image of a Au grating; (c) Scanning electron microscope image of a Ag grating.

It should be noted that the same fabrication process is used for Ag and Au DFBs, however, as seen in Fig. 6(c), the Ag grating does not look as good as the Au grating. We surmise that this is due to Ag de-wetting from the

SiO<sub>2</sub> surface, causing Ag to ball up on the sample rather than wetting and adhering properly. Moreover, larger grains and a higher roughness are observed. Optimisation of the deposition conditions and the inclusion of a thin adhesion layer would improve the outcome.

### B. Setup

All experiments are carried out at room temperature. The experimental setup is illustrated in Fig. 7.

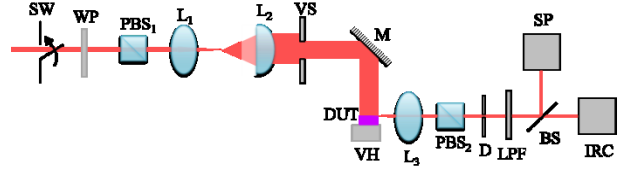


Fig. 7 Experimental setup for characterizing DBB lasers. SW: electro-mechanical switch for pump blocking; WP:  $\lambda/2$  waveplate; PBS<sub>1</sub> and PBS<sub>2</sub>: Polarizing beam splitters; L<sub>1</sub>: spherical lens; L<sub>2</sub>: Cylindrical lens; VS: variable slit; M: Mirror; DUT: Die under test; VH: Vacuum holder; L<sub>3</sub>: 20× objective; D: Diaphragm; LPF: 850 nm long-pass filter; BS: beam splitter; IRC: Infrared camera; SP: Spectrograph.

The second harmonic from a Nd:YAG pulsed laser (Spectra Physics, Mod. Quanta-Ray Lab 190) pumps a tunable dye laser (Sirah, Mod. Cobra-Stretch) to produce 8 nsec pulses in a 10 Hz repetition rate at the peak absorption wavelength of IR-140,  $\lambda_p = 810$  nm.<sup>30</sup> An electro-mechanical switch (SW) is used to block the pump beam as needed. A  $\lambda/2$  waveplate (WP) and a polarizing beam splitter (PBS<sub>1</sub>) are used to control the pump intensity and polarization. A biconvex spherical lens (L<sub>1</sub>) is used to magnify the beam spot, which is then followed by a cylindrical lens (L<sub>2</sub>) to convert the Gaussian beam into a pump line about 400  $\mu$ m wide. A variable slit is used to control the pump line length and match it to the length of the die under test (DUT). A mirror is used to reflect the pump line onto the DUT which is held tightly by a vacuum holder (VH) mounted on a micro-stage positioner. Using a microscope camera, the pump line is aligned parallel to and centered on a DFB on the die, such that only a single DFB is excited. The spacing between adjacent DFBs on the die is 400  $\mu$ m (similar to the width of the pump line), so that no two DFBs can be excited simultaneously. The output emission from the DFB under test is collected by a 20× objective (L<sub>3</sub>) and passed through a polarizing beam splitter (PBS<sub>2</sub>) to remove any TE polarized spontaneous emission. An optical diaphragm (D) is used reduce the TM polarized spontaneous emission that may be carried by the slab on either side of the DFB, and a long pass filter (LPF) which cuts wavelengths below 850 nm is used to block the pump signal. A glass slide is used as a beam splitter (BS) to split the DFB's output between an infrared camera (IRC) and a spectrograph (SP). The infrared camera (MIcronViewer, Mod. 7290A) captures images of the emitted mode. The spectrograph (Princeton Instruments, Mod. IsoPlane SCT-320) is a high resolution diffraction system attached to an ultrafast gated ICCD camera (Princeton Instruments, Mod. PI-

MAX4), and is synchronized with the pump pulses, enabling time-resolved characterization. The pump polarization is set to be parallel with the pump line and the DFBs to maximize optical TM gain, as explained in Ref. [30]. Also, the energy density of the pump varies from 1 mJ/cm<sup>2</sup> to a maximum 47 mJ/cm<sup>2</sup> in the experiments.

### C. Results

In terms of design parameters, we expect Ag and Au DFBs to have similar lasing performance (*i.e.* lasing threshold, and linewidth). This is because the coupling and mode gain coefficients, as presented in section II, are very similar for Ag and Au DFBs.

About 20 DFBs on different fabricated dies were tested. Typical responses for Ag and Au DFBs are presented in this section. Fig. 8 plots output emission spectra from a Ag and a Au DFB tested with a pump energy density of  $I_p = 15$  mJ/cm<sup>2</sup>, showing narrow peaks at 882 nm and 881.6 nm respectively. The insets in Figs. 8(a) and (b) zoom into the narrow peaks. The linewidth of these emission peaks are 0.2 nm (Fig. 8(a)), and 0.35 nm (Fig. 8(b)), clearly limited by the resolution of the spectrograph used in the experiments - the actual linewidths are narrower. Even though spectrograph-limited, these linewidths place a ceiling of 0.2 nm on the linewidth of our lasers, and this ceiling corresponds (to our knowledge) to the narrowest peaks reported to date in the literature for surface plasmon lasers.

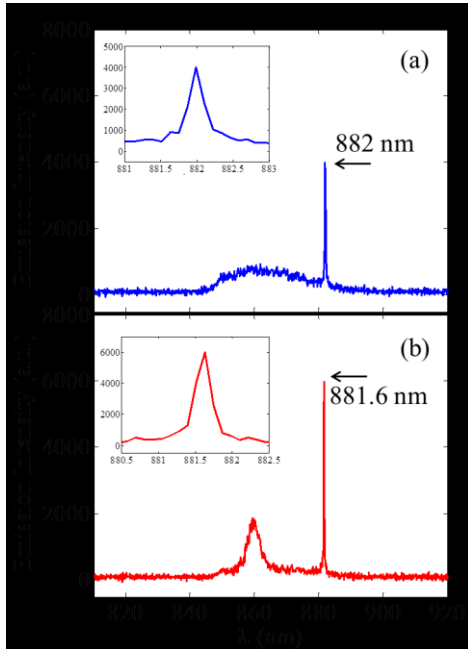


Fig. 8 Lasing emission spectra from: (a) Ag DFB and (b) Au DFB lasers pumped with an energy density of  $I_p \sim 10$  mJ/cm<sup>2</sup>. Insets: zoomed peaks.

As can be observed, weak broadband spontaneous emission is present in Fig. 8(a), and some ASE ( $\sim 7$  nm linewidth) is evident in Fig. 8(b), both near 860 nm,

which corresponds to the location of maximum gain in the doped PMMA. It is noteworthy that the lasing peak in Fig. 8(b) is much narrower than the ASE peak. The linewidths observed are narrower than the narrowest linewidths reported to date for SPP lasers, such as FWHM = 0.5 nm, obtained at cryogenic temperatures for a Ag laser in an electrically pumped metal-insulator-semiconductor-insulator-metal structure at telecommunication wavelength<sup>19</sup>, or FWHM = 0.4 nm, reported for a surface-plasmon enhanced DFB laser at  $\sim 615$  nm in a Ag-polymer single-interface structure.<sup>21</sup>

L-L graphs are generated by plotting the output emission intensity at the lasing peak vs. the pump energy density, as shown in Fig. 9. The clear kinks in these plots indicate the onset of lasing. The insets to these figures illustrate sudden emission narrowing at the onset of lasing. The L-L characteristic of each DFB laser in the linear region before saturation is fitted to a linear model, as shown by the red dashed lines in Fig. 9. The intercept of these lines with the emission floor gives the lasing thresholds for the Ag and Au DFBs as 7.8 mJ/cm<sup>2</sup> and 10.4 mJ/cm<sup>2</sup> respectively which is a moderate pump energy density.

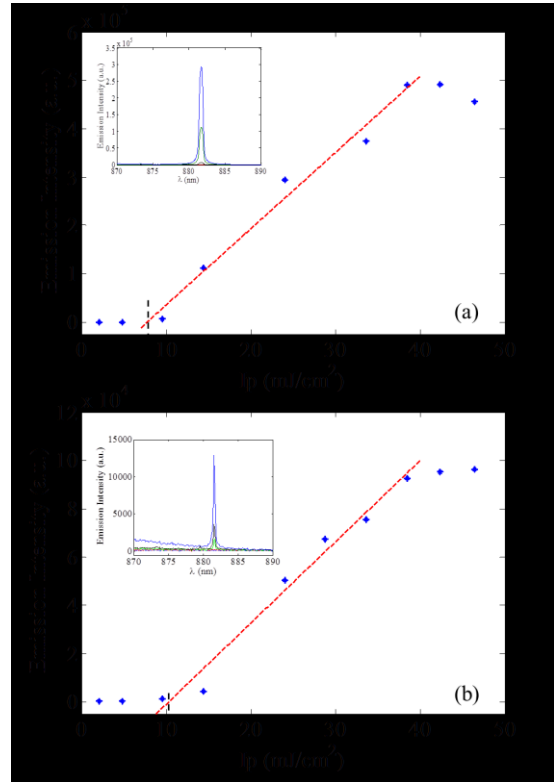


Fig. 9 Peak emission intensity vs. pump energy density for (a) Ag and (b) Au DFBs. The lasing threshold for the Ag DFB is 7.8 mJ/cm<sup>2</sup> and for the Au DFB is 10.4 mJ/cm<sup>2</sup>. Insets: linewidth narrowing with increasing pump energy density.

The lasing threshold was lower in most tested Ag DFBs compared to Au DFBs. This is due to the lower absorption of Ag compared to Au, as was similarly observed in two-dimensional band-edge nano-particle

lattice lasers<sup>7</sup>. Also, the DFB lasing threshold is higher than the ASE threshold ( $\sim 1 \text{ mJ/cm}^2$ ) in IR-140 doped PMMA slab waveguides, in part because of the lower propagation loss in the latter and the cavity leakage loss in the former (to create an emitted signal).<sup>26</sup> Also, the pump intensity for our DFB lasers is comparable with the pump intensity used for amplification of LRSPPs with IR-140 in solution (a solvent mixture).<sup>25</sup> However, the threshold is about  $20\times$  larger than the threshold ( $0.5 \text{ mJ/cm}^2$ ) of strongly coupled plasmonic nano-particle arrays using IR-140 doped polyurethane<sup>7</sup>.

Fig. 10 gives a mode image of the output from a Ag DFB captured by the infrared camera. A bright spot is observed, against a dim background corresponding to TM-polarized spontaneous emission propagating in the slabs adjacent to the Ag DFB, as slab modes that are radiative into the  $\text{SiO}_2$  lower cladding. The bright spot corresponds to the emission of the LRSPP lasing mode in the Ag DFB (*cf.* Fig. 3). The mode appears strongly guided and robust.



Fig. 10 Output mode from a Ag DFB captured by the infrared camera, showing a robustly-guided and bright lasing mode.

These results show that Ag and Au DFB lasers can generate highly coherent LRSPPs with good modal confinement, at near infrared wavelengths and lab temperature, using moderate pump energy densities.

Although LRSPP lasers offer less confinement than hybrid plasmonic nano-lasers,<sup>8-12</sup> the former produce narrower linewidths (compared to a few nanometers for the latter, as deduced from emission spectra). Also the optical pump intensity used in the latter is usually very high, *e.g.*, above  $100 \text{ MW/cm}^2$ ,<sup>8</sup> or are operated at cryogenic temperatures.<sup>9</sup> A FWHM of 0.7 nm was reported in a subwavelength confined, waveguide embedded (WEB) plasmon laser at visible wavelengths,<sup>9,10</sup> but with using a very strong pump intensity above  $3 \text{ GW/cm}^2$ .

#### IV. CONCLUSION

Single-mode, optically-pumped DFB lasers operating at room temperature with LRSPPs, based on step-in-width Ag and Au grating stripes, in a non-uniform dielectric structure involving a dye-doped polymer as the gain medium, are designed, modelled, realized and demonstrated. Details of the modeling and design, along with the fabrication processes applied and the experimental procedures developed are provided. DFB LRSPP lasing was achieved at the design wavelength of 882 nm, and linewidths of 0.2 and 0.35 nm were

observed for Ag and Au DFBs, respectively, which are the narrowest linewidths observed to date for SPP lasers. The TM-polarized emission and high-quality lasing mode, along with their ease of fabrication, make these DFB lasers interesting as high-coherence sources of surface plasmons for integration with passive elements.

#### References

- [1] H. Raether, "Surface plasmons on smooth and rough surfaces and on gratings", (Springer, 1988).
- [2] P. Berini, and I. De Leon, "Surface plasmon-polariton amplifiers and lasers", *Nature Photonics* 6, 16–24 (2012).
- [3] D. J. Bergman, and M. I. Stockman, "Surface Plasmon amplification by stimulated emission of radiation: Quantum generation of coherent surface plasmons in nanosystems," *Phys. Rev. Lett.* 90, 027402 (2003).
- [4] M. I. Stockman, "The spaser as a nanoscale quantum generator and ultrafast amplifier", *J. Opt.* 12, 024004 (2010).
- [5] M. A. Noginov, G. Zhu, A.M. Belgrave, R. Bakker, V.M. Shalaev, E.E. Narimanov, S. Stout, E. Herz, T. Suteewong and U. Wiesner, "Demonstration of a spaser-based nanolaser," *Nature*, vol. 460, 1110, (2009).
- [6] J. Y. Suh, C. H. Kim, W. Zhou, M. D. Huntington, D. T. Co, M. R. Wasielewski, and T. W. Odom, "Plasmonic bowtie nanolaser arrays", *Nano Lett.* 12, 5769-5774, (2012).
- [7] W. Zhou, M. Dridi, J. Y. Suh, C. H. Kim, D. T. Co, M. R. Wasielewski, G. Schatz, and T. W. Odom, "Lasing action in strongly coupled plasmonic nanocavity arrays", *Nat. Nanotechnol.* 8, 506-511, (2013).
- [8] R. F. Oulton, V. J. Sorger, T. Zentgraf, R. M. Ma, C. Gladden, L. Dai, G. Bartal, and X. Zhang, "Plasmon lasers at deep subwavelength scale", *Nature* 461, 629-632 (2009).
- [9] R. M. Ma, R. F. Oulton, V. J. Sorger, G. Bartal, G., and X. Zhang, "Room-temperature subdiffraction-limited plasmon laser by total internal reflection", *Nat. Mater.* 10, 110-113 (2011).
- [10] R. M. Ma, X. Yin, R. F. Oulton, V. J. Sorger, and X. Zhang, "Multiplexed and electrically modulated plasmon laser circuit", *Nano Lett.* 12, 5396-5402 (2012).
- [11] Y. J. Lu, J. Kim, H. Y. Chen, C. Wu, N. Dabidian, C. E. Sanders, C. Y. Wang, M. Y. Lu, B. H. Li, X. Qiu, W. H. Chang, L. J. Chen, G. Shvets, C. K. Shih, and S. Gwo, "Plasmonic nanolaser using epitaxially grown silver film", *Science* 337, 450-453 (2012).

- [12] T. P. H. Sidiropoulos, R. Röder, S. Geburt, O. Hess, S. A. Maier, C. Ronning, and R. F. Oulton, “Ultrafast plasmonic nanowire lasers near the surface plasmon frequency”, *Nat. Phys.* 10, 870-876, (2014).
- [13] Y. Li, and W. P. Huang, “Electrically-pumped plasmonic lasers based on low-loss hybrid SPP waveguide”, *Opt. Exp.* 23, 24843-24849, (2015).
- [14] E. Bermudez-Uren, G. Tutuncuoglu, J. Cuerda, C. L. C. Smith, J. Bravo-Abad, S. I. Bozhevolnyi, A. Fontcuberta i Morral, F. J. García-Vidal, and R. Quidant, “Plasmonic Waveguide-Integrated Nanowire Laser”, *Nano Lett.* 17, 747-754, (2017).
- [15] C. Sirtori, C. Gmachl, F. Capasso, J. Faist, D. L. Sivco, A. L. Hutchinson, and A. Y. Cho, “Long-wavelength ( $\lambda \approx 11.5 \mu\text{m}$ ) semiconductor lasers with waveguides based on surface plasmons”, *Opt. Lett.* 23, 1366-1368, (1998).
- [16] A. Tredicucci, C. Gmachl, F. Capasso, A. L. Hutchinson, D. L. Sivco, and A. Y. Cho, “Single-mode surface-plasmon laser”, *Appl. Phys. Lett.* 76, 2164-2166, (2000).
- [17] M. T. Hill, M. Marell, E. S. P. Leong, B. Smalbrugge, Y. Zhu, M. Sun, P. J. vanVeldhoven, E. J. Geluk, F. Karouta, Y. S. Oei, R. Nötzel, C. Z. Ning, and M. K. Smit, “Lasing in metal-insulator-metal sub-wavelength plasmonic waveguides”, *Opt. Exp.* 17, 11107-11112 (2009).
- [18] R. A. Flynn, C. S. Kim, I. Vurgaftman, M. Kim, J. R. Meyer, A. J. Mäkinen, K. Bussmann, L. Cheng, F. S. Choa, and J. P. Long, “A room-temperature semiconductor spaser operating near  $1.5 \mu\text{m}$ ”, *Opt. Exp.* 19, 8954-8961, (2011).
- [19] M. J. H. Marell, B. Smalbrugge, E. J. Geluk, P. J. van Veldhoven, B. Barcones, B. Koopmans, R. Nötzel, M. K. Smit, and M. T. Hill, “Plasmonic distributed feedback lasers at telecommunications wavelengths”, *Opt. Exp.* 19, 15109-15118, (2011).
- [20] C. Hahn, S. H. Song, C. H. Oh, and P. Berini, “Single-mode lasers and parity-time symmetry broken gratings based on active dielectric-loaded long-range surface plasmon polariton waveguides”, *Opt. Exp.* 23, 19922-19931, (2015).
- [21] D. Zhang, S. Chen, Y. Huang, Z. Zhang, Y. Wang, and D. Ma, “Surface-plasmon-enhanced lasing emission based on polymer distributed feedback laser”, *J. App. Phys.* 117, 023106, (2015).
- [22] E. K. Keshmarzi, R. N. Tait, and P. Berini, “Long-range surface plasmon single-mode laser concepts”, *J. Appl. Phys.* 112 (6), 063115, (2012).
- [23] I. De Leon and P. Berini, “Theory of noise in high-gain surface plasmon-polariton amplifiers incorporating dipolar gain media”, *Opt. Exp.* 19, 20506-20517, (2011).
- [24] S. Kéna-Cohen, P. N. Stavrinou, D. D. C. Bradley, and S. A. Maier, Confined surface plasmon polariton amplifiers, *Nano Lett.* 13, 1323-1329, (2013).
- [25] I. De Leon, and P. Berini, Amplification of long-range surface plasmons by a dipolar gain medium, *Nat. Photonics* 4, 382–387, (2010).
- [26] M. A. Bourgeois, E. K. Keshmarzi, R. N. Tait, and P. Berini, “Gain optimisation and bleaching of IR-140 doped PMMA”, manuscript submitted for publication.
- [27] P., “Long-range surface plasmon polaritons”, *Adv. Opt. and Phot.* 1, 484-588, (2009).
- [28] H. Kogelnik and C. V. Shank, “Coupled-wave theory of distributed feedback lasers”, *J. Appl. Phys.* 43, 2327 (1972).
- [29] [www.Refractiveindex.info](http://www.Refractiveindex.info).
- [30] E. K. Keshmarzi, R. N. Tait, and P. Berini, “Near infrared amplified spontaneous emission in a dye-doped polymeric waveguide for active plasmonic applications”, *Opt. Exp.* 22, 12452–12460 (2014).
- [31] L. Dal Negro, P. Bettotti, M. Cazzanelli, D. Pacifici, and L. Pavesi, “Applicability conditions and experimental analysis of the variable stripe length method for gain measurements,” *Opt. Commun.* 229(1-6), 337–348 (2004).
- [32] P. Berini, R. Charbonneau, N. Lahoud, and G. Mattiussi, *J. Appl. Phys.* 98, 043109 (2005).

#### 4.4 Surface plasmon DFB laser optimization on alternative substrates

The refractive index difference between SiO<sub>2</sub> ( $n_{SiO_2} \sim 1.452$ ) and 0.9wt% IR-140 doped PMMA ( $n_{PMMA} \sim 1.506$ ) reduces the available mode power gain in the  $ss_b^0$  mode in the LRSPP structure. The design range and performance of DFB lasers can be improved by using substrates with refractive indices closer to the refractive index of the doped PMMA. Pyrex with refractive index  $n_{Pyrex} \sim 1.47$  is a reasonable and cost effective substrate which has been considered and DFB designs have been completed using it. It will be seen in this section that the design range increases with this substrate as opposed to Silica, however; wafer dicing and facet polishing will be required for this substrate.

##### 4.4.1 DFB lasers' design using Pyrex substrate

The refractive index of a Pyrex optical wafer is about 1.47 at near infrared wavelengths. The thickness of IR-140 doped PMMA needs to be modified using Pyrex as the new substrate, since the cut-off thicknesses for TE and TM polarized slab modes will change. Figure 12 provides the effective index of the LRSPP, TE and TM polarized slab modes in comparison to the index of a Pyrex substrate. This figure is equivalent to Fig. 2 in the article of section 4.3, only Pyrex replaces SiO<sub>2</sub> as the substrate. The guided mode is cut off where its effective index is less than the substrate's index (i.e.  $n_{eff} < 1.47$ ). According to Figure 12, the cut-off of the LRSPP mode occurs at  $t_{PMMA-LRSPP} \sim 500$  nm using either metal stripe material. The TE and TM polarized slab modes are cut off at  $t_{PMMA-TE} \sim 550$  nm and  $t_{PMMA-TM} \sim 620$  nm, respectively. Neglecting the TE mode, as it can be simply filtered out by a polarizing cube, the acceptable doped PMMA thickness is in the range of  $500 \text{ nm} < t_{PMMA} < 620 \text{ nm}$ .

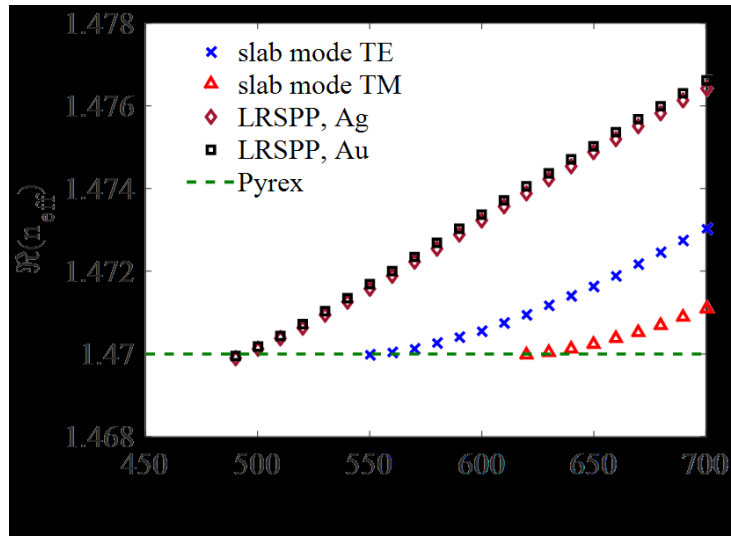


Figure 12 Effective indices of TE and TM slab modes in doped PMMA on Pyrex, and the LRSPP mode's effective index supported in a 20 nm-thick, 1  $\mu\text{m}$ -wide Au and Ag stripe on Pyrex, and covered with doped PMMA. Index of Pyrex substrate is plotted for comparison and specifying the cut-off regions

For the DFB design we would like to maximize the mode power gain (MPG), within the acceptable  $t_{PMMA}$  range. Figure 13 plots MPG versus doped PMMA thickness for the LRSPPs using 20 nm-thick, 1  $\mu\text{m}$ -wide Ag or Au metal stripes on a Pyrex substrate.

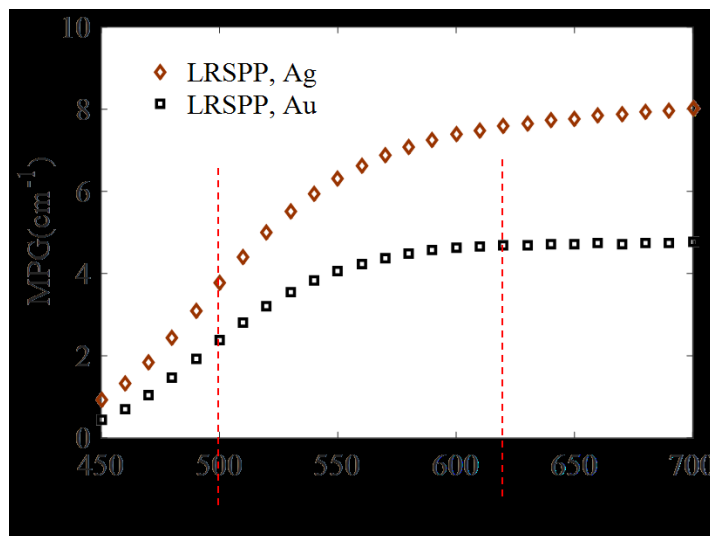
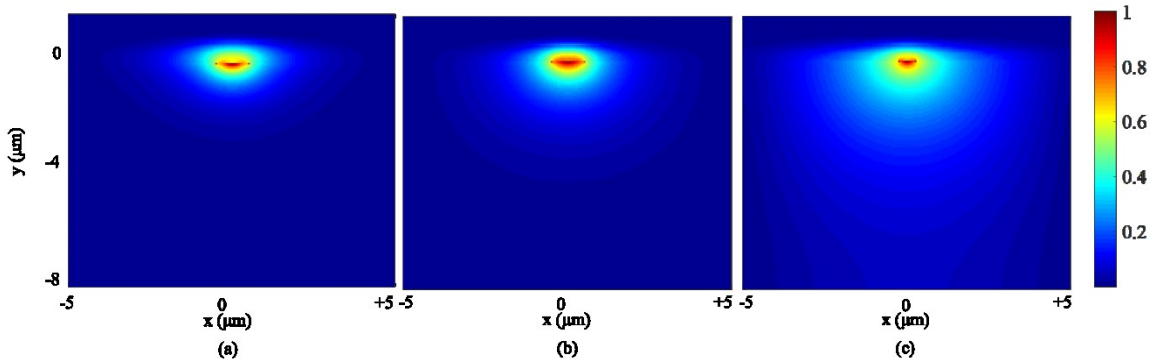


Figure 13 MPG ( $\text{cm}^{-1}$ ) versus doped PMMA thickness for the LRSPPs using 20 nm-thick, 1  $\mu\text{m}$ -wide Ag or Au on a Pyrex substrate

In contrast to Fig. 3 in the article of section 4.3, the LRSPPs' MPG using Pyrex substrate is always positive. This means that the DFBs' design range is only limited by the LRSPP and TM modes' cut-off region, i.e.  $500 \text{ nm} < t_{PMMA} < 620 \text{ nm}$  which is specified by the dashed lines in Figure 13. Also MPG in Figure 13 is almost two orders of magnitude larger than MPG using Silica. Larger MPG is preferred in DFB laser design, and as Figure 13 suggests, thicker IR-140 doped PMMA is better. However, it should be noted that the LRSPP's MPG eventually saturates with increasing  $t_{PMMA}$ , as is seen in Figure 13. In practice also it is not good to increase  $t_{PMMA}$  unnecessarily, since the pump intensity can weaken in a thicker doped PMMA film. Moreover, numerical computation of the  $ss_b^0$  mode's field distribution shows that a thicker doped PMMA layer can alter the symmetry of the  $ss_b^0$  mode. Figure 14(a) shows the  $ss_b^0$  mode's field distribution in a LRSPP structure with a 20 nm-thick, 1  $\mu\text{m}$ -width Au stripe on a Pyrex substrate using a 700 nm-thick doped PMMA layer.



**Figure 14 Computed LRSPP mode electric field distribution for (a) 20nm-thick, 1  $\mu\text{m}$  wide Au stripe and 700 nm-thick PMMA, (b) 20nm-thick, 1  $\mu\text{m}$  wide Au stripe and 600 nm-thick PMMA, (c) 20nm-thick, 0.5  $\mu\text{m}$  wide Au stripe and 600 nm-thick PMMA, all on Pyrex substrate**

Figure 14 (b), shows the mode's profile using the same Au stripe but with a thinner doped PMMA layer of  $t_{PMMA} = 600 \text{ nm}$ . The  $ss_b^0$  mode looks more symmetric in the

thinner doped PMMA (Figure 14 (b)) compared to the thicker film (Figure 14 (a)), while both doped PMMA layers produce almost the same MPG  $\sim 4.5\text{cm}^{-1}$ . Figure 14 (c) shows the  $ss_b^0$  mode's profile in a 20 nm-thick, 0.5  $\mu\text{m}$ -wide Au stripe on Pyrex and with  $t_{PMMA} = 600$  nm.

We follow the lasers' design by considering a 600 nm-thick IR-140 doped PMMA on the Pyrex substrate, and for 20 nm-thick stepped-in-width Ag and Au Bragg gratings. The average refractive index in Ag and Au Bragg gratings are found using a numerical solver, COMSOL Multiphysics v.5.2., with both values equal to  $n_{ave} = 1.4718$ . The pitch of the first order Bragg grating for lasing at  $\lambda_0 = 882$  nm is then computed as  $\Lambda = \lambda_0/2n_{ave} \sim 300$  nm.

The coupling and mode gain coefficients in Ag and Au Bragg gratings are obtained as  $\kappa_{Au} = 73 \text{ cm}^{-1}$ ,  $\kappa_{Ag} = 66 \text{ cm}^{-1}$ ,  $\alpha_{Au} = 2.3 \text{ cm}^{-1}$ , and  $\alpha_{Ag} = 3.3 \text{ cm}^{-1}$ . Following the laser design methodology in the article (part B., section II), the minimum and maximum DFB lengths for single mode lasing in Ag and Au DFBs, are obtained as  $L_{min-Ag} = 1.5$  mm,  $L_{max-Ag} = 3.3$  mm, and  $L_{min-Au} = 2.2$  mm,  $L_{max-Au} = 4.8$  mm. It is interesting to note that although the gain constant in Au DFBs is smaller than that in Ag DFBs ( $\alpha_{Au} < \alpha_{Ag}$ ), however; Au DFBs produce larger coupling coefficients which compensates for the lower gain constant.

## 5. PT symmetry Bragg gratings based on LRSPP structure

### 5.1 Summary

It is shown in quantum mechanics that non-Hermitian Hamiltonians respecting a parity-time (PT) symmetry condition can generate real eigenvalues. Hamiltonians with a complex potential  $V$  as a function of position  $r$  obeying the condition  $V(r) = V^*(-r)$ , with  $*$  denoting the complex conjugate, are PT symmetric. By forming analogy between the corresponding equations of quantum mechanics and optics it is easy to show that the refractive index plays the role of the potential in optics and photonic systems satisfying  $n(\mathbf{r}) = n^*(-\mathbf{r})$  are PT symmetric. PT symmetric optical materials are realized by judiciously manipulating the complex refractive index to produce even- and odd-symmetric distributions for the real and imaginary indices, respectively. These artificial materials have gained great attention due to their extraordinary behaviour at a so-called exceptional point where the PT symmetry breaks abruptly.

In this chapter, two PT symmetric Bragg grating structures are introduced operating in a LRSPP structure near the exceptional point. The Bragg gratings are proposed and designed to produce asymmetric reflectance for signals incident from the left or right of the grating. The non-reciprocal reflectance is due to the unidirectional coupling coefficient between the forward and backward propagating modes and is not against Lorentz reciprocity theorem in linear systems. In both structures index modulation is implemented by stepping the width of a metal stripe in a LRSPP waveguide. To generate gain/loss modulation, the first PT symmetric Bragg grating uses a PMMA top cladding which covers the metal stripe and is periodically doped by IR-140 [95]. Step-in-width IR-140 doped PMMA stripes covering the metal stripe are used for

gain/loss perturbation in the second PT symmetric structure [96]. Both structures lead to the same functionalities but the fabrication processes will be significantly different.

## **5.2 Contribution**

The results provided in this chapter were published in two journals, first one in Applied Physics Letters, and the second one in Applied Physics A. I proposed and designed the structures, modeled them by modal analysis and the TMM method. I interpreted the results and wrote the manuscripts. Dr. Tait and Dr. Berini contributed to the interpretation of the results, and revised the manuscript.

## **5.3 Articles**

The published articles follow verbatim.

## Spatially nonreciprocal Bragg gratings based on surface plasmons

Elham Karami Keshmarzi,<sup>1</sup> R. Niall Tait,<sup>1</sup> and Pierre Berini<sup>2,3,4</sup>

<sup>1</sup>Department of Electronics, Carleton University, 1125 Colonel By Dr., Ottawa, Ontario K1S 5B6, Canada

<sup>2</sup>School of Electrical Engineering and Computer Science, University of Ottawa, Ottawa, Ontario K1N 6N5, Canada

<sup>3</sup>Department of Physics, University of Ottawa, Ottawa, Ontario K1N 6N5, Canada

<sup>4</sup>Center for Research in Photonics, University of Ottawa, Ottawa, Ontario K1N 5N6, Canada

(Received 16 July 2014; accepted 31 October 2014; published online 12 November 2014)

Using the concept of parity-time symmetry in optics, we propose a spatially non-reciprocal Bragg grating at near infrared wavelengths, operating with long-range surface plasmon polaritons, by employing balanced modulation of index and gain/loss in a step-in-width configuration. The index perturbation is created by stepping the width of an Ag stripe supporting long-range plasmons. Gain/loss modulation is generated by periodically doping the top polymer cladding of the structure with IR-140 dye molecules and pumping the grating optically from top. Loss exists inherently in the undoped regions due to plasmonic propagation loss. The transmission matrix method was employed as an accurate modeling technique to compute the reflectance and transmittance spectra of the proposed structures. Simulation results exhibit a strong reflectance from one end of the grating at about 880 nm as opposed to nearly no reflectance from the other end at the same wavelength.

© 2014 AIP Publishing LLC. [<http://dx.doi.org/10.1063/1.4901818>]

Parity-time (PT) symmetric materials operating at the so-called exceptional point have shown the ability of unusually manipulating and controlling light propagation.<sup>1</sup> These synthetic materials are created by judiciously encompassing gain and loss in the structure such that the refractive index of the medium follows  $n(z) = n^*(-z)$ .<sup>1-5</sup> This is a necessary but insufficient condition for having PT symmetry.<sup>6</sup> In fact, by adjusting the refractive index of the structure at a certain critical threshold, PT symmetry breaks down abruptly. This threshold breaking is referred to as an exceptional point or spontaneous phase transition, where many intriguing optical phenomena can be observed. In the unbroken PT symmetric state, the eigenvalues of the optical Hamiltonian are purely real. PT symmetry breakdown is accompanied by merging of the eigenvalues. In the broken state, eigenvalues will again split and form a complex conjugate pair.<sup>7</sup> Double refraction and non-reciprocal refraction,<sup>8</sup> unidirectional Bloch oscillations,<sup>9</sup> unidirectional coupling in contra-directional couplers,<sup>10-12</sup> and in GACC (grating assisted co-directional couplers)<sup>4,13</sup> are examples of effects and devices employing PT symmetric structures near an exceptional point.

A Bragg grating with matched modulation of real (index) and imaginary (gain/loss) refractive index, where the perturbation of gain/loss versus the real index perturbation is quarter-period shifted spatially, is an example of a PT symmetric structure operating at the breaking threshold. The refractive index distribution of such a Bragg grating can be written as

$$n(z) = n_0 + \Delta n_0 \exp\left(\pm j \frac{2\pi}{\Lambda} z\right), \quad (1)$$

where  $\Lambda$  is the period of the grating. Using coupled mode theory, coupling from the forward to the backward propagating mode is directly related to the Fourier components of the periodic refractive index. For a refractive index with single

sideband spectrum, such as the one given in Eq. (1), there will be unidirectional coupling between the forward and backward propagating modes and non-reciprocal Bragg grating (NRBG) results. It is important to note that non-reciprocity in this context refers to unidirectional coupling which causes a spatially nonreciprocal reflectance, and is not in contradiction to the Lorentz reciprocity theorem.

The concept of NRBGs was proposed in general by Poladian,<sup>14</sup> where using the theory of resonance modes in linear and non-uniform gratings, he showed that hybrid index and gain/loss gratings generate asymmetric reflectance spectra within contra-propagating waveguide couplers. He indicated that an ideal NRBG (defined further below) could be obtained by perfectly matching the index and gain/loss modulations while shifting them exactly 90° out of phase. Kulishov *et al.*<sup>10</sup> later presented a detailed theoretical study based on coupled mode theory and explored the reflectance/transmittance spectra as well as the dispersion characteristics. The effects on the spectral characteristics of deviation from the ideal NRBG conditions were also investigated therein.<sup>10</sup>

Loss in plasmonic systems facilitates the realization of PT symmetric devices because the loss is intrinsic and it can be finely adjusted through geometrical adjustments. Many PT symmetry studies are now being conducted with plasmonic systems.<sup>3,15-18</sup> These studies are becoming more realistic as gain is introduced and implemented in plasmonic waveguides, and found to produce amplification.<sup>19-21</sup>

In this letter, PT symmetry is applied in a waveguide Bragg grating structure supporting long-range surface plasmon polaritons (LRSPPs) as the basis of a NRBG. The proposed structure offers a single sideband modulation of the refractive index similar to Eq. (1) which gives rise to a NRBG. Reciprocal LRSPP Bragg gratings have been previously studied,<sup>22</sup> implemented,<sup>23,24</sup> and suggested as the cavity mirrors in LRSPP lasers.<sup>25</sup> Such gratings<sup>22-24</sup> produce

mainly a modulation of the real refractive index by stepping the width of the metal stripe used in their implementation. LRSPP Bragg gratings based on step in thickness also produce index modulation in stronger manner.<sup>26</sup> In this work, we introduce modulation of imaginary refractive index (gain/loss) into step in width LRSPP gratings by periodically doping the top polymer cladding of the structure with dye molecules. Fig. 1 shows the proposed NRBG architecture.

A 20 nm thick Ag stripe is assumed deposited on a fused silica substrate. The index grating is created by stepping the width of the Ag stripe on a pitch of  $\Lambda$  with a 50% duty cycle. Gratings  $G_1$ ,  $G_2$ , and  $G_3$  are proposed from the following step-in-width, respectively:  $(w_1, w_2) = (1 \mu\text{m}, 0.5 \mu\text{m})$ ,  $(w_1, w_2) = (1 \mu\text{m}, 0.9 \mu\text{m})$ , and  $(w_1, w_2) = (1 \mu\text{m}, 0.96 \mu\text{m})$ . All gratings are first order, and their lengths vary with the number of unit cells selected as follows:  $N_1 = 3000$ ,  $N_2 = 4000$ ,  $N_3 = 5000$ , and  $N_4 = 6000$ . A 1  $\mu\text{m}$  thick, 4  $\mu\text{m}$  wide PMMA layer covers the Ag grating over its entire length and is periodically doped with dye molecules (IR-140 is assumed) following the same period and duty cycle as the Ag step-in-width grating ( $\Lambda$  and 50%), but is shifted spatially by a quarter period ( $\Lambda/4$ ) in order to generate the  $90^\circ$  phase difference required between the real and imaginary modulations of refractive index (Fig. 1(b)). The thickness and width of the PMMA regions were selected such that LRSPPs can be supported in this asymmetric structure—the index of PMMA is higher than that of fused silica, so a thin layer of PMMA covered by air can effectively match the index of the fused silica, thus enabling LRSPPs to be supported.<sup>27</sup>

IR-140 is a commercial dye molecule with peak absorption and emission wavelengths at about  $\lambda_p = 810 \text{ nm}$  and  $\lambda_e = 880 \text{ nm}$ , respectively.<sup>19</sup> The IR-140 to PMMA weight ratio is assumed to be 0.8 wt. % in the doped regions. The whole grating length is assumed pumped optically from the top using 10 ns, 500 MW/cm<sup>2</sup> laser pulses at

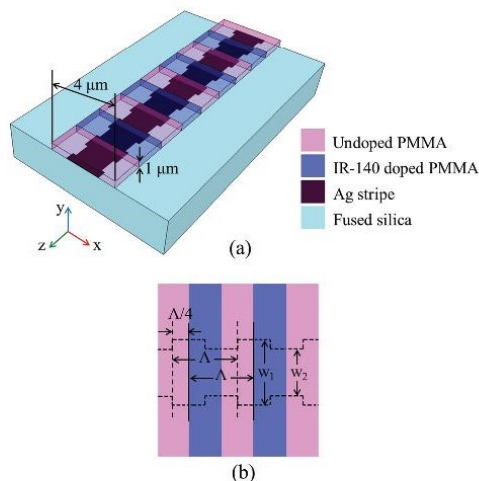


FIG. 1. (a) Proposed NRBG architecture. (b) Top view of the structure. Ag step-in-width metal stripe grating shown in black dashed outline. An undoped/doped PMMA (Poly methyl methacrylate) grating of the same period as the Ag step-in-width grating is overlaid but shifted  $\Lambda/4$  spatially with respect to the latter.

810 nm. It was experimentally demonstrated<sup>28</sup> that this gain medium (under the conditions mentioned) provides a TM material gain of about  $68 \text{ cm}^{-1}$ . This is the material gain assumed herein for the doped PMMA regions. The design Bragg wavelength is selected as  $\lambda_B = 880 \text{ nm}$  which corresponds to the peak emission wavelength of IR-140 in PMMA at the given concentration.<sup>28</sup>

Alternate gain and loss with a  $\Lambda/4$  offset with respect to the Ag step-in-width, forms four LRSPP waveguide sections of equal length within the unit cell of the gratings. For instance, in grating  $G_1$ , there will be passive and active 1  $\mu\text{m}$  wide as well as passive and active 0.5  $\mu\text{m}$  wide sections. The LRSPP mode in each section is approximated by a plane wave propagating longitudinally along the stripe, and the equivalent dielectric stack model is applied to model the structure.<sup>22</sup> In this model, which was proven reliable in comparisons between theoretical and experimental results for LRSPP Bragg gratings,<sup>23,24</sup> each LRSPP waveguide section is assigned to a dielectric layer of refractive index equal to the complex effective index of the LRSPP in that section.

The LRSPP's effective index in each section was computed using a commercial numerical mode solver. Figs. 2(a) and 2(b) show the normalized distribution of the main transverse field component ( $E_y$ ) of the LRSPP mode in passive 0.5  $\mu\text{m}$  and 1  $\mu\text{m}$  wide sections, respectively.

The pitch of the gratings is determined by the Bragg wavelength and also the average effective index of refraction in the grating, as is given in Eq. (2)<sup>22</sup>

$$\Lambda = \frac{\lambda_B}{2n_{ave}}, \quad (2)$$

where  $n_{ave}$  is the average effective index of refraction,  $n_{ave} = Re(n_{eff1} + n_{eff2} + n_{eff3} + n_{eff4})/4$ , and  $n_{effi}$   $i = 1:4$  is the mode complex effective index in  $i$ th section.  $n_{ave}$  was obtained for gratings  $G_1$ ,  $G_2$ , and  $G_3$  as 1.4554, 1.4613, and 1.4615, respectively. Using Eq. (2), the grating pitch for  $G_1$ ,  $G_2$ , and  $G_3$  will be approximately 300 nm, from which the physical length of the grating will be in the range of 0.9 mm to 1.8 mm. The active LRSPP waveguide, experimented in Ref. 19 using IR-140 molecules in the solution, has been 1.524 mm long.

The transfer matrix method<sup>29</sup> was applied to the grating structures and reflectance/transmittance spectra were

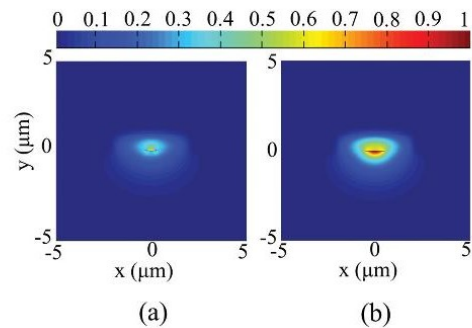


FIG. 2. Normalized  $E_y$  field distribution in the cross section of (a) 0.5  $\mu\text{m}$  and (b) 1  $\mu\text{m}$  wide passive LRSPP waveguide sections.

computed. Figs. 3(a) and 3(b) show the reflectance and transmittance spectra of  $G_1$ ,  $G_2$ , and  $G_3$  for  $N = 3000$ .

Non-reciprocal reflectance is observed in Fig. 3(a); however, the transmittance spectra are symmetric. The theory given in the supplementary material clarifies why the transmittance is always symmetric.

The contrast ratio ( $C$ ) is defined to measure the level of non-reciprocity<sup>11</sup>

$$C = \left| \frac{R_r - R_l}{R_r + R_l} \right|, \quad (3)$$

where  $R_r$  and  $R_l$  are the right-incident and left-incident reflectance respectively. Using Eq. (3), we obtain:  $C_{G1} = 0.20$ ,  $C_{G2} = 0.62$ , and  $C_{G3} = 0.99$ . Therefore,  $G_3$  approaches the performance of an ideal NRBG ( $C = 1$ ). The ratio of index modulation to gain/loss modulation ( $\Delta n/\Delta k$ ) in the three gratings are, respectively, 8.6, 2.9, and 1.1, which indicates that grating  $G_3$  has the most balanced perturbation of index versus gain/loss among the three gratings.

Fig. 4 shows the reflectance response of  $G_3$  as its length varies by increasing the number of unit cells from 3000 to 6000. The peak reflectance increases as expected, however, at a high number of unit cells (i.e., above 5000), 100% reflectance, and even amplified reflectance, is observed. Thus, a reflectance equal to or greater than unity is one of the features that can be provided by PT symmetric structures.

To have considered our devices' performance in practice, design robustness in terms of gain variations in doped

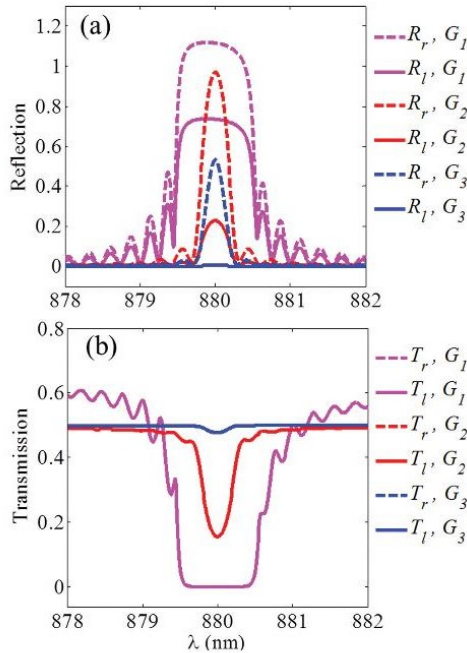


FIG. 3. (a) Reflectance spectra and (b) transmittance spectra for gratings  $G_1$ ,  $G_2$ , and  $G_3$  at  $N = 3000$ .  $R_r$ ,  $R_l$ : right- and left- incident reflectance;  $T_r$ ,  $T_l$ : right- and left-incident transmittance.

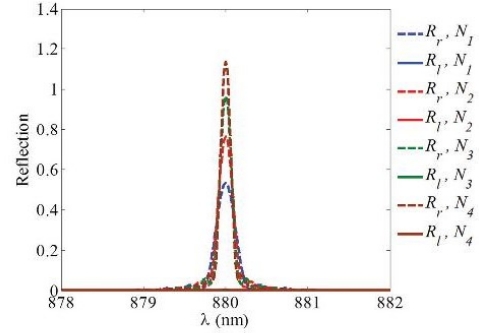


FIG. 4. Reflectance spectra of grating  $G_3$  for  $N$  varying from 3000 to 6000. Amplified reflectance is observed for  $N > 5000$ .

regions as well as the effect of offset in modulation of real versus imaginary index from the reference quadrature situation were taken into account. Fig. 5 plots the contrast ratio  $C$  as a function of gain where the phase difference is fixed at  $\Lambda/4$ , and also as function of phase difference as the gain is fixed at  $68 \text{ cm}^{-1}$ .

As it is observed from the gain curve, if the gain coefficient changes in the range of  $45 \text{ cm}^{-1}$  to  $114 \text{ cm}^{-1}$ , the contrast ratio will remain above 90%. From the phase shift curve, by varying the phase shift between modulation of the real and imaginary indices from  $63^\circ$  to  $114^\circ$ , the contrast ratio still remains above 90%. This phase variation corresponds to a spatial shift of  $0.17 \Lambda$  to  $0.32 \Lambda$ , or equivalently spanning a 45 nm displacement, which is quite large given the resolution of, say, e-beam lithography or deep UV lithography tools. These results indicate that there is reasonable margin for realizing a high contrast NRBG.

In summary, we proposed a spatially NRBG concept by operating at the breaking threshold of PT symmetry. Matched perturbations of index with gain/loss and a  $\Lambda/4$  spatial shift between them are combined in an asymmetric LRSP step-in-width waveguide Bragg grating configuration. The transfer matrix method was used to compute the reflectance and

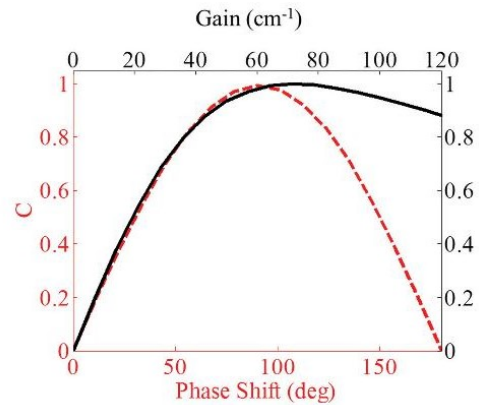


FIG. 5. Contrast ratio versus gain (black) and phase shift between modulation of real and imaginary indices (dashed-red).

transmittance spectra. Near-ideal non-reciprocal reflectance is predicted along with amplified reflectance in an experimentally realisable structure.

- <sup>1</sup>X. Yin and X. Zhang, *Nat. Mater.* **12**, 175–177 (2013).
- <sup>2</sup>A. Regensburger, Ch. Bersch, M. A. Miri, G. Onishchukov, D. N. Christodoulides, and U. Peschel, *Nature* **488**, 167–171 (2012).
- <sup>3</sup>H. Alaeian and J. A. Dionne, *Phys. Rev. A* **89**, 033829 (2014).
- <sup>4</sup>M. Kulishov and B. Kress, *Opt. Express* **21**, 22327–22337 (2013).
- <sup>5</sup>H. Ramezani, T. Kottos, R. El-Ganainy, and D. N. Christodoulides, *Phys. Rev. A* **82**, 043803 (2010).
- <sup>6</sup>H. E. Rüter, K. G. Makris, R. El-Ganainy, D. N. Christodoulides, M. Segev, and D. Kip, *Nat. Phys.* **6**, 192–195 (2010).
- <sup>7</sup>See supplementary material at <http://dx.doi.org/10.1063/1.4901818> for additional details on Hamiltonian of a generic Bragg grating.
- <sup>8</sup>K. G. Makris, R. El-Ganainy, D. N. Christodoulides, and Z. H. Musslimani, *Phys. Rev. Lett.* **100**, 103904 (2008).
- <sup>9</sup>E. M. Graefe and H. F. Jones, *Phys. Rev. A* **84**, 013818 (2011).
- <sup>10</sup>M. Kulishov, J. M. Laniel, N. Bélanger, J. Azaña, and D. V. Plant, *Opt. Express* **13**, 3068–3078 (2005).
- <sup>11</sup>L. Feng, Ye. L. Xu, W. S. Fegadolli, M-Hui. Lu, J. E. B. Oliveira, V. R. Almeida, Y. F. Chen, and A. Scherer, *Nat. Mater.* **12**, 108–113 (2013).
- <sup>12</sup>L. Feng, X. Zhu, S. Yang, H. Zhu, P. Zhang, X. Yin, Y. Wang, and X. Zhang, *Opt. Express* **22**, 1760–1767 (2014).
- <sup>13</sup>M. Kulishov, J. M. Laniel, N. Bélanger, and D. V. Plant, *Opt. Express* **13**, 3567–3578 (2005).
- <sup>14</sup>L. Poladian, *Phys. Rev. E* **54**, 2963 (1996).
- <sup>15</sup>H. Benisty, A. Degiron, A. De Lustrac, S. Chenais, S. Forget, M. Besbes, G. Barbillon, A. Bruyant, S. Blaize, and G. Lerondel, *Opt. Express* **19**, 18004–18019 (2011).
- <sup>16</sup>A. Lupu, H. Benisty, and A. Degiron, *Opt. Express* **21**, 21651–21668 (2013).
- <sup>17</sup>H. Alaeian and J. A. Dionne, *Phys. Rev. B* **89**, 075136 (2014).
- <sup>18</sup>J. Han, Y. Fan, L. Jin, Z. Zhang, Z. Wei, C. Wu, J. Qiu, H. Chen, and H. Li, *J. Opt.* **16**, 045002 (2014).
- <sup>19</sup>I. De Leon and P. Berini, *Nat. Photon.* **4**, 382–387 (2010).
- <sup>20</sup>M. C. Gather, K. Meerholz, N. Danz, and K. Leosson, *Nat. Photonics* **4**, 457–461 (2010).
- <sup>21</sup>S. Kéna-Cohen, P. N. Stavrinou, D. D. C. Bradley, and S. A. Maier, *Nano Lett.* **13**, 1323–1329 (2013).
- <sup>22</sup>S. Jetté-Charbonneau and P. Berini, *J. Opt. Soc. Am. A* **23**, 1757–1767 (2006).
- <sup>23</sup>S. Jetté-Charbonneau, R. Charbonneau, N. Lahoud, G. Mattiussi, and P. Berini, *Opt. Express* **13**, 4674–4682 (2005).
- <sup>24</sup>S. Jetté-Charbonneau and P. Berini, *IEEE J. Quant. Electr.* **41**, 1480–1491 (2005).
- <sup>25</sup>E. K. Keshmarzi, R. N. Tait, and P. Berini, *J. Appl. Phys.* **112**, 063115 (2012).
- <sup>26</sup>A. Boltasseva, S. I. Bozhevolnyi, T. Nikolajsen, and K. Leosson, *J. Lightwave Technol.* **24**, 912–918 (2006).
- <sup>27</sup>P. Berini, *Adv. Opt. Photonics*, **1**, 484–588 (2009).
- <sup>28</sup>E. K. Keshmarzi, R. N. Tait, and P. Berini, *Opt. Express* **22**, 12452–12460 (2014).
- <sup>29</sup>P. Yeh, *Optical Waves in Layered Media* (Wiley, Toronto, 1988).

## Parity-time symmetry-broken Bragg grating operating with long-range surface plasmon polaritons

Elham Karami Keshmarzi<sup>1</sup>  · R. Niall Tait<sup>1</sup> · Pierre Berini<sup>2,3,4</sup>

Received: 9 September 2015 / Accepted: 8 November 2015 / Published online: 7 March 2016  
© Springer-Verlag Berlin Heidelberg 2016

**Abstract** A parity-time symmetry-broken Bragg grating concept, comprising step-in-width IR-140 doped PMMA stripes covering step-in-width Au stripes on a fused silica substrate and operating with long-range surface plasmon polaritons, is reported. The design methodology is outlined, structures are modelled using a combination of modal analysis and the transfer matrix method, and reflectance and transmittance responses are computed. The design robustness with respect to deviations in the dimensions due to fabrication error is also investigated. The structure is capable of producing a reflectance contrast ratio of 1 over optical bandwidths of 879.96–880.04 nm.

### 1 Introduction

The concept of parity-time (PT) symmetry, originating from quantum mechanics, is a property of a Hamiltonian operator by which a non-Hermitian Hamiltonian could possess entirely real eigenvalues [1]. In quantum mechanics, it is known that a necessary (but insufficient) condition for PT symmetry is to have a potential energy function that follows  $v(x) = v^*(-x)$  [2]. By analogy, the

refractive index  $n(x)$  in optics plays the same role as the potential energy  $v(x)$  so that PT symmetry in photonics exists if  $n(x) = n^*(-x)$ . In fact, photonic structures are suitable for the observation of PT symmetric non-Hermitian Hamiltonians [3]. By tweaking the refractive index distribution in photonics, synthetic materials with unique properties are created [4–8].

Specifically, most of the attention in recent years has been on PT symmetry-broken structures operating near their breaking threshold where many interesting and unusual phenomena are observed [9–14]. One example of a structure operating at the breaking threshold of PT symmetry is a Bragg grating with a balanced perturbation of index versus gain/loss and 90° phase shift between these perturbations.

It is shown that in such gratings the coupling between contra-directional modes is unidirectional and asymmetric reflectance from input/output facets is obtained [14, 15]. A general schematic of a PT symmetry-broken Bragg grating is shown in Fig. 1 where there is a square perturbation of the real refractive index and of the gain/loss, of the same period  $\Lambda$ , but with a  $\Lambda/4$  spatial shift between them. The step in index is the same as the magnitude of the step in gain or loss, i.e.  $\Delta n = \Delta k$ . The unit cell consists of four sections of equal length (each  $\Lambda/4$ ) and the following refractive indices:  $n_1 = n + \Delta n + jk$ ,  $n_2 = n + \Delta n + j(k + \Delta k)$ ,  $n_3 = n + j(k + \Delta k)$  and  $n_4 = n + jk$ .

The Bragg grating we introduce in this paper follows this concept and operates with long-range surface plasmon polaritons (LRSPPs). Figure 2a gives a sketch of the structure's architecture and Fig. 2b of the unit cell. A 20-nm-thick step-in-width Au stripe is deposited on a fused silica substrate and then covered by a 600-nm-thick step-in-width doped PMMA stripe.

✉ Elham Karami Keshmarzi  
ekkeshma@doe.carleton.ca

<sup>1</sup> Department of Electronics, Carleton University, 1125 Colonel By Dr., Ottawa, ON K1S 5B6, Canada  
<sup>2</sup> School of Electrical Engineering and Computer Science, University of Ottawa, Ottawa, ON K1N 6N5, Canada  
<sup>3</sup> Department of Physics, University of Ottawa, Ottawa, ON K1N 6N5, Canada  
<sup>4</sup> Center for Research in Photonics, University of Ottawa, Ottawa, ON K1N 5N6, Canada

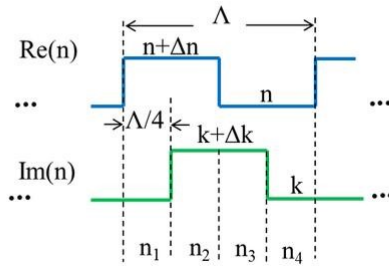


**Fig. 1** Longitudinal distribution within a unit cell of the real and imaginary index of refraction with balanced perturbations ( $\Delta n = \Delta k$ ) of the same period ( $\Lambda$ ) but with a spatial shift ( $\Lambda/4$ ) between them, resulting in a PT symmetry-broken Bragg grating

The thickness of the doped PMMA is selected so that its refractive index in combination with air on top effectively matches that of fused silica at the operating wavelength of 880 nm such that the structure supports LRSPPs. This thickness also ensures that all TE and TM PMMA slab modes will be cut off. The PMMA is doped with laser dye molecules IR-140 with a peak emission wavelength of 880 nm. The material gain of this medium was measured to be about  $68 \text{ cm}^{-1}$  when it is optically pumped from the top with  $500 \text{ MW/cm}^2$  laser pulses at 810 nm [16]. As sketched in Fig. 2b, the unit cell of the Bragg grating comprises four sections of specific Au and doped PMMA widths which result in specific complex effective indices of refraction. The arrangement of effective refractive indices in the unit cell is such that it follows the general distribution of Fig. 1.

## 2 Modelling results

The thickness of the doped PMMA was determined such that the TE and TM PMMA slab modes are cut off and only LRSPPs can propagate along the Bragg grating. Using a commercial numerical mode solver based on the finite element method, the complex effective index of refraction of TE and TM modes in a slab waveguide comprising fused silica, doped PMMA and air was computed as a function of the doped PMMA thickness ( $t_{\text{PMMA}}$ ). The complex effective index of LRSPP mode in a waveguide comprising fused silica, 20 nm thick- $1 \mu\text{m}$  Au covered by doped PMMA, and air was also computed as a function of  $t_{\text{PMMA}}$ . Figure 3 shows the real effective index of the first TE and TM slab modes along with the LRSPP mode versus PMMA thickness at  $\lambda = 880 \text{ nm}$ . The index of fused silica is also plotted for comparison.

In order to ensure that the TE and TM modes are cut off, but that the LRSPP mode propagates, we must have:

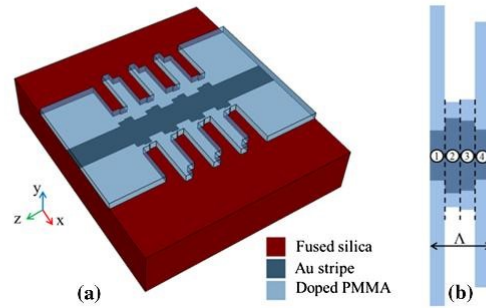


**Fig. 2** a Architecture of PT symmetry-broken Bragg grating operating with LRSPPs. b Unit cell of the Bragg grating in top view, forming four sections of effective complex refractive indices  $n_{\text{eff},i}$ ,  $i = 1:4$

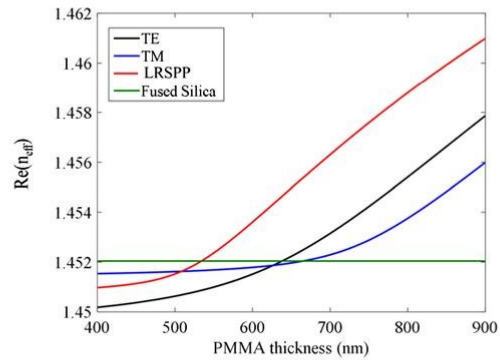


**Fig. 3** Real effective index of the first TE and TM slab modes and of the LRSPP mode versus PMMA thickness. The refractive index of fused silica is also plotted for reference

$n_{\text{eff\_TE}} < n_{\text{FS}}$ ,  $n_{\text{eff\_TM}} < n_{\text{FS}}$  and  $n_{\text{eff\_LRSPP}} > n_{\text{FS}}$ , where  $n_{\text{FS}}$  is the refractive index of fused silica. According to Fig. 3, a PMMA thickness in the range of  $\sim 535\text{--}635 \text{ nm}$  satisfies these conditions. We thus choose a PMMA thickness of  $t_{\text{PMMA}} = 600 \text{ nm}$  for our Bragg grating.

The complex effective index of the LRSPP mode was then computed as a function of the widths of the Au and doped PMMA stripes and plotted in Fig. 4a, b. In order to design a PT symmetry-broken Bragg, we arrange Bragg's unit cell such that it follows Fig. 1, i.e.  $\text{Re}\{n_{\text{eff}1}\} \approx \text{Re}\{n_{\text{eff}2}\}$ ,  $\text{Re}\{n_{\text{eff}3}\} \approx \text{Re}\{n_{\text{eff}4}\}$ ,  $\text{Im}\{n_{\text{eff}1}\} \approx \text{Im}\{n_{\text{eff}4}\}$  and  $\text{Im}\{n_{\text{eff}2}\} \approx \text{Im}\{n_{\text{eff}3}\}$ . The step in index should be approximately equal to the step in gain/loss.

The numbered markers in Fig. 4 show the real and imaginary effective indices which are selected for each section of the unit cell. From Fig. 4, we have:  $n_{\text{eff}1} = 1.453542 + j1.4 \times 10^{-5}$ ,  $n_{\text{eff}2} = 1.453535 - j4.4 \times$

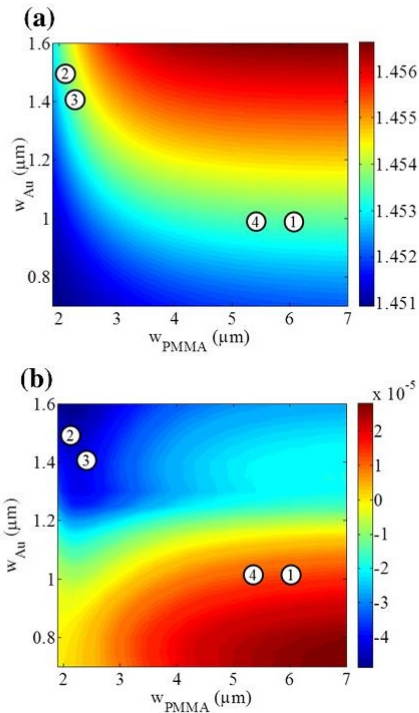
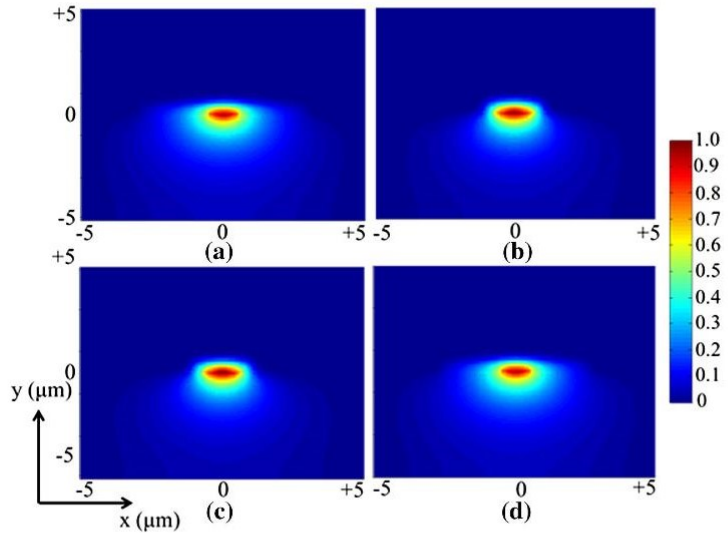


**Fig. 4** Real and imaginary effective index of the LRSPP as a function of Au and doped PMMA widths. Markers 1 to 4 specify the effective index in Sects. 1, 2, 3 and 4, respectively

**Fig. 5 a-d** Normalized distribution of the main transverse electric field component ( $E_y$ ) of the LRSPP in Sects. 1, 2, 3 and 4, respectively



$10^{-5}$ ,  $n_{\text{eff}3} = 1.453486 - j4.1 \times 10^{-5}$ , and  $n_{\text{eff}4} = 1.453493 + j1.3 \times 10^{-5}$  from which we observe  $\Delta n \approx 10^{-4}$  and  $\Delta k \approx 6 \times 10^{-5}$ . These effective indices correspond, respectively, to sections with the following Au and PMMA width pairs:  $(w_{\text{Au}1}, w_{\text{PMMA}1}) = (1, 6 \mu\text{m})$ ,  $(w_{\text{Au}2}, w_{\text{PMMA}2}) = (1.5, 2.1 \mu\text{m})$ ,  $(w_{\text{Au}3}, w_{\text{PMMA}3}) = (1.4, 2.2 \mu\text{m})$  and  $(w_{\text{Au}4}, w_{\text{PMMA}4}) = (1, 5.3 \mu\text{m})$ . Figure 5a-d gives the normalized distribution of the main transverse field component ( $E_y$ ) of the LRSPP mode in Sects. 1, 2, 3 and 4, respectively.

The pitch  $\Lambda$  of the gratings is determined by the Bragg wavelength and the average effective index of refraction in the grating through: [17]

$$\Lambda = \frac{O \lambda_B}{2n_{\text{ave}}} \tag{1}$$

where  $O$  is an integer specifying the grating order,  $\lambda_B$  is the Bragg wavelength ( $\lambda_B = 880 \text{ nm}$ , corresponding to the peak emission wavelength of IR-140),  $n_{\text{ave}} = \text{Re}\{n_{\text{eff}1} + n_{\text{eff}2} + n_{\text{eff}3} + n_{\text{eff}4}\}/4 \approx 1.4535$  is the average effective index, and  $n_{\text{eff}i}$  ( $i = 1:4$ ) is the complex effective index in the  $i$ th section.

An equivalent dielectric stack is used to model the structure. In this model, which has proven accurate for LRSPP Bragg gratings in comparisons with experimental results [18, 19], each LRSPP waveguide section is assigned to a dielectric layer of length and refractive index equal to the length and complex effective index of the LRSPP in that section. Then, the transfer matrix method [20] is applied to the stack structure, and reflectance and transmittance spectra are computed.

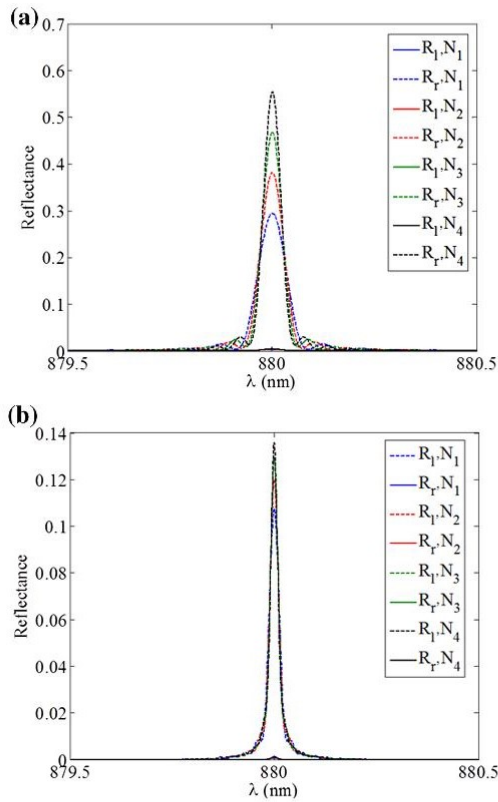


**Fig. 6** Reflectance spectra for (a) first- and (b) third-order Bragg gratings. The number of unit cells is  $N_1 = 10,000$ ,  $N_2 = 12,000$ ,  $N_3 = 14,000$ ,  $N_4 = 16,000$

Figure 6 shows the reflectance responses of first ( $O = 1$ )- and third ( $O = 3$ )-order gratings as the number of unit cells varies from 10,000 to 16,000.

As the number of unit cells increases, the reflectance peaks increase as expected. The third-order gratings have a sharper peak, but a maximum reflectance that is lower than first-order gratings due to the greater propagation loss in a longer structure. In terms of fabrication, third-order gratings are more convenient as the pitch and the length of Sects. 1, 2, 3 and 4 are  $3\times$  longer.

The contrast ratio ( $C$ ) is defined to measure the level of non-reciprocity and is given as:

$$C = \frac{|R_r - R_l|}{|R_r + R_l|} \quad (2)$$

where  $R_r$  and  $R_l$  are the right-incident and left-incident reflectance, respectively. The contrast ratio obtained is

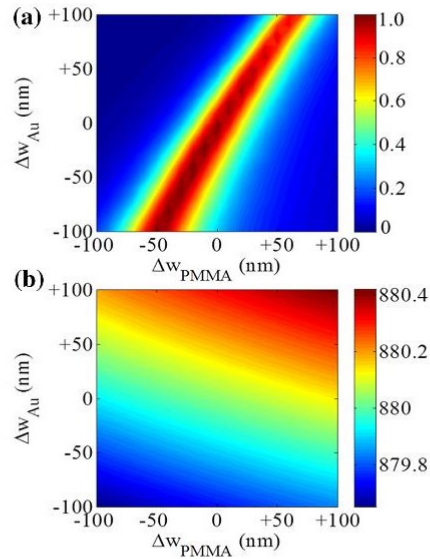


**Fig. 7** (a) Contrast ratio and (b) Bragg wavelength vs. deviations in Au and PMMA widths of all four sections in a unit cell

98 % for the designed gratings regardless of their order or number of unit cells.

### 3 Design robustness

In order to consider design robustness, which matters for fabrication, we assumed equal drift on the dimensions of all four sections and observed how the contrast ratio and Bragg wavelength vary. For instance, the width of the Au stripe in all four sections could be larger by 50 nm due to overexposure of resist. The contrast ratio was computed as a function of deviations in the Au and PMMA widths by up to  $\pm 100$  nm from their nominal values. Figure 7a, b plots the contrast ratio and the Bragg wavelength vs. the width deviations  $\Delta w_{Au}$  and  $\Delta w_{PMMA}$ .

As Fig. 7a shows if  $\Delta w_{Au}$  and  $\Delta w_{PMMA}$  decrease or increase together, the contrast ratio remains high, whereas it drops significantly for other combinations of deviations. From Fig. 7b, we note that the Bragg wavelength remains essentially constant over such deviations. This is not surprising because the pitch remains constant—only  $n_{ave}$  is modified by width deviations. Indeed, the PT symmetry-broken Bragg is sensitive to dimensions; however, as observed from Fig. 7, the contrast ratio remains reasonably tolerant to errors in width.

#### 4 Summary

A PT symmetry-broken Bragg grating concept operating with LRSPPs was proposed and modelled. The reflectance response was computed for first- and third-order gratings. The contrast ratio was used to evaluate the asymmetric performance of the Braggs and their tolerance to some fabrication imperfections considered. Contrast ratios nearing 1 with a single-sided reflectance approaching 0.6 are possible using a step-in-width Au stripe and an overlaid step-in-width active PMMA stripe providing about  $70 \text{ cm}^{-1}$  of material gain.

#### References

1. C.M. Bender, S. Boettcher, *Phys. Rev. Lett.* **80**, 5243–5246 (1998)
2. G. Levai, M. Znojil, *J. Phys. Math. Gen.* **33**, 7165–7180 (2000)
3. L. Feng, Y.L. Xu, W.S. Fegadolli, M.-H. Lu, J.E.B. Oliveira, V.R. Almedida, Y.F. Chen, A. Scherer, *Nat. Mater.* **12**, 108–113 (2013)
4. X. Yin, X. Zhang, *Nat. Mater.* **12**, 175–177 (2013)
5. A. Regensburger, Ch. Bersch, M.A. Miri, G. Onishchukov, D.N. Christodoulides, U. Peschel, *Nature* **488**, 167–171 (2012)
6. H. Alaeian, J.A. Dionne, *Phys. Rev. A* **89**, 033829 (2014)
7. M. Kulishov, B. Kress, *Opt. Express* **21**, 22327–22337 (2013)
8. H. Ramezani, T. Kottos, R. El-Ganainy, D.N. Christodoulides, *Phys. Rev. A* **82**, 043803 (2010)
9. H.E. Reuter, K.G. Makris, R. El-Ganainy, D.N. Christodoulides, M. Segev, D. Kip, *Nat. Phys.* **6**, 192–195 (2010)
10. K.G. Makris, R. El-Ganainy, D.N. Christodoulides, Z.H. Musslimani, *Phys. Rev. Lett.* **100**, 103904 (2008)
11. E.M. Graefe, H.F. Jones, *Phys. Rev. A* **84**, 013818 (2011)
12. M. Kulishov, J.M. Laniel, N. B elanger, J. Aza na, D.V. Plant, *Opt. Express* **13**, 3068–3078 (2005)
13. L. Feng, X. Zhu, S. Yang, H. Zhu, P. Zhang, X. Yin, Y. Wang, X. Zhang, *Opt. Express* **22**, 1760–1767 (2014)
14. M. Kulishov, J.M. Laniel, N. B elanger, D.V. Plant, *Opt. Express* **13**, 3567–3578 (2005)
15. E.K. Keshmarzi, R.N. Tait, P. Berini, *App. Phys. Lett.* **105**, 191110 (2014)
16. E.K. Keshmarzi, R.N. Tait, P. Berini, *Opt. Express* **22**, 12452–12460 (2014)
17. S. Jett -Charbonneau, P. Berini, *J. Opt. Soc. Am. A* **23**, 1757–1767 (2006)
18. S. Jett -Charbonneau, R. Charbonneau, N. Lahoud, G. Mattiussi, P. Berini, *Opt. Express* **13**, 4674–4682 (2005)
19. S. Jett -Charbonneau, P. Berini, *IEEE J. Quantum Electron* **41**, 1480–1491 (2005)
20. P. Yeh, *Optical Waves in Layered Media* (Wiley, Toronto, 1988)

## **5.4 Unidirectional PT symmetry breaking Bragg grating, remarks on group and energy velocities**

### **5.4.1 Summary**

A comprehensive literature review on PT symmetric optical systems is provided in this section. Moreover, two PT symmetry Bragg gratings operating in LRSPP structure based on step-in-width metal stripes, and dielectric-loaded metal stripes are proposed [12]. Using modal and TMM computations, asymmetric reflectance is demonstrated in these Bragg gratings. The conditions for switching the PT symmetric grating to exist in the unbroken state, at the breaking threshold, and in the broken state are discussed. Additionally, pulse reshaping and energy transport in generic gratings as well as proposed PT symmetric Bragg gratings are investigated. It is shown that unlike conventional Bragg gratings, PT symmetric Bragg gratings at the exceptional point produce no dispersion in group or energy velocity. Also the group delay dispersion in broken and unbroken states is inverted. These properties make these gratings suitable for novel applications in optical switching and distortion-less pulse transfer.

### **5.4.2 Contribution**

Choloong Hahn and I reviewed the literature. He and I had proposed and designed PT symmetric Bragg gratings based on dielectric-loaded metal stripes, and step-in-width metal stripes respectively. We formulated the group and energy velocities for generic Bragg gratings, and each of us applied the theoretical model to our corresponding PT symmetric Bragg gratings. We both interpreted the results and made conclusions. I wrote the manuscript. Dr. Tait, Dr. Berini and Hahn's supervisors contributed to the results' interpretation and manuscript revision.

## 5.4.3 Article

The published article follows verbatim.

4600712

IEEE JOURNAL OF SELECTED TOPICS IN QUANTUM ELECTRONICS, VOL. 22, NO. 5, SEPTEMBER/OCTOBER 2016

# Unidirectional Bragg Gratings Using Parity-Time Symmetry Breaking in Plasmonic Systems

Choloong Hahn, Elham Karami Keshmarzi, Seok Ho Song, Cha Hwan Oh, *Member, IEEE*,  
R. Niall Tait, and Pierre Berini, *Fellow, IEEE*

(Invited Paper)

**Abstract**—Optical systems following concepts of parity-time (PT) symmetry have attracted significant attention because of their extraordinary behavior such as unidirectional reflectance or power oscillation. PT symmetric optical systems are realized by judiciously manipulating the complex refractive index to produce even- and odd-symmetric distributions for the real and imaginary indices, respectively. We propose two PT symmetric Bragg gratings based on step-in-width metal stripes and dielectric-loaded metal stripes operating with long-range surface plasmon polaritons. The gratings are designed to operate near 880 nm because optical gain can be conveniently provided by IR140-doped PMMA. Asymmetric reflectance is predicted in the proposed gratings based on modal and transfer matrix method computations. Moreover, we analyzed pulse reshaping and energy transport in generic gratings, and in the proposed plasmonic gratings, in terms of group and energy velocities. It is found that the group and energy velocities are dispersionless at the PT symmetry breaking point. Also, the group velocity dispersion can be inverted by changing the PT symmetric state from broken to unbroken or vice versa. Our designs are practical because a large left-right asymmetric reflectance contrast is produced for a wide range of physical dimensions. The proposed gratings are suitable as on-chip devices for optical processing providing new functionality such as switching and controlling the time delay of a data pulse without distortion.

**Index Terms**—Bragg gratings, energy velocity, exceptional point, group velocity, parity-time symmetry, plasmonics.

## I. INTRODUCTION

IT IS well-known in quantum mechanics that the Hamiltonian of a system needs to be Hermitian in order to provide an entirely real set of eigenvalues as observable quantities. However, it was clearly shown by Bender and Boettcher in 1998 that a wide class of non-Hermitian systems could also have real

eigenvalues provided that they respect the parity-time (PT) symmetry condition and the corresponding Hamiltonians share the same set of eigenfunctions [1]. Hamiltonians with a complex potential  $V$  as a function of position  $\mathbf{r}$  obeying the condition  $V(\mathbf{r}) = V^*(-\mathbf{r})$ , with  $*$  denoting the complex conjugate, are PT symmetric. By forming an analogy between the corresponding equations of quantum mechanics and optics it is easy to show that the refractive index plays the role of the potential in optics. Completing the analogy, PT symmetry implies that the complex refractive index satisfy  $n(\mathbf{r}) = n^*(-\mathbf{r})$ . In other words, the real index distribution is invariant under spatial inversion whereas the gain and loss simultaneously interchange [2], [3].

Synthetic optical materials such as photonic crystals [4] and metamaterials [5], created by engineering the real part of refractive index, have been widely studied and have found novel optical applications. Recently, new artificial materials based on the concept of PT symmetry, including real and imaginary refractive indices, have been investigated. PT symmetry in optics has attracted significant attention because it is a new and versatile approach to realize and observe evolution of PT phases. Also, conceptually, it leads to components that offer extraordinary optical functions, such as unidirectional energy transport in directional waveguide coupler systems [3], asymmetric reflectance in waveguide Bragg gratings [6], and Bloch power oscillation in time-domain PT symmetric optical lattices [7]. Most of these phenomena are observed near the spontaneous PT symmetry breaking point (the so-called exceptional point) where PT symmetry breaks down abruptly and eigenvalues merge and become degenerate. The optical properties of structures at the breaking point are studied by many due to the extraordinary behavior observed there, but some research is also conducted on the adiabatic evolution of complex potentials near the breaking point without crossing the threshold [8].

As the above condition on the refractive index distribution implies, a balanced amount of gain and loss is required in the system in order for it to be PT symmetric. However, this is not a sufficient condition for PT symmetry. Indeed, it is possible to produce a PT symmetric optical system (based on gauge transformation) such that only loss exists and is modulated in the material [9]. Plasmonic systems with intrinsic loss are advantageous when applied to the PT symmetric optical systems [10]. Moreover, plasmonic systems could be combined with gain [11], leading to practical PT symmetric designs.

In this paper, we review the concepts behind PT symmetric waveguide Bragg gratings, and, comprehensively, the literature

Manuscript received November 30, 2015; revised January 13, 2016; accepted January 14, 2016. Date of publication February 11, 2016; date of current version March 21, 2016. This work was supported in part by the Global Frontier Program through the National Research Foundation of Korea funded by the Ministry of Science, ICT & Future Planning (No. NRF-2014M3A6B3063708), and by the Natural Science and Engineering Research Council of Canada.

C. Hahn, S. H. Song, and C. H. Oh are with the Physics Department, Hanyang University, Seoul 133-791, Korea (e-mail: choloong.hahn@gmail.com; shsong@hanyang.ac.kr; choh@hanyang.ac.kr).

E. K. Keshmarzi and R. N. Tait are with the Electronics Department, Carleton University, Ottawa, ON K1S 5B6, Canada (e-mail: ekeshma@doe.carleton.ca; niall@doe.carleton.ca).

P. Berini is with the School of Electrical Engineering and Computer Science, Department of Physics, and the Center for Research in Photonics, University of Ottawa, Ottawa, ON K1N 6N5, Canada (e-mail: berini@eecs.uottawa.ca).

Color versions of one or more of the figures in this paper are available online at <http://ieeexplore.ieee.org>.

Digital Object Identifier 10.1109/JSTQE.2016.2519825

on this topic. We also discuss in detail two PT symmetric Bragg gratings (based on long-range surface plasmon polaritons—LRSPPs [12]), operating near the exceptional point [13], [14]. We previously discussed how these structures provide asymmetric reflectance, in contrast to other LRSP Bragg gratings using only real index modulation [15]. Designs of PT symmetric Bragg gratings follow a similar approach except that the required imaginary index modulation is introduced by periodically doping a polymer gain cladding [13] or by altering the supermode character of LRSP modes [14]. Group and energy velocities have not yet been considered or evaluated for such structures—we recall the general definitions of these quantities from which we analyze pulse propagation and energy transport through a generic PT symmetric Bragg grating and through specific implementations based on LRSPPs.

## II. PARITY-TIME SYMMETRIC OPTICAL SYSTEMS

Some optical properties pertaining to PT symmetric materials or devices, such as asymmetric reflection in non-uniform linear Bragg gratings [16], nonreciprocal diffraction [17], irreversible coupling [18], unidirectional coupling [19], unidirectional Bragg gratings [2], and ring resonators based on asymmetric transmission [20], were reported in the late 1990s and early 2000s. Although no explicit connection to PT symmetry was made in these works, the properties observed are consistent with concepts of PT symmetry. The very first report to our knowledge which considered the physical realization of a PT symmetric potential in a planar slab waveguide was by Ruschhaupt *et al.* [21], who showed that Maxwell equations for an electromagnetic wave propagating along a planar slab waveguide filled with contiguous gain and loss regions can be approximated in a parameter range by a Schrödinger equation with a PT symmetric scattering potential. Later, El-Ganainy and Makris [22] developed a coupled-mode theory appropriate for PT symmetric optical systems, and applied their method to a PT symmetric waveguide coupler and an infinite array of PT symmetric potentials. These researchers also systematically investigated one- and two-dimensional PT symmetric optical lattices [23], [24]. Some peculiarities of diffraction dynamics arising in PT lattices, including band-merging, double-refraction, non-reciprocity, bi-orthogonality, power oscillation and phase dislocation were analytically and numerically examined.

Since it was shown that complex PT symmetric potentials are realizable within the realm of optics, numerous optical structures have been suggested and studied theoretically and experimentally. As our focus in this paper is on PT symmetric waveguide Bragg gratings, we give an expansive review of this particular concept. Related PT symmetric optical structures are also briefly reviewed at the end of this section.

### A. Waveguide Type Bragg Gratings

Kulishov *et al.* [2] reported a waveguide Bragg grating which combined balanced modulations of real refractive index and loss/gain allowing asymmetric mode coupling within the structure. The structure was analyzed using coupled-mode theory and the spectral performance and design constraints were derived.

This study also revealed that structure exhibits strong amplification at the resonance wavelength even with zero net gain in the waveguide, while simultaneously providing higher wavelength selectivity than the corresponding real-index modulated grating. In the paper by Lin *et al.* [25], unidirectional invisibility at the spontaneous PT symmetry breaking point of a PT symmetric Bragg structure was reported. It was shown that for operation at the PT symmetric breaking point, when light is incident on one side of the structure, the system is reflectionless at frequencies near the Bragg resonance, whereas the reflectance from the other side of the structure is enhanced. Moreover, in this regime, the transmission phase vanishes, which is a necessary condition for evading detectability. They also found that these properties persist even in the presence of Kerr nonlinearities. PT symmetric Dirac–Kronig–Penney (DKP) Hamiltonians were investigated in [26], and their physical realization was considered through propagation and scattering of light waves in engineered superstructure fiber Bragg gratings which comprise balanced optical gain and loss regions. Kulishov *et al.* proposed a new class of distributed Bragg reflector (DBR) laser structures using PT symmetric Bragg gratings with unidirectional reflectance [27], composed of two concatenated unidirectional Bragg gratings with their non-reflective ends oriented outwards from the cavity. It was shown that these laser structures inherently support only one lasing mode. A passive PT symmetric Bragg waveguide was realized experimentally by Feng *et al.* [28] using absorptive media in the Si-on-insulator platform. An 800-nm-wide and 220-nm-thick Si waveguide with a periodic modulation of its permittivity was embedded in SiO<sub>2</sub>. Theoretical analysis suggested unidirectional invisibility at the PT exceptional point. In the experiments, the reflectance in the forward direction was about 7.5 dB stronger than that in the backward direction, indicating asymmetric optical performance owing to the PT symmetry phase transition over a broad band of telecom wavelengths from 1520 to 1580 nm.

Phang *et al.* suggested the use of a PT symmetric waveguide Bragg grating as an optical switch and analyzed the switching response in the time domain using transmission line modeling [29]. For this purpose the original Bragg grating with uniform loss is turned in to a PT symmetric Bragg grating by suddenly pumping the structure while dissipative regions are masked. It was shown that the switching action occurs in 0.4–1.4 ps, and the on/off ratio of the transmitted signal’s amplitude is of the order of 10<sup>3</sup>. The minimum switching time and maximum on/off ratio was obtained at the PT symmetry breaking point. Xu *et al.* modeled a PT symmetric Si waveguide Bragg grating using coupled-mode theory and the FDTD method [30]. The results showed the expected asymmetric reflectivity. Moreover, they considered a DBR cavity structure using PT symmetric Si waveguide Bragg gratings. The third-order nonlinearity of Si in the cavity was taken into account because of the high fields induced therein by the PT symmetric gratings. In addition to the asymmetric forward/backward reflection, the transmission response was also found to be asymmetric due to nonlinearity in the cavity. The transmission of the nonlinear PT symmetric DBR cavity at certain wavelengths was highly unidirectional producing a contrast ratio of almost unity. Lupu *et al.* suggested

a new class of directional couplers based on four-wave interaction in a PT symmetric Bragg-grating-assisted structure [31]. In the proposed structure a uniform passive waveguide and a PT symmetric Bragg grating waveguide are coupled as a four port device, useful for switching and modulating applications. The device operation is based on modifying the dispersion properties of the PT symmetric Bragg grating by adjusting its gain level in order to control phase matching between the two waveguides. It is impossible to achieve phase matching using conventional Bragg gratings because they have a bandgap near the Bragg wavelength; however, the bandgap disappears in a properly gain modulated PT symmetric Bragg operating at the exceptional point. The switching action also occurs with imperfect PT symmetric or PT symmetry broken Bragg gratings which are more practical.

Zhu *et al.* analyzed the scattering in a rectangular PT symmetric Bragg grating of finite length [32]. Via numerical modeling, they showed that asymmetric reflection occurred periodically with increasing number of unit cells. The proposed Bragg was bi-directionally transparent (unity transmittance) at reflectance minima, which occur for a specific number of unit cells due to the discontinuity at the interfaces of grating sections. Unidirectional response and field localization due to the PT symmetric arrangement of the grating sections were also discussed. Yan *et al.* reported a fabrication method for sinusoidal PT symmetric gratings with arbitrary complex index modulation [33]. This method is based on simultaneous vapor-deposition of a non-absorbing high index host ( $\text{Alq}_3$ ), a non-absorbing low index dopant (Teflon AF 1600), and an absorbing dopant (DCM). By co-deposition and continuously varying the individual rates, the modulation amplitude of the real (proportional to the low-index dopant concentration) and imaginary gratings (proportional to the absorbing dopant concentration) are independently controlled throughout the film's thickness, producing a contrast ratio of about 0.9 at the PT symmetry breaking point. Kesharzi *et al.* proposed a PT symmetric Bragg grating based on an LRSPP waveguide structure [13]. The real and imaginary index modulations were produced by stepping the width of a Ag stripe, and alternating the deposition of a doped and undoped PMMA top cladding. The phase difference between the real and imaginary index modulations at the exceptional point is  $90^\circ$ . The proposed grating promises a contrast ratio of  $\sim 1$  assuming a material gain of about  $70 \text{ cm}^{-1}$ . (This structure will be discussed in greater detail in Section IV.) Jia *et al.* suggested a fabrication method for a sinusoidal PT symmetric grating using angled deposition of an absorptive material [34]. The sinusoidal real grating was fabricated using interference lithography and the absorptive material was deposited at an oblique angle. In this way the sinusoidal modal effective index distribution having the desired phase shift is achieved through the local thickness of both materials. The Littrow diffraction was measured and a contrast ratio of  $\sim 0.9$  was obtained at the PT symmetry breaking point. Hahn *et al.* designed a PT symmetric Bragg grating based on the LRSPP waveguide structure [14]. The required complex index modulation was obtained by modulating the width of the top PMMA cladding about the width where the LRSPP couples to an antisymmetric plasmon mode.

Two pairs of suitable waveguide segments were selected and arranged judiciously within the grating's unit cell. The magnitude of real and imaginary index modulation is controlled by tuning the thickness of the Ag stripe and by introducing gain in the PMMA claddings. (This structure will be discussed in greater detail in Section IV.) Nixon *et al.* studied light propagation in a PT symmetric waveguide using multiscale perturbation theory [35]. They showed that the cubic nonlinearity does not alter the exponential growth or decay of the mode in non-PT-symmetric Bragg gratings. However, continuous families of longitudinally periodic and transversely quasi-localized nonlinear modes, below and above the PT symmetry breaking point, were observed. It was shown that the low-amplitude incident electric field initially grows exponentially and eventually develops nonlinear periodic states.

### B. Other PT Symmetric Optical Structures

The exceptional point in a PT symmetric directional coupler comprising two waveguides with an antisymmetric gain/loss profile was visualized as a branch point in the paper by Klaiman *et al.* [36]. Čtyroký *et al.* investigated the power transmission properties of TE and TM modes in a two-mode waveguide and a directional coupler with an asymmetric gain/loss profile [37]. They showed that the total power transmitted in a coupler with balanced loss and gain is not constant along the coupler, and that above a critical gain/loss balance, power predominantly resides in the gain section and grows exponentially with coupling length. In experiments by Rüter *et al.* [3], PT symmetry breaking and violation of left-right symmetry in an active PT symmetric coupled system, were investigated using Fe-doped  $\text{LiNbO}_3$  comprising active and passive waveguides. It was observed that above some threshold gain, light is predominantly guided in the active channel regardless of where the input signal is applied. PT symmetric directional couplers based on hybrid dielectric-plasmonic waveguides were investigated by Benisty *et al.* [10] revealing that near a PT symmetry exceptional point a small modulation of gain/loss results in a large change in the propagation characteristics of the supermodes. In a later work by Lupu *et al.* [38], plasmonic-based PT symmetric directional couplers are proposed for optical switching, emphasizing on the positive role of losses in plasmonic waveguides, leading to lower required gain for switching.

A five layer plasmonic waveguide composed of metallic layers separated by dielectric media containing either loss or gain in equal quantities was investigated by Alaeian *et al.* [39]. The modal behavior of the waveguide was studied as a function of non-Hermiticity with particular attention paid to the eigenstates as they coalesce and evolve at exceptional points. The authors suggest use of PT symmetric plasmonic devices as nanophotonic modulators, which near the exceptional point, will exhibit significant modal transformations, giving rise to fast, sensitive and low-power all-optical modulators. The issue of controlling gain/loss while maintaining the symmetry of the real index in directional couplers is addressed by Choi *et al.* [40] where they propose a PT symmetric coupled-waveguide structure based on a double-slab SPP waveguide.

Unidirectional invisibility near the exceptional point in a large-scale PT symmetric temporal lattice was experimentally demonstrated in [7]. The entire band structure of this lattice was probed by simultaneously exciting all bands with a single pulse. Evolution of exceptional points as well as band merging effects and power oscillation were observed in the experiment agreeing well with theory. PT symmetry breaking was observed in an entirely passive dual system comprising two coupled ridge waveguides in a multilayered  $\text{Al}_x\text{Ga}_{1-x}\text{As}$  heterostructure [9]. Loss-enhanced transmission was observed as a direct manifestation of PT non-Hermiticity.

A ring cavity laser based on PT symmetry breaking was introduced by Feng *et al.* [41] which exhibits intrinsic single-mode lasing regardless of the gain spectral bandwidth. In an experimental work by Hodaei *et al.* [42] a PT symmetric coupled-microring laser was demonstrated, where by selectively breaking PT symmetry the maximum attainable output power in the desired mode was systematically enhanced.

A nanoscale PT symmetric plasmonic modulator was proposed by Baum *et al.* [43] which operates based on coherent absorption and amplification. Huang *et al.* [44] designed a PT symmetric plasmonic waveguide cavity system, consisting of two metal-dielectric-metal stub resonators side-coupled to a metal-dielectric-metal waveguide forming an exceptional point enabling unidirectional reflection at telecom wavelengths. Longhi *et al.* [45] introduced the idea of a PT symmetric laser-absorber and showed that an optical medium satisfying the PT symmetry condition can behave simultaneously as a laser oscillator, emitting outgoing coherent waves, and as a coherent perfect absorber, fully absorbing incoming coherent waves with appropriate amplitudes and phases.

### III. PT SYMMETRIC BRAGG GRATINGS

In this section we recall the complex optical potential for a one-dimensional PT symmetric Bragg grating and specify the PT symmetric phases based on a balance factor. Then we recall general definitions of group and energy velocity from which we analyze pulse propagation and energy transport through the Bragg grating.

#### A. Complex Optical Potential in PT Symmetric Bragg Grating

We focus on PT symmetric Bragg gratings operating near the exceptional point. We express the PT symmetric refractive index distribution along the Bragg reflector's length ( $z$ ) in a basic sinusoidal form as [2], [25], [28]:

$$n(z) = n_{\text{ave}} + \Delta n_{\text{R}} \cos\left(\frac{2\pi}{\Lambda} z\right) + i\Delta n_{\text{I}} \cos\left(\frac{2\pi}{\Lambda} z - \delta\right), \quad (1)$$

where,  $n_{\text{ave}}$  is the average complex index,  $\Delta n_{\text{R}}$  and  $\Delta n_{\text{I}}$  are the modulation amplitudes of the real and imaginary indices, respectively,  $\delta$  is the phase difference between the real and imaginary index modulations, and  $\Lambda$  is the spatial periodicity. Now the complex potential can be characterized in terms of  $\delta$  and the balance factor, which is defined as  $\gamma \equiv \Delta n_{\text{I}}/\Delta n_{\text{R}}$ . Based on our discussion in Section I, a PT symmetric Bragg

reflector is obtained by setting  $\delta = \pm\pi/2$ . The balance factor  $\gamma$  measures the system's non-Hermiticity level and determines the PT symmetric state by specifying the eigenvalues of the corresponding Hamiltonian. For  $\gamma < 1$ , the Bragg reflector is in an exact PT symmetric state (so-called unbroken PT symmetry), where the eigenvalues are all purely real even though both optical gain and loss exist in the system. Spontaneous PT symmetry breaking occurs at  $\gamma = 1$ , where the real and imaginary index modulations are perfectly balanced. Here, eigenvalues merge and become degenerate. Further increasing  $\gamma$  to  $\gamma > 1$  shifts the system to a broken PT symmetric state where it is still PT symmetric but the eigenstates are not, and the eigenvalues form complex conjugate pairs [1]–[3], [28].

Although a PT symmetric Bragg grating is defined from (1), it is not always easy to implement a structure in that form. It is important to note that any one-dimensional periodic refractive index can be approximated by its first-order Fourier representation to resemble (1). Here, we are specifically dealing with square perturbations of refractive index in which both the real and imaginary refractive index have the same period  $\Lambda$ , but a  $\Lambda/4$  spatial shift between them, satisfying the requirement for PT symmetry. In this configuration we can still define the balance factor as stated above and specify regions corresponding to unbroken, exceptional point and broken states by the step difference in the real and imaginary indices.

#### B. Group and Energy Velocity

Typically periodic structures exhibit group velocity dispersion with wavelength, so a pulse propagating through will experience distortion and dispersion. The superluminal group velocity of Bragg gratings has been widely studied. Longhi *et al.* have reported superluminal pulse reflection in the sense that the peak of reflected pulse has left the input facet before the peak of incident pulse enters the input facet of a grating structure [46]. However, superluminal group velocities do not violate Einstein causality because they are not simply related to the velocity of energy transport in such structures.

It has been shown theoretically [2], [25] that PT symmetric Bragg gratings produce dispersionless group velocity at the PT symmetry breaking point, and Regensburger *et al.* have shown experimentally that superluminal pulse propagation occurs in a PT symmetric temporal lattice, implemented as a fiber-coupled system, operating in a PT symmetry broken state [7].

The group and energy velocities are identical for isotropic, nondispersive, lossless media [47], however, they are not the same in Bragg gratings. The group velocity of a Bragg grating is superluminal near the Bragg wavelength but the energy velocity is always subluminal, respecting causality [48]. For a clearer understanding of pulse propagation and energy transport we consider an ideal PT symmetric Bragg grating which has four step indices per period, as detailed in the bottom left of Fig. 1. In this case the PT symmetry breaking point occurs at  $\Delta n_{\text{I}} = 5 \times 10^{-4}$  because we set  $\Delta n_{\text{R}} = 5 \times 10^{-4}$ . For Bragg gratings, the group velocity of the grating is obtained as

$$v_g(\lambda) = L_G/\tau_g(\lambda), \quad (2)$$

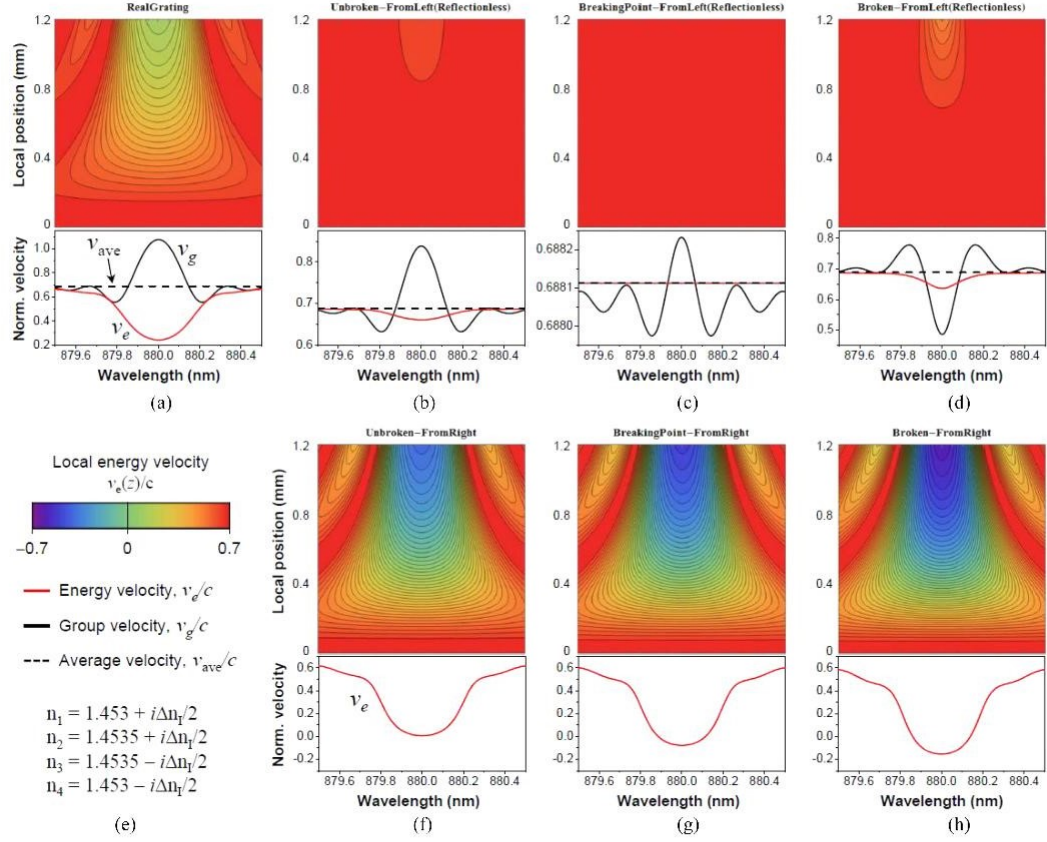


Fig. 1. Calculated local ( $v_e(z)$ , contour plots) and global energy ( $v_e$ , black solid curves) velocities, and group velocities ( $v_g$ , red curves). (a) Conventional real index grating ( $\Delta n_I = 0$ ), and for unbroken, breaking point, and broken PT symmetric gratings with incidence from the left side (b-d) and from the right side (e-g). The dashed line indicates the averaged index velocity. All velocities are normalized to the vacuum speed of light.

where  $\lambda$  is the wavelength,  $L_G$  is the physical length of whole grating, and  $\tau_g$  is the group delay for transmission through the grating which can be written as

$$\tau_g(\lambda) = -\frac{\lambda^2}{2\pi c_0} \frac{\partial \phi}{\partial \lambda}. \quad (3)$$

Here,  $c_0$  is the speed of light in vacuum, and  $\phi$  is the phase of the transmission coefficient. Also, from formal definition, the magnitude of local energy transport velocity,  $v_e(z, \lambda)$ , can be written as [48]:

$$v_e(z, \lambda) = \frac{\bar{\mathbf{S}}(z, \lambda) \cdot \hat{a}_z}{\bar{w}(z, \lambda)}, \quad (4)$$

where,  $z$  is the propagation axis of the Bragg grating,  $\hat{a}_z$  is a unit vector in the propagation direction,  $\bar{\mathbf{S}}(z, \lambda) = \text{Re}[\mathbf{E}(z, \lambda) \times \mathbf{H}^*(z, \lambda)]/2$  is the time-averaged local Poynting vector, and  $\bar{w}(z, \lambda) = [\mathbf{E}(z, \lambda) \cdot \mathbf{D}^*(z, \lambda) + \mathbf{B}(z, \lambda) \cdot \mathbf{H}^*(z, \lambda)]/2$  is the time-averaged electromagnetic

energy density. The electric field inside the grating can be written as  $\mathbf{E}(z, \lambda) = \mathbf{E}^+(z, \lambda) + \mathbf{E}^-(z, \lambda)$ , as a superposition of forward and backward propagating fields. To extend the local energy velocity to a global quantity, we take the average of local energy velocities over for whole length of the grating:

$$v_e(\lambda) = \frac{\int_0^{L_G} v_e(z, \lambda) dz}{L_G}. \quad (5)$$

Since a PT symmetric Bragg grating is characterized by the balance factor  $\gamma$  as unbroken ( $\gamma < 1$ ) and broken ( $\gamma > 1$ ) states, we considered four cases to compare, including a conventional real index grating ( $\Delta n_I = 0$ ), and PT symmetric gratings in the unbroken state ( $\Delta n_I = 4 \times 10^{-4}$ ), at the breaking point ( $\Delta n_I = 5 \times 10^{-4}$ ), and in the broken state ( $\Delta n_I = 6 \times 10^{-4}$ ). The velocities calculated by (2) and (5) for these cases are shown in Fig. 1, normalized to the vacuum speed of light. The black curves in Fig. 1 are  $v_g$ , the red curves are  $v_e$ , and the dashed lines are the light propagation velocity in the uniform medium

with averaged index ( $v_{ave}$ ). For a clearer understanding, we also present  $v_e(z)$  versus wavelength and local position. We used the transfer matrix method (TMM) [49] for obtaining  $\varphi$  and  $\mathbf{E}$ , 4000 periods were considered with a Bragg wavelength of  $\lambda_B = 880$  nm. The computed local energy velocity  $v_e(z)$  is presented as contour plots in Fig. 1 and the global velocities ( $v_e$ ,  $v_g$ ,  $v_{ave}$ ) are presented at the bottom of each contour plots. Fig. 1(a) corresponds to a conventional real index grating, whereas Fig. 1(b)–(d) show the velocities for left-side incidence and Fig. 1(e)–(g) for right-side incidence for the PT symmetric Bragg at 3 different states. Note that the energy velocities for left- and right-incident waves are different. This is due to the asymmetric reflection of these waves. However, because the transmission for left- and right-incident waves is identical, the group velocities are also identical, so we plot  $v_g$  only for the left-incident case.

The contours in Fig. 1 reveal interesting points. Firstly in Fig. 1(a),  $v_e(1.2$  mm) at  $\lambda = 880$  nm tends to zero implying the formation of standing waves at the Bragg wavelength due to high grating reflectance. However, for the reflectionless side of the PT symmetric Braggs (see Fig. 1(b)–(d))  $v_e$  does not show much variation and is indeed very similar to  $v_{ave}$ . This is because there is not much backward coupling in this case, which implies that the propagating wave is unaffected by the index modulation. For the right incident cases though (see Fig. 1(e)–(g)), the  $v_e$  distribution resembles that of the conventional Bragg (see Fig. 1(a)). This is due to the forward to backward coupling in these cases. But interestingly we also observe a negative  $v_e$  which occurs due to the reflectance greater than 1, or amplified reflectance in PT symmetric Braggs, which alters the direction of energy transport.

The group velocity of the real grating is greater than  $v_{ave}$  around  $\lambda_B$ , which implies that the grating is in the superluminal regime. However, this does not violate causality because  $v_e$  remains subluminal over the whole wavelength range as predicted in [48]. By increasing  $\Delta n_I$  to  $4 \times 10^{-4}$ , thus turning the grating to PT symmetric grating,  $v_g$  and  $v_e$  for left-incidence retain a similar shape to the real grating as shown in Fig. 1(b). This is because the grating is in the unbroken state which yields pure real eigenvalues, so such gratings produce similarly shaped velocity curves even though there is gain/loss modulation. The modulation ranges of the velocities are smaller for the PT symmetric grating due to the reduced reflection. The velocities for left-incidence become constant as the grating approaches the PT symmetry breaking point ( $\Delta n_I = 5 \times 10^{-4}$ ) because there is no reflection at this point to alter the velocities. As shown in Fig. 1(c),  $v_e$  is perfectly flat over the wavelength range considered, and the fluctuation in  $v_g$  is negligibly small (note the vertical scale change) so we can assume that  $v_g$  is also constant at the breaking point. This means that the incident light propagates through the grating without experiencing the real and imaginary index modulations. When  $\Delta n_I$  exceed  $5 \times 10^{-4}$ , the grating enters the broken state;  $v_g$  and  $v_e$  in this state are plotted in Fig. 1(d), and  $v_e$  is again subluminal, as in the unbroken state. Therefore, in all states, energy transport through the grating is slower than  $v_{ave}$  which is consistent with the subluminal regime and respects causality. However,  $v_g$  in the broken state has an in-

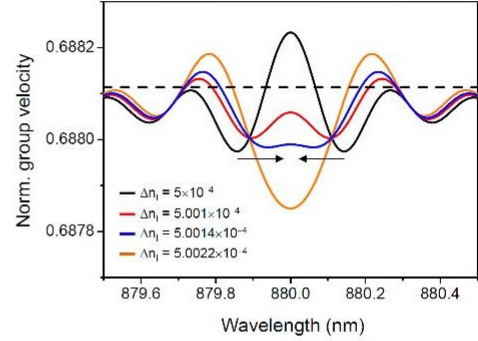


Fig. 2. Inversion of the group velocity response near the PT symmetry breaking point. The colors denote different  $\Delta n_I$  and the horizontal dashed line is as in Fig. 1. The black arrows indicate the motion of the dips occurring at the band edges.

verted shape compared to the unbroken state, yet they have same energy transport velocities. This could give one more degree of freedom for device applications pertaining to pulse reshaping.

The group velocities of the conventional real grating, and of the unbroken PT symmetric grating, peak at  $\lambda_B$  and drop on both sides of  $\lambda_B$ , in correspondence with the edges of the (energy) bandgap. Increasing  $\gamma$  from the unbroken to the broken state, the peak decreases and the dips move to the Bragg wavelength, as the band edges merge, leading to inversion of the group velocity response curve as shown in Fig. 2. The black curve is the calculated group velocity at the PT symmetry breaking point and  $\Delta n_I$  is increased in sequence (red, blue and orange curves). The group velocity is completely inverted by increasing  $\Delta n_I$  by only 0.04% from the breaking point. Group velocity inversion (compare Fig. 1(b) with Fig. 1(d)) could be useful in devices that control the group velocity.

#### IV. PLASMONIC PT SYMMETRIC BRAGG GRATINGS

##### A. Design of PT Symmetric Bragg Gratings

Plasmonic systems present good platforms to realize PT symmetric structures because losses in plasmonic systems are intrinsic and precisely controllable by manipulating the geometry. Here we propose two Bragg grating structures satisfying PT symmetry conditions based on plasmonic waveguide structures supporting LRSPP mode. 3D and top view sketches of a period of the proposed grating structures are schematically illustrated in Fig. 3, with two waveguiding sections connected at the both ends of the gratings. Pink colored regions represent undoped PMMA layers and purple colored regions are IR140-doped PMMA layers. IR140 is a well-studied commercial dye molecule which absorbs light around 810 nm and provides optical gain around 880 nm. It has been reported that IR140-doped PMMA layers provide  $\sim 70$  cm<sup>-1</sup> of optical TM gain under optical pumping from the top with 10 ns, 500 MW/cm<sup>2</sup>, 810 nm pulses [50]. So the gratings are designed to operate in the near-infrared at  $\lambda_B = 880$  nm.

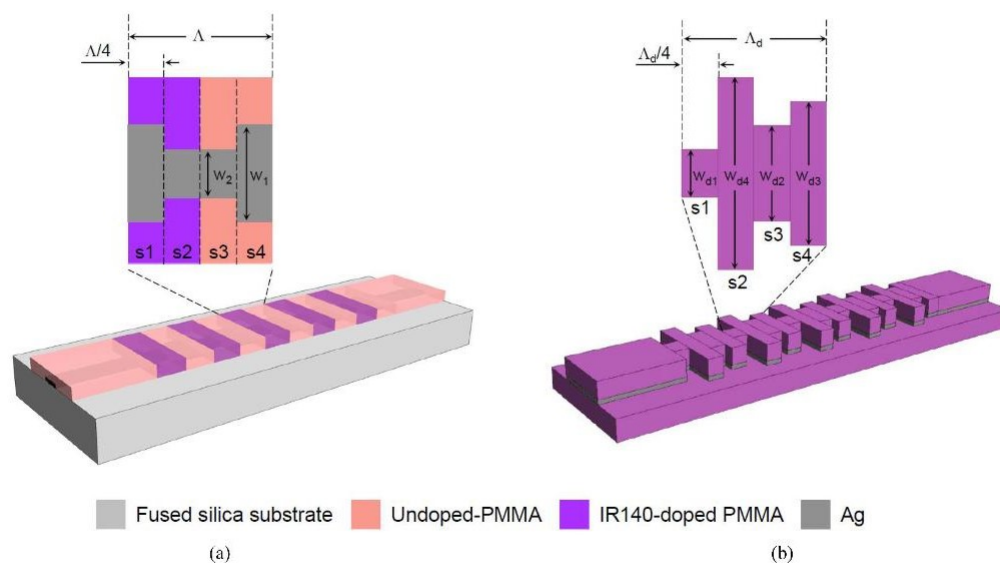


Fig. 3. Schematic illustrations for PT-symmetric Bragg gratings based on plasmonic waveguides supporting LRSPP modes. (a) Alternate modulation of Ag width and IR140 doping region. (b) Complex index controlled by four different widths.

The basic architecture of a periodically-doped grating is shown in Fig. 3(a) [13]. We assume fused silica as a substrate and a 20-nm-thick Ag stripe with a stepped width as a passive grating. The real index modulation generated by stepping the Ag width is suitable for a Bragg grating, as was demonstrated experimentally [15]. Two widths of the Ag stripe in a period can be selected to produce a desired real index difference—here we choose  $w_1 = 1 \mu\text{m}$  and  $w_2 = 0.96 \mu\text{m}$  with a 50% duty cycle. The stepped Ag stripe is covered by a 1- $\mu\text{m}$ -thick PMMA layer over the whole length. The PMMA layer is periodically doped by IR140 dye with same duty cycle and period. The  $\pm\pi/2$  phase shift between the real and imaginary index distribution, which is necessary for PT symmetry, is obtained by spatially shifting the periodically-doped PMMA layer  $\pm\Lambda/4$ . Since the refractive index of fused silica is slightly lower than that of the top layered PMMA, we choose the thickness of the latter as  $1 \mu\text{m}$  to lower effectively the index of the top part. The designed structure therefore operates in the LRSPP mode.

Another PT symmetric Bragg grating structure based on the dielectric-loaded LRSPP (DL-LRSPP) waveguide is illustrated in Fig. 3(b) [14]. The DL-LRSPP waveguides are typically composed of a patterned dielectric top ridge on a thin metal film on a dielectric substrate [51]. As shown, the DL-LRSPP Bragg grating structure has stepped a Ag stripe, similarly to the periodically-doped Bragg grating, but it is covered by IR140-doped PMMA layers for the top ridge and bottom cladding to enhance gain efficiency. It has been reported theoretically and experimentally that the DL-LRSPP waveguide can have almost double the modal gain by employing an IR140-doped PMMA

layer for both the top and bottom claddings [52]. We assume a 5- $\mu\text{m}$ -thick bottom cladding of optically semi-infinite thickness, and we carefully select the thickness and width for operating in a single LRSPP mode. The thickness of top ridge is selected as 950 nm because the cutoff thickness of TE modes is 980 nm for a 4- $\mu\text{m}$ -wide ridge. The higher-order TM modes are eliminated by adjusting the width narrower than the cutoff of the higher modes  $\sim 4.5 \mu\text{m}$ .

The real and imaginary index distribution satisfying the PT symmetric condition is obtained by selecting four widths for a period as in the top view shown in Fig. 3(b). These four widths can be selected around the crossing width of real index of the symmetric TM mode and anti-symmetric higher-order mode. The real and imaginary index of a typical waveguide structure varies monotonically with respect to changes in the structure geometry. Thus it is impossible to find such widths to satisfy the PT symmetric condition which requires even and odd symmetry for the real and imaginary index in a period, respectively. However, we can find such widths in DL-LRSPP waveguides because the effective index does not vary monotonically near the coupling width as shown in Fig. 4. The black curve in Fig. 4(a) and (b) plots the real and imaginary index versus top ridge width, respectively, and the vertical blue line indicates the coupling width between the fundamental LRSPP mode and higher-order anti-symmetric mode. The supermode character due to the coupling of these modes occurs as a large dip for the imaginary index whereas a local peak then a local dip is observed for the real index with increasing width. Therefore, we can find four widths to create a PT symmetric distribution of complex index over the

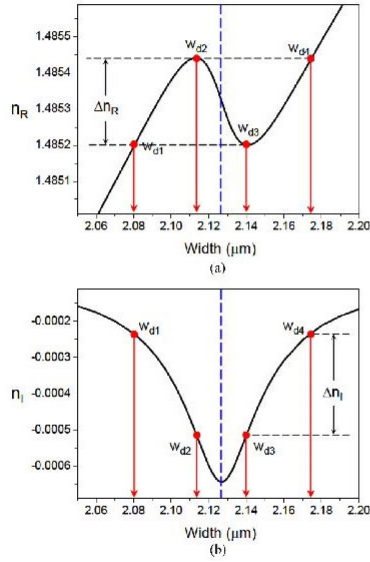


Fig. 4. (a) Real and (b) imaginary parts of effective index for the DL-LRSPP waveguide as a function of top ridge width for 35-nm-thick Ag stripe. The filled red circle and arrows indicate the four widths selected for a PT symmetric Bragg grating and the vertical blue dashed line denotes the coupling width between the symmetric TM mode and anti-symmetric higher mode.

width range shown in Fig. 4. Firstly, as marked, we can select two width  $w_{d2}$  and  $w_{d3}$  at the local peak and dip, such that these two widths have a different real index but the same imaginary index. Then, we can select two more widths which have the same real index with  $w_{d2}$  and  $w_{d3}$  marked as  $w_{d4}$  and  $w_{d1}$  in Fig. 4. These two widths also have the same imaginary index but of a different value than the imaginary index of  $w_{d2}$  and  $w_{d3}$ . Now we can arrange the four selected widths within a period in the sequence of  $w_{d1}$ ,  $w_{d4}$ ,  $w_{d2}$ , and  $w_{d3}$  as shown in Fig. 3(b). The arranged period has even symmetric real index and odd symmetric imaginary index, thus operating as a PT symmetric Bragg grating. The material gain of IR140-doped PMMA was not considered in the calculations of Fig. 4. Thus the grating has a non-zero average imaginary index however it remains PT symmetric because this represents a gauge transformation [9]. Introducing material gain (via IR140-doped PMMA) leads to better performance.

Another important parameter of PT symmetric gratings is the balance factor  $\gamma$ . In the DL-LRSPP grating,  $\gamma$  is determined by the real and imaginary index modulation, denoted  $\Delta n_R$  and  $\Delta n_I$  in Fig. 4, which are fixed for a fixed Ag thickness. But  $\gamma$  can be adjusted by controlling the Ag thickness or through material gain without altering the PT symmetric index distribution.

### B. Asymmetric Reflection

We observe asymmetric reflection which is an interesting feature of a PT symmetric index distribution. We compute

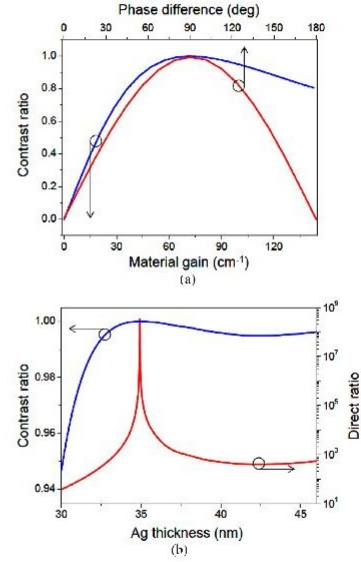


Fig. 5. (a) Contrast ratio of periodically-doped PT symmetric gratings (Fig. 3 (a)) as a function of phase difference with  $68 \text{ cm}^{-1}$  of fixed material gain (red), and as a function of material gain with  $90^\circ$  of fixed phase difference (blue). (b) Direct (red) and contrast (blue) ratios of DL-LRSPP PT-symmetric gratings (see Fig. 3(b)) as a function of Ag thickness.

the reflectance using the TMM. In the calculation 4000 periods were assumed. The period of each grating is obtained via the Bragg equation  $\Lambda = \lambda_B / 2n_{\text{ave}}$ , where  $\lambda_B = 880 \text{ nm}$  is the Bragg wavelength, and  $n_{\text{ave}} = \text{Re}[n_{s1} + n_{s2} + n_{s3} + n_{s4}] / 4$  is the average index of the four sections of the grating marked as s1-s4 in Fig. 3. We plot the contrast ratio as a measure of the asymmetry of the gratings' reflectance, defined as:

$$C \equiv \left| \frac{R_r - R_l}{R_r + R_l} \right|. \quad (6)$$

Here,  $R_r$  and  $R_l$  are the reflectance for right- and left-incident light, respectively. Note that,  $C = 1$  can be obtained for an ideal PT symmetric grating at the breaking point, which implies the most asymmetric operation, and  $C = 0$  is obtainable for a conventional real index grating implying symmetric operation. The contrast ratio for periodically-doped PT symmetric gratings is plotted in Fig. 5(a) as a function of the material gain of the IR140-doped PMMA layer with a fixed phase difference of  $90^\circ$  (blue curve), and as a function of phase difference with a fixed material gain of  $68 \text{ cm}^{-1}$  (red curve). As shown, the maximum asymmetry requires  $90^\circ$  of phase difference.

The grating has only real index modulation at zero material gain (i.e., external pumping is not applied) because the absorption of IR140-doped PMMA is negligible at  $\lambda_B$ . Therefore, the reflectance is symmetric at this point which gives  $C = 0$ .  $C$  increases with pumping until maximum  $\gamma$  is achieved at a material gain of  $71.4 \text{ cm}^{-1}$ , which gives  $C = 0.99$ . We obtained

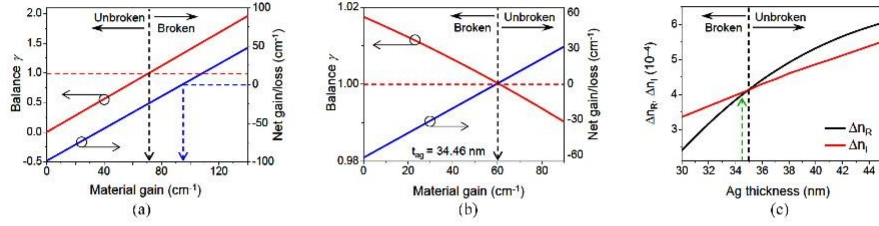


Fig. 6. Balance factor  $\gamma$  and net gain/loss as a function of material gain of the IR140-doped PMMA for (a) periodically-doped PT-symmetric grating and (b) DL-LRSPP waveguide based PT-symmetric Bragg grating. The vertical black arrows indicate the material gain that corresponds to the PT-symmetry breaking point for each structure, (c)  $\Delta n_R$  and  $\Delta n_I$  as a function of Ag thickness for the DL-LRSPP waveguide-based PT-symmetric Bragg grating.

a maximum  $C$  less than 1 because stepping the Ag width also slightly changes the imaginary effective index. This design guarantees a contrast ratio of over 90% for a material gain in the range of 45 to 114 cm<sup>-1</sup> and a phase difference in the range of 63° to 114°, corresponding to a spatial offset of 0.17 to 0.32 $\lambda$ . These quite large ranges infer that the designed structure can easily provide high contrast ratio asymmetry, using e-beam or deep UV lithography.

Asymmetric reflection of DL-LRSPP waveguide-based PT symmetric gratings is also characterized by the contrast (blue) and direct (red,  $R_t/R_i$ ) ratios plotted in Fig. 5(b). In this grating, the phase difference between the real and imaginary index distributions is determined by dividing a period into four sections and selecting the widths to have a PT symmetric index distribution. Neglecting the material gain of IR140-doped PMMA,  $\gamma$  is determined by selecting the thickness of Ag stripe. In Fig. 5(b), we considered the range of Ag thickness as 30 to 46 nm. Typically waveguide structures supporting LRSPP modes employ a thinner Ag thickness because it has lower losses. However, the DL-LRSPP waveguide structure with a Ag thickness less than 30 nm has a weak supermode character, making it impossible to find four widths satisfying PT symmetry. By increasing the thickness of Ag from 30 nm, the modulation of the real and imaginary index ( $\Delta n_R$  and  $\Delta n_I$ ) increase. At a Ag thickness of 30 nm, the PT symmetric grating is in the broken state with  $\gamma > 1$ . However,  $\Delta n_R$  increases faster than  $\Delta n_I$  with increasing Ag thickness as shown in Fig. 6(c), thus the grating reaches the breaking point at 35 nm and the unbroken state beyond. The maximum asymmetry occurs at the breaking point, as observed by the direct ratio in Fig. 5(b). However,  $C$  remains above 0.94 over the considered Ag thickness range, indicating that the design based on the DL-LRSPP waveguide is practical and the structure provides high asymmetry as the periodically-doped grating.

### C. Active Control of the Balance Factor

The phase shift between the real and imaginary index distribution is fixed by the geometry. Then, the balance parameter  $\gamma$  can be controlled by external pumping (i.e., via the material gain of IR140-doped PMMA). The periodically-doped PT symmetric grating is the same as a conventional real index grating when there is no external pumping ( $\gamma = 0$ ). By increasing the pump power,  $\gamma$  and  $G_{\text{net}}$  (net gain or loss) increase as shown

in Fig. 6(a) as a function of material gain (the red and blue curves correspond to  $\gamma$  and  $G_{\text{net}}$ , respectively). The horizontal red dashed line indicates  $\gamma = 1$ , thus the material gain indicated by the black arrow is the breaking point. The breaking point is not equivalent to  $G_{\text{net}} = 0$ , but maximum asymmetry occurs at the breaking point (see Fig. 5(a)).

Similar plots for the DL-LRSPP waveguide-based PT symmetric Bragg grating are given in Fig. 6(b) and (c). Contrary to the previous case, this grating has both real and imaginary index modulations without material gain, thus it is PT symmetric even if not pumped.  $\Delta n_R$  and  $\Delta n_I$  of the passive (un-pumped) grating is plotted in Fig. 6(c).  $\Delta n_R$  and  $\Delta n_I$  are the same at a particular thickness corresponding to the breaking point.  $\Delta n_R$  and  $\Delta n_I$  can be changed through the material gain, which implies that the thickness which produces  $\gamma \neq 1$  can be tuned to the breaking point ( $\gamma = 1$ ) via the external pump.  $\gamma$  and  $G_{\text{net}}$  of the grating versus material gain are plotted in Fig. 6(b) for a Ag thickness of 34.46 nm marked as green arrow in Fig. 6(c). This thickness is slightly thinner than that at the breaking point, so the grating is in the broken state before the external pump applied. Note that the particular Ag thickness of 34.36 nm is selected to show that it is possible to achieve  $\gamma = 1$  and  $G_{\text{net}} = 0$  simultaneously by adjusting the geometry.  $\gamma$  and  $G_{\text{net}}$  are plotted versus material gain as the red and blue curves in Fig. 6(b). The dashed red line indicates  $\gamma = 1$  and  $G_{\text{net}} = 0$ . The PT symmetric grating is in the broken state when there is no material gain, and evolves to the breaking point ( $\gamma = 1$ ) by increasing the material gain to 59.5 cm<sup>-1</sup> as marked by the black arrow in Fig. 6(b). At this material gain the PT symmetric grating has an exactly odd symmetric imaginary index distribution so the asymmetry of the grating at this level of material gain is maximal.

For both designed gratings,  $\gamma$  is controllable by the external pump through the IR140-doped PMMA. This is an advantage for fabrication because the balance can be tuned actively after fabrication. This also implies that PT symmetric gratings can be applied for all-optical switching because the asymmetry can be controlled optically.

### D. Group and Energy Velocities of Designed PT Symmetric Bragg Gratings

As mentioned earlier, a PT symmetric Bragg grating is dispersionless ( $v_g$  and  $v_e$ ) which implies that an incident pulse can

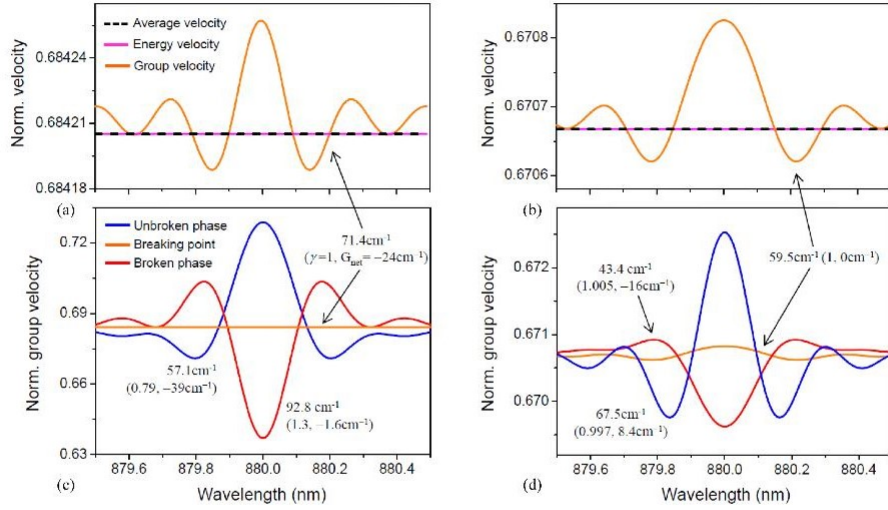


Fig. 7. (a) Normalized group (orange) and energy (magenta) velocities of a periodically-doped PT symmetric Bragg grating. (b) Group velocities of a periodically-doped PT symmetric grating in the unbroken (blue) and broken (red) states and at the breaking point (orange). (c) and (d) same as (a) and (b) but for the DL-LRSPP waveguide-based PT symmetric Bragg grating.

be transmitted through the grating without pulse shape broadening. We calculate  $v_g$  and  $v_e$  for three different material gain levels in the broken and unbroken states, and at the symmetry breaking point. The selected material gain is labeled in Fig. 7(b) and (d) (with the corresponding  $\gamma$  and  $G_{net}$  in parentheses) for the two designed gratings. For the periodically-doped PT symmetric Bragg grating, the breaking point occurs at  $71.4 \text{ cm}^{-1}$  of material gain. We choose  $57.1$  and  $92.8 \text{ cm}^{-1}$  as the material gains for the unbroken and broken states. For the DL-LRSPP waveguide-based grating, the breaking point occurs at  $59.5 \text{ cm}^{-1}$  of material gain, and we choose  $43.4$  and  $67.5 \text{ cm}^{-1}$  for the broken and unbroken states.

$v_g$  and  $v_e$  normalized to the vacuum speed of light are plotted in Fig. 7. As shown in Fig. 7(a) and (c) (orange curves),  $v_g$  is approximately constant for the two gratings at the symmetry breaking point.  $v_e$  of the two gratings are plotted with the average velocity which is the speed of light in a uniform medium of the averaged index of the unit cell. The  $v_g$  for the broken and unbroken states are plotted as the red and blue curves, respectively, in Fig. 7(b) and (d). The broken and unbroken states of the periodically-doped grating have net loss, and the DL-LRSPP waveguide-based grating has net loss and net gain for the broken and unbroken states, respectively. However, the broken states clearly show an inverted response relative to the unbroken states as observed earlier relative to the generic grating (see Fig. 1) even though they have net gain or loss.  $v_g$  of both PT symmetric gratings based on the periodically-doped LRSPP waveguide and the DL-LRSPP waveguide can be completely inverted by adjusting the material gain (i.e., controlling the external pumping level). Therefore, these two plasmonic grating structures can be applied to control the dispersion and asymmetric reflectance.

## V. CONCLUSION

We proposed two PT symmetric Bragg gratings based on plasmonic structures. One uses a plasmonic waveguide composed of a thin Ag stripe supporting LRSPP modes. Real index modulation is obtained by stepping the width of the Ag stripe, and the imaginary index modulation is obtained by periodically doping the top cladding while ensuring a  $\Lambda/4$  spatial shift. Over 90% asymmetry can be produced with a material gain in the range from  $45$  to  $114 \text{ cm}^{-1}$  while maintaining a phase shift in the range of  $63^\circ$  to  $114^\circ$  for a spatial shift of  $0.17$  to  $0.32\lambda$  at fixed material gain.

The other is based on the DL-LRSPP waveguide structure. The complex index distribution is obtained by arranging four different widths to satisfy the PT symmetry condition. It is possible to choose these four widths due to the supermode character that occurs by coupling between the LRSPP mode and anti-symmetric higher-order modes. Over 94% asymmetry can be produced over a wide range of Ag thickness without gain; however, introducing gain improves the performance.

The balance factor  $\gamma$  can be controlled via the material gain, so the state of PT symmetry is tunable for both grating structures. The energy and group velocity, which are related to energy transport and pulse reshaping, are computed for three material gain values in the broken and unbroken states, and at the PT symmetry breaking point. These velocities are constant over wavelength (dispersionless) at the PT symmetry breaking point, so the incident light does not experience the complex index modulation here. The broken and unbroken states have an inverted shape for the group velocity spectrum. Therefore, controlling the group velocity can be achieved in the proposed gratings by simply adjusting the material gain (pump).

Asymmetric reflectance is a new functionality achieved by introducing PT symmetry into Bragg gratings. The asymmetric reflectance of a PT symmetric Bragg grating is determined by the balance factor  $\gamma$  which is a function of material gain in the proposed gratings. The proposed gratings use plasmonic structures and can be integrated on chip. Thus, the observed properties infer that the proposed gratings are good candidates for device applications with controllable multi-functionalities.

#### REFERENCES

- [1] C. M. Bender and S. Boettcher, "Real spectra in non-Hermitian hamiltonians having PT symmetry," *Phys. Rev. Lett.*, vol. 80, no. 24, pp. 5243–5246, Jun. 1998.
- [2] M. Kulishov, J. Laniel, N. Bélanger, J. Azaña, and D. Plant, "Nonreciprocal waveguide Bragg gratings," *Opt. Exp.*, vol. 13, no. 8, pp. 3068–3078, Apr. 2005.
- [3] C. E. Rüter *et al.*, "Observation of parity–time symmetry in optics," *Nature Phys.*, vol. 6, no. 3, pp. 192–195, Jan. 2010.
- [4] J. D. Joannopoulos, P. R. Villeneuve, and S. Fan, "Photonic crystals: Putting a new twist on light," *Nature*, vol. 386, no. 6621, pp. 143–149, Mar. 1997.
- [5] T. J. Cui, D. R. Smith, and R. Liu, *Metamaterials*. New York, NY, USA: Springer, 2014.
- [6] L. Feng *et al.*, "Nonreciprocal light propagation in a silicon photonic circuit," *Science*, vol. 333, no. 6043, pp. 729–733, Aug. 2011.
- [7] A. Regensburger *et al.*, "Parity–time synthetic photonic lattices," *Nature*, vol. 488, no. 7410, pp. 167–171, Aug. 2012.
- [8] C. Dembowski *et al.*, "Encircling an exceptional point," *Phys. Rev. E*, vol. 69, no. 5, art. no. 056216, May. 2004.
- [9] A. Guo *et al.*, "Observation of PT-symmetry breaking in complex optical potentials," *Phys. Rev. Lett.*, vol. 103, no. 9, art. no. 093902, Aug. 2009.
- [10] H. Benisty *et al.*, "Implementation of PT symmetric devices using plasmonics: Principle and applications," *Opt. Exp.*, vol. 19, no. 19, pp. 18004–18019, Sep. 2011.
- [11] P. Berini and I. De Leon, "Surface plasmon–polariton amplifiers and lasers," *Nature Photon.*, vol. 6, no. 1, pp. 16–24, Dec. 2011.
- [12] P. Berini, "Long-range surface plasmon polaritons," *Adv. Opt. Photon.*, vol. 1, no. 3, pp. 484–588, Nov. 2009.
- [13] E. K. Keshmarzi, R. N. Tait, and P. Berini, "Spatially nonreciprocal Bragg gratings based on surface plasmons," *Appl. Phys. Lett.*, vol. 105, no. 19, art. no. 191110, Nov. 2014.
- [14] C. Hahn, S. H. Song, C. H. Oh, and P. Berini, "Single-mode lasers and parity–time symmetry broken gratings based on active dielectric-loaded long-range surface plasmon polariton waveguides," *Opt. Exp.*, vol. 23, no. 15, pp. 19922–19931, Jul. 2015.
- [15] S. Jetté-charbonneau, R. Charbonneau, N. Lahoud, G. A. Mattiussi, and P. Berini, "Bragg gratings based on long-range surface plasmon-polariton waveguides: Comparison of theory and experiment," *IEEE J. Quantum Electron. Quantum Electron.*, vol. 41, no. 12, pp. 1480–1491, Dec. 2005.
- [16] L. Poladian, "Resonance mode expansions and exact solutions for nonuniform gratings," *Phys. Rev. E*, vol. 54, no. 3, pp. 2963–2975, Sep. 1996.
- [17] R. Birabassov, A. Yesayan, and T. V. Galstyan, "Nonreciprocal diffraction by spatial modulation of absorption and refraction," *Opt. Lett.*, vol. 24, no. 23, pp. 1669–1671, Dec. 1999.
- [18] M. Greenberg and M. Orenstein, "Irreversible coupling by use of dissipative optics," *Opt. Lett.*, vol. 29, no. 5, pp. 451–453, Mar. 2004.
- [19] M. Greenberg and M. Orenstein, "Unidirectional complex grating assisted couplers," *Opt. Exp.*, vol. 12, no. 17, pp. 4013–4018, Aug. 2004.
- [20] M. Kulishov, J. Laniel, N. Bélanger, and D. Plant, "Trapping light in a ring resonator using a grating-assisted coupler with asymmetric transmission," *Opt. Exp.*, vol. 13, no. 9, pp. 3567–3578, May 2005.
- [21] A. Ruschhaupt, F. Delgado, and J. Muga, "Physical realization of PT-symmetric potential scattering in a planar slab waveguide," *J. Phys. A*, vol. 38, no. 9, pp. L171–L176, Feb. 2005.
- [22] R. El-Ganainy and K. Makris, "Theory of coupled optical PT-symmetric structures," *Opt. Lett.*, vol. 32, no. 17, pp. 2632–2634, Sep. 2007.
- [23] K. G. Makris, R. El-Ganainy, D. N. Christodoulides, and Z. H. Musslimani, "Beam dynamics in PT symmetric optical lattices," *Phys. Rev. Lett.*, vol. 100, no. 10, art. no. 103904, Mar. 2008.
- [24] K. Makris and R. El-Ganainy, "PT-symmetric periodic optical potentials," *Int. J. Theor. Phys.*, vol. 50, no. 4, pp. 1019–1041, Apr. 2011.
- [25] Z. Lin *et al.*, "Unidirectional invisibility induced by PT-symmetric periodic structures," *Phys. Rev. Lett.*, vol. 106, no. 21, art. no. 213901, May 2011.
- [26] S. Longhi, F. Cannata, and A. Ventura, "Spontaneous PT symmetry breaking in Dirac-Kronig-Penney crystals," *Phys. Rev. B*, vol. 84, no. 23, art. no. 235131, Dec. 2011.
- [27] M. Kulishov, B. Kress, and R. Slavik, "Resonant cavities based on parity-time-symmetric diffractive gratings," *Opt. Exp.*, vol. 21, no. 8, pp. 9473–9483, Apr. 2013.
- [28] L. Feng *et al.*, "Experimental demonstration of a unidirectional reflectionless parity-time metamaterial at optical frequencies," *Nature Mater.*, vol. 12, no. 2, pp. 108–113, Feb. 2013.
- [29] S. Phang, A. Vukovic, H. Susanto, T. M. Benson, and P. Sewell, "Ultrafast optical switching using parity–time symmetric Bragg gratings," *J. Opt. Soc. Amer. B*, vol. 30, no. 11, pp. 2984–2991, Nov. 2013.
- [30] Y.-L. Xu, L. Feng, M.-H. Lu, and Y. Chen, "Unidirectional Transmission based on a passive PT symmetric grating with a nonlinear silicon distributed Bragg reflector cavity," *IEEE Photon. J.*, vol. 6, no. 1, art. no. 0600507, Feb. 2014.
- [31] A. Lupu, H. Benisty, and A. Degiron, "Using optical PT-symmetry for switching applications," *Photon. Nanostructures—Fundam. Appl.*, vol. 12, no. 4, pp. 305–311, Aug. 2014.
- [32] X.-F. Zhu, Y.-G. Peng, and D.-G. Zhao, "Anisotropic reflection oscillation in periodic multilayer structures of parity–time symmetry," *Opt. Exp.*, vol. 22, no. 15, pp. 18401–18411, Jul. 2014.
- [33] Y. Yan and N. C. Giebink, "Passive PT symmetry in organic composite films via complex refractive index modulation," *Adv. Opt. Mater.*, vol. 2, no. 5, pp. 423–427, Feb. 2014.
- [34] Y. Jia, Y. Yan, S. V. Kesava, E. D. Gomez, and N. C. Giebink, "Passive parity–time symmetry in organic thin film waveguides," *ACS Photon.*, vol. 2, no. 2, pp. 319–325, Jan. 2015.
- [35] S. Nixon and J. Yang, "Light propagation in periodically modulated complex waveguides," *Phys. Rev. A*, vol. 91, no. 3, art. no. 033807, Mar. 2015.
- [36] S. Klaiman, U. Günther, and N. Moiseyev, "Visualization of branch points in PT-symmetric waveguides," *Phys. Rev. Lett.*, vol. 101, no. 8, art. no. 080402, Aug. 2008.
- [37] J. Ctyroky, V. Kuzmiak, and S. Eyderman, "Waveguide structures with antisymmetric gain/loss profile," *Opt. Exp.*, vol. 18, no. 21, pp. 21585–21593, Oct. 2010.
- [38] A. Lupu, H. Benisty, and A. Degiron, "Switching using PT symmetry in plasmonic systems: Positive role of the losses," *Opt. Exp.*, vol. 21, no. 18, pp. 21651–21668, Sep. 2013.
- [39] H. Alaeian and J. A. Dionne, "Non-Hermitian nanophotonic and plasmonic waveguides," *Phys. Rev. B*, vol. 89, no. 7, art. no. 075136, Feb. 2014.
- [40] Y. Choi *et al.*, "Parity–time–symmetry breaking in double-slab surface-plasmon-polariton waveguides," *Opt. Exp.*, vol. 23, no. 9, pp. 11783–11789, May 2015.
- [41] L. Feng, S. J. Wong, R.-M. Ma, Y. Wang, and X. Zhang, "Single-mode laser by parity–time symmetry breaking," *Science*, vol. 346, no. 6212, pp. 972–975, Oct. 2014.
- [42] H. Hodaie, M. Miri, and M. Heinrich, "Parity–time–symmetric microring lasers," *Science*, vol. 346, no. 6212, pp. 975–978, Oct. 2014.
- [43] B. Baum, H. Alaeian, and J. Dionne, "A parity–time symmetric coherent plasmonic absorber-amplifier," *J. Appl. Phys.*, vol. 117, no. 6, art. no. 063106, Feb. 2015.
- [44] Y. Huang, G. Veronis, and C. Min, "Unidirectional reflectionless propagation in plasmonic waveguide-cavity systems at exceptional points," *Opt. Exp.*, vol. 23, no. 23, pp. 29882–29895, Nov. 2015.
- [45] S. Longhi, "PT-symmetric laser absorber," *Phys. Rev. A*, vol. 82, no. 3, p. 031801(R), Sep. 2010.
- [46] S. Longhi, M. Marano, M. Belmonte, and P. Laporta, "Superluminal pulse propagation in linear and nonlinear photonic grating structures," *IEEE J. Sel. Topics Quantum Electron.*, vol. 9, no. 1, pp. 4–16, Feb. 2003.
- [47] K. Sakoda, *Optical Properties Photonic Crystals*. New York, NY, USA: Springer, 2004.
- [48] G. Torrese, J. Taylor, H. P. Schriemer, and M. Cada, "Energy transport through structures with finite electromagnetic stop gaps," *J. Opt. A: Pure Appl. Opt.*, vol. 8, no. 11, pp. 973–980, Nov. 2006.
- [49] P. Yeh, *Optical Waves Layered Media*. Hoboken, NJ, USA: Wiley, 1988.
- [50] E. K. Keshmarzi, R. N. Tait, and P. Berini, "Near infrared amplified spontaneous emission in a dye-doped polymeric waveguide for active plasmonic applications," *Opt. Exp.*, vol. 22, no. 10, pp. 12452–12460, May 2014.

## 6. Conclusions and future work

### 6.1 Concluding remarks

Plasmonic structures suffer highly by their intrinsic metallic attenuation which constrains their application to a great extent. Incorporation of optical gain in plasmonic devices has been greatly investigated during the last decade using various gain media in different SPP supporting structures. The goal has been to compensate the attenuation and increase SPP propagation length. Over compensation of loss has also been pursued to develop SPP amplifiers or SPP laser sources. Although numerous theoretical studies have been conducted on this topic but yet there are many avenues open to explore and in particular experimental demonstrations have been limited.

In this thesis we successfully demonstrated lasing with two-dimensional long-range surface plasmon polariton (LRSP) structure. This type of plasmonic laser offers new architecture suitable for integration with passive LRSP elements, and uses organic gain media based on optically-pump IR-140 doped PMMA. IR-140 dye molecules have a relatively large transition cross section and they produce a fair optical gain (about  $80 \text{ cm}^{-1}$ ) at about 880 nm. Cost effectiveness, ease of processing and fabrication, and wide wavelength tunability are properties which turn IR-140 doped PMMA to be a promising gain media at near infrared.

Ag and Au DFBs in LRSP configuration were realized and showed highly coherent lasing with good modal confinement at near infrared using moderate pump intensities and at room temperature.

We also suggested PT symmetric Bragg gratings operating in LRSP structure by using the same gain media and balanced with the LRSP's loss to exhibit unidirectional

reflectance. The proposed plasmonic-based PT symmetry Bragg gratings in this thesis are novel devices with great application potential. While the materials used in these structures are linear they demonstrate asymmetric reflectance and dispersion-less pulse transmission. Optical processing and switching are among applications can be predicted for this kind of devices.

List of articles published in the refereed journals throughout this Ph.D. are listed in below:

- Elham Karami Keshmarzi, R Niall Tait, Pierre Berini, “Long-range surface plasmon single-mode laser concepts”, *Journal of Applied Physics* 112, 063115 (1-5), 2012.
- Elham Karami Keshmarzi, R Niall Tait, Pierre Berini, “Near infrared amplified spontaneous emission in a dye-doped polymeric waveguide for active plasmonic applications”, *Optics Express* 22, 12452-12460, 2014.
- Elham Karami Keshmarzi, R Niall Tait, Pierre Berini, “Spatially nonreciprocal Bragg gratings based on surface plasmons”, *Applied Physics Letters* 105, 191110 (1-4), 2014.
- Elham Karami Keshmarzi, R Niall Tait, Pierre Berini, “Parity-time symmetry broken Bragg grating operating with long-range surface plasmon polaritons”, *Journal of Applied Physics A* 122 (4), 1-5, 2016.
- Choloong Hahn, Elham Karami Keshmarzi , Seok Ho Song , Cha Hwan Oh , R. Niall Tait , Pierre Berini, “Udirectional Bragg Gratings Using Parity-Time Symmetry Breaking in Plasmonic Systems”, *IEEE Journal of Selected Topics in Quantum Electronics* 22 (5), 1-12, 2016.
- Elham Karami Keshmarzi, R Niall Tait, Pierre Berini, “Surface Plasmon Single-Mode Distributed Feedback Lasers”, to be submitted for publication.

## 6.2 Future work

Although extensive work has been performed already in this thesis, there is still much future work to accomplish. The future work can be summarized as in below:

- **Fabrication improvement to produce high quality stepped-in-width Ag stripes**

Ag has a lower loss compared to other plasmonic metals and is widely used in plasmonic systems. However, Ag is a highly reactive material which turns it susceptible to its ambient environment. For Ag deposition using thermal or electron beam evaporation techniques, it is essential that a high pressure vacuum ( $\sim 1 \times 10^{-8}$  Torr) is supplied in the evaporation chamber. Otherwise any oxygen or water vapor molecules can interact with Ag and induce impurities. Also it is critical that the chamber temperature is not too high. This is because Ag cannot properly wet the sample's surface even at the room temperature.

For a 20 nm-thick Ag deposition, a very low roughness (sub nanometer) is required. In my best deposition attempts so far 1.2 nm roughness is achieved for a 20 nm-thick Ag or about 6% roughness.

The other factors important in producing a good quality stepped-in-width Ag stripe is to have a right bi-layer resist for electron beam lithography and fine exposure parameters. It is necessary to produce adequate undercut in the resist so that after Ag deposition and lift off, artifacts such as wings will not remain.

- **Accurate linewidth measurement for LRSPP DFB lasers using heterodyning techniques**

Up to now the best performing LRSPP DFB laser has shown a FWHM  $\sim 0.2$  nm which is almost as narrow as the resolution of the spectrograph used for DFB characterization. A more accurate linewidth measurement is necessary to evaluate the coherency of LRSPP DFB lasers. Heterodyning techniques based on beating the laser beams from the source under test and a tunable source of known linewidth and detecting the beat note by a fast photo receiver is usually an established method to obtain the linewidth of unknown source.

- **Realization of LRSPP DFB lasers using Pyrex**

As was explained in chapter 4, the contrast between the refractive index of the SiO<sub>2</sub> substrate and IR-140 doped PMMA top cladding decreases the LRSPP's MPG and tightens the design range for Ag and Au DFB lasers. Pyrex is an available substrate which can replace with SiO<sub>2</sub> to reduce the index contrast and increase the design range. Also Ag and Au DFBs using Pyrex have larger MPG which can lower the DFBs lasing threshold and increase the quality factor. The challenge with Pyrex wafers is that they cannot be easily cleaved to produce high quality optical facets. It is required to dice the samples made of Pyrex substrates and then polish the sample's edge without damaging the deposited layers.

- **Realization of a LRSPP PT symmetric Bragg grating using periodic doped and undoped PMMA top cladding**

The fabrication processes for this device is already considered. After depositing the stepped-in-width Ag stripe on the substrate, an undoped PMMA is spun and cured on the sample. Then an electron beam lithography followed by development is performed to create an undoped PMMA pattern. A liquid gain media in the form of IR-140 molecules

dissolved in an index-matched solution is poured on the sample in a precise quantity so that the liquid fills in the hollow regions and arrive at a same thickness as undoped PMMA regions.

- **Investigation of a LRSPP PT symmetric laser**

Using a long stepped-in-width Ag Bragg grating (up to 10 mm) and replacing the SiO<sub>2</sub> substrate with Pyrex to increase LRSPP modal gain, would increase the non-zero coupling coefficient in the PT symmetric Bragg grating with periodic doped and undoped PMMA top cladding, so that an amplified reflectance would occur. Lasing is possible with reflectance greater than 1 and this laser unlike the two output port DFB lasers, has only one output port.

## References

---

- [1] S. A. Maier, *Plasmonics: Fundamentals and Applications*. Springer-Verlag, Berlin, (2007).
- [2] T. W. Ebbesen, C. Genet, and S. I. Bozhevolnyi, Surface plasmon circuitry. *Phys. Today* 61, 44–50, (2008).
- [3] J. Homola, Surface plasmon resonance sensors for detection of chemical and biological species, *Chem. Rev.* 108, 462–493, (2008).
- [4] F. Xu, G. Chen, C. Wang, B. Cao, and Y. Lou, Superlens imaging with a surface plasmon polariton cavity in imaging space, *Opt. Lett.* 138, 3819–3822, (2013).
- [5] K. A. Willets, and R. P. Van Duyne, Localized Surface Plasmon Resonance Spectroscopy and Sensing, *Phys. Chem.* 58, 267–297, (2007).
- [6] X. Luo, and T. Ishihara, Subwavelength photolithography based on surface-plasmon polariton resonance, *Opt. Exp.* 12, 3055–3065, (2004).
- [7] X. Luo, L. Yan, Surface Plasmon Polaritons and Its Applications, *IEEE Phot. J.* 4, 590–595, (2012).
- [8] W. L. Barnes, A. Dereux, and T. W. Ebbesen, Surface plasmon subwavelength optics, *Nature* 424, 824–830, (2003).
- [9] P. Zijlstra, P. M. R. Paulo, and M. Orrit, Optical detection of single non-absorbing molecules using the surface plasmon resonance of a gold nanorod, *Nat. Nanotech.* 7, 379–382, (2012).
- [10] P. Berini, and I. De Leon, Surface plasmon-polariton amplifiers and lasers, *Nat. Photonics* 6, 16–24, (2012).
- [11] P. Berini, E. Rüter, K. G. Makris, R. El-Ganainy, D. N. Christodoulides, M. Segev, and D. Kip, Observation of parity–time symmetry in optics, *Nat. Phys.* 6, 192–195, (2010).
- [12] C. Hahn, E. K. Keshmarzi, S. H. Song, C. H. Oh, R. N. Tait, and P. Berini, Unidirectional Bragg Gratings Using Parity- Time Symmetry Breaking in Plasmonic Systems, *IEEE J. Sel. Top. Quant. Electr.* 22, No. 5, (2016).
- [13] I. De Leon, and P. Berini, Amplification of long-range surface plasmons by a dipolar gain medium, *Nat. Photonics* 4, 382–387, (2010).
- [14] J. Nkoma, R. Loudon, and D. R. Tilley, Elementary properties of surface plasmons, *J. Phys. C* 7, 3547–3559, (1974).
- [15] A. Archambault, F. Marquier, and J. Greffet, Quantum theory of spontaneous and stimulated emission of surface plasmons, *Phys. Rev. B* 82, 035411 (1–10), (2010).
- [16] R. Matloob, R. Loudon, S. M. Barnett, and J. Jeffers, Electromagnetic field quantization in absorbing dielectrics, *Phys. Rev. A* 52, 4823–4838, (1995).
- [17] W. L. Barnes, Fluorescence near interfaces: the role of photonic mode density, *J. Mod. Opt.* 45, 661–669, (1998).

- 
- [18] P. Berini, Long-range surface plasmon polaritons, *Adv. Opt. Photon.* 1, 484–588, (2009).
- [19] [www.refractiveindex.info](http://www.refractiveindex.info)
- [20] P. Berini, R. Charbonneau and N. Lahoud, G. Mattiussi, Characterization of long-range surface-plasmon-polariton waveguides, *JOURNAL OF APPLIED PHYSICS* 98, 043109, (2005).
- [21] I. De Leon, Amplification of Long-Range Surface Plasmon-Polaritons, Ph.D. dissertation, School of Information Technology and Engineering, University of Ottawa, (2011).
- [22] G. Plotz, H. Simon, and J. Tucciarone, Enhanced total reflection with surface plasmons, *J. Opt. Soc. Am.* 69, 419–422, (1979).
- [23] A. N. Sudarkin, and P. A. Demkovich, Excitation of surface electromagnetic waves on the boundary of a metal with an amplifying medium, *Sov. Phys. Tech. Phys.* 34, 764–766, (1988).
- [24] M. P. Nezhad, K. Tetz, and Y. Fainman, Gain assisted propagation of surface plasmon polaritons on planar metallic waveguides, *Opt. Express* 12, 4072–4079, (2004).
- [25] P. Kumar, V. K. Tripathi, and C. S. Liu, A surface plasmon laser, *J. Appl. Phys.* 104, 033306 (1–4), (2008).
- [26] F. F. Lu, T. Li, J. Xu, Z. D. Xie, L. Li, S. N. Zhu, and Y. Y. Zhu, Surface plasmon polariton enhanced by optical parametric amplification in nonlinear hybrid waveguide, *Opt. Express* 19, 2858–2865, (2011).
- [27] C. Sirtori, C. Gmachl, F. Capasso, J. Faist, D. L. Sivco, A. L. Hutchinson, and A. Y. Cho, Long-wavelength ( $\lambda \approx 11.5 \mu\text{m}$ ) semiconductor lasers with waveguides based on surface plasmons, *Opt. Lett.* 23, 1366–1368, (1998).
- [28] A. Tredicucci, C. Gmachl, F. Capasso, A. L. Hutchinson, D. L. Sivco, and A. Y. Cho, Single-mode surface-plasmon laser, *Appl. Phys. Lett.* 76, 2164–2166, (2000).
- [29] J. Seidel, S. Grafstrom, and L. Eng, Stimulated emission of surface plasmons at the interface between a silver film and an optically pumped dye solution. *Phys. Rev. Lett.* 94, 177401 (1–4), (2005).
- [30] M. A. Noginov, V. A. Podolskiy, G. Zhu, M. Mayy, M. Bahoura, J. A. Adegoke, B. A. Ritzo, and K. Reynolds, Compensation of loss in propagating surface plasmon polariton by gain in adjacent dielectric medium, *Opt. Express* 16, 1385–1392, (2008).
- [31] M. A. Noginov, G. Zhu, M. Mayy, B. A. Ritzo, N. Noginova, and V. A. Podolskiy, Stimulated emission of surface plasmon polaritons, *Phys. Rev. Lett.* 101, 226806 (1–4), (2008).
- [32] P. M. Bolger, W. Dickson, A. V. Krasavin, L. Liebscher, S. G. Hickey, D. V. Skryabin, and A. V. Zayats, Amplified spontaneous emission of surface plasmon polaritons and limitations on the increase of their propagation length, *Opt. Lett.* 35, 1197–1199, (2010).
- [33] I. Avrutsky, Surface plasmons at nanoscale relief gratings between a metal and a dielectric medium with optical gain, *Phys. Rev. B* 70, 155416 (1–6), (2004).
- [34] T. Okamoto, F. H'Dhili, and S. Kawata, Towards plasmonic band gap laser, *Appl. Phys. Lett.* 85, 3968–3970, (2004).

- 
- [35] T. Okamoto, J. Simonen, and S. Kawata, Plasmonic band gaps of structured metallic thin films evaluated for a surface plasmon laser using the coupled-wave approach, *Phys. Rev. B* 77, 115425 (1–8), (2008).
- [36] F. H'Dhili, T. Okamoto, J. Simonen, and S. Kawata, Improving the emission efficiency of periodic plasmonic structures for lasing applications, *Opt. Comm.* 284, 561–566, (2011).
- [37] G. Winter, S. Wedge, and W. L. Barnes, Can lasing at visible wavelength be achieved using the low-loss long-range surface plasmon-polariton mode?, *New J. Phys.* 8, 125–138, (2006).
- [38] Genov, D. A., Ambati, M., and Zhang, X. (2007). Surface plasmon amplification in planar metal films. *IEEE J. Quantum Electron.* 43, 1104–1108.
- [39] I. De Leon, and P. Berini, Theory of surface plasmon-polariton amplification in planar structures incorporating dipolar gain media, *Phys. Rev. B* 78, 161401(R) (1–4), (2008).
- [40] I. De Leon, and P. Berini, Modeling surface plasmon-polariton gain in planar metallic structures, *Opt. Express* 17, 20191–20202, (2009).
- [41] I. De Leon, and P. Berini, Theory of noise in high-gain surface plasmon-polariton amplifiers incorporating dipolar gain media, *Opt. Express* 19, 20506–20517, (2011).
- [42] I. De Leon, and P. Berini, Spontaneous emission in long-range surface plasmon-polariton amplifiers, *Phys. Rev. B* 83, 081414(R) (1–4), (2011).
- [43] M. C. Gather, K. Meerholz, N. Danz, and K. Leosson, Net optical gain in a plasmonic waveguide embedded in a fluorescent polymer, *Nat. Photonics* 4, 457–461, (2010).
- [44] C. Hahn, S. H. Song, C. H. Oh, and P. Berini, Plasmonic gain in long-range surface plasmon polariton waveguides bounded symmetrically by dye-doped polymer, *App. Phys. Lett.* 107, 121107 (1–4), (2015).
- [45] I. P. Radko, M. G. Nielsen, O. Albrektsen, and S. I. Bozhevolnyi, Stimulated emission of surface plasmon polaritons by lead-sulfide quantum dots at near infra-red wavelengths, *Opt. Express* 18, 18633–18641, (2010).
- [46] S. A. Maier, Gain-assisted propagation of electromagnetic energy in sub-wavelength surface plasmon polariton gap waveguides, *Opt. Comm.* 258, 295–299, (2006).
- [47] S. W. Chang, and S. L. Chuang, Normal modes for plasmonic nanolasers with dispersive and inhomogeneous media, *Opt. Lett.* 34, 91–93, (2009).
- [48] S. W. Chang, and S. L. Chuang, Fundamental formulation for plasmonic nanolasers, *IEEE J. Quantum Electron.* 45, 1014–1023, (2009).
- [49] D. B. Li, and C. Z. Ning, Giant modal gain, amplified surface plasmon-polariton propagation, and slowing down of energy velocity in a metal-semiconductor-metal structure, *Phys. Rev. B* 80, 153304 (1–4), (2009).
- [50] D. B. Li, and C. Z. Ning, Interplay of various loss mechanisms and ultimate size limit of a surface plasmon polariton semiconductor nanolaser, *Opt. Express* 20, 16348–16357, (2012).

- 
- [51] J. B. Khurgin, and G. Sun, Practicality of compensating the loss in the plasmonic waveguide using semiconductor gain medium, *Appl. Phys. Lett.* 100, 011105 (1–3), (2012).
- [52] X. Chen, B. Bhola, Y. Huang, and S. T. Ho, Multi-level multi-thermal-electron FDTD simulation of plasmonic interaction with semiconducting gain media: applications to plasmonic amplifiers and nanolasers. *Opt. Express* 18, 17220–17238, (2010).
- [53] Z. Yu, G. Veronis, S. Fan, and M. L. Bongersma, Gain-induced switching in metal- dielectric-metal plasmonic waveguides, *Appl. Phys. Lett.* 92, 041117 (1–3), (2008).
- [54] M. T. Hill, M. Marell, E. S. P. Leong, B. Smalbrugge, Y. Zhu, M. Sun, P. J. vanVeldhoven, E. J. Geluk, F. Karouta, Y. S. Oei, R. Nötzel, C. Z. Ning, and M. K. Smit, Lasing in metal-insulator-metal sub-wavelength plasmonic waveguides. *Opt. Express* 17, 11107–11112, (2009).
- [55] M. Z. Alam, J. Meier, J. S. Aitchison, and M. Mojahedi, Gain assisted surface plasmon polariton in quantum well structures. *Opt. Express* 15, 176–182, (2007).
- [56] Y. H. Chen, and L. J. Guo, High Q long-range surface plasmon polariton modes in sub-wavelength metallic microdisk cavity, *Plasmonics* 6, 183–188, (2011).
- [57] M. Ambati, D. A. Genov, R. F. Oulton, and X. Zhang, Active plasmonics: surface plasmon interaction with optical emitters. *IEEE J. Sel. Top. Quan. Elec.* 14, 1395–1403, (2008).
- [58] S. Kéna-Cohen, P. N. Stavrinou, D. D. C. Bradley, and S. A. Maier, Confined surface plasmon polariton amplifiers, *Nano Lett.* 13, 1323–1329, (2013).
- [59] R. A. Flynn, C. S. Kim, I. Vurgaftman, M. Kim, J. R. Meyer, A. J. Mäkinen, K. Bussmann, L. Cheng, F. S. Choa, and J. P. Long, A room-temperature semiconductor spaser operating near 1.5  $\mu\text{m}$ , *Opt. Express* 19, 8954–8961, (2011).
- [60] J. Grandidier, G. Colas des Francs, S. Massenot, A. Bouhelier, L. Markey, J. C. Weeber, C. Finot, and A. Dereux, Gain-assisted propagation in a plasmonic waveguide at telecom wavelength, *Nano Lett.* 9, 2935–2939, (2009).
- [61] J. Grandidier, G. Colas des Francs, S. Massenot, A. Bouhelier, L. Markey, J. C. Weeber, C. Finot, and A. Dereux, Leakage radiation microscopy of surface plasmon coupled emission: investigation of gain-assisted propagation in an integrated plasmonic waveguide. *J. Microsc.* 239, 167–172, (2010).
- [62] C. Garcia, V. Coello, Z. Han, I. P. Radko, and S. I. Bozhevolnyi, Partial loss compensation in dielectric-loaded plasmonic waveguides at near-infra-red wavelengths. *Opt. Express* 20, 7771–7775, (2012).
- [63] G. Colas Des Francs, P. Bramant, J. Grandidier, A. Bouhelier, J. C. Weeber, and A. Dereux, Optical gain, spontaneous and stimulated emission of surface plasmon polaritons in confined plasmonic waveguide, *Opt. Express* 18, 16327–16334, (2010).
- [64] R. Rao, and T. Tang, Study on active surface plasmon waveguides and design of a nanoscale lossless surface plasmon waveguide, *J. Opt. Soc. Am. B* 28, 1258–1265, (2011).
- [65] C. Hahn, S. H. Song, C. H. Oh, and P. Berini, Single-mode lasers and parity-time symmetry broken gratings based on active dielectric-loaded long-range surface plasmon polariton waveguides, *Opt. Express* 23, 19922–19931, (2015).

- 
- [66] M. Z. Alam, J. Meier, J. S. Aitchison, and M. Mojahedi, Super mode propagation in low index medium, Proc. CLEO, JThD112, (2007).
- [67] R. F. Oulton, V. J. Sorger, D. A. Genov, D. F. P. Pile, and X. Zhang, A hybrid plasmonic waveguide for subwavelength confinement and long-range propagation. Nat. Photonics 2, 496–500, (2008).
- [68] R. F. Oulton, G. Bartal, D. F. P. Pile, and X. Zhang, Confinement and propagation characteristics of subwavelength plasmonic modes, New J. of Phys. 10, 105018 (1-14), (2008).
- [69] R. F. Oulton, V. J. Sorger, T. Zentgraf, R. M. Ma, C. Gladden, L. Dai, G. Bartal, and X. Zhang, Plasmon lasers at deep subwavelength scale, Nature 461, 629–632, (2009).
- [70] R. M. Ma, R. F. Oulton, V. J. Sorger, G. Bartal, G., and X. Zhang, Room-temperature subdiffraction-limited plasmon laser by total internal reflection, Nat. Mater. 10, 110–113, (2011).
- [71] R. M. Ma, X. Yin, R. F. Oulton, V. J. Sorger, and X. Zhang, Multiplexed and electrically modulated plasmon laser circuit. Nano Lett. 12, 5396–5402, (2012).
- [72] Y. J. Lu, J. Kim, H. Y. Chen, C. Wu, N. Dabidian, C. E. Sanders, C. Y. Wang, M. Y. Lu, B. H. Li, X. Qiu, W. H. Chang, L. J. Chen, G. Shvets, C. K. Shih, and S. Gwo, Plasmonic nanolaser using epitaxially grown silver film. Science 337, 450–453, (2012).
- [73] T. P. H. Sidiropoulos, R. Röder, S. Geburt, O. Hess, S. A. Maier, C. Ronning, and R. F. Oulton, Ultrafast plasmonic nanowire lasers near the surface plasmon frequency, Nature Physics 10, 870–876, (2014).
- [74] Y. Li, and W. P. Huang, Electrically-pumped plasmonic lasers based on low-loss hybrid SPP waveguide, Opt. Express 23, 24843–24849, (2015).
- [75] K. L. Kelly, E. Coronado, L. L. Zhao, and G. C. Schatz, The optical properties of metal nanoparticles: the influence of size, shape, and dielectric environment. J. Phys. Chem. B 107, 668–677, (2003).
- [76] M. Pelton, J. Aizpurua, and G. Bryant, Metal-nanoparticle plasmonics. Laser Phot. Rev. 2, 136–159, (2008).
- [77] D. J. Bergman, and M. I. Stockman, Surface plasmon amplification by stimulated emission of radiation: quantum generation of coherent surface plasmons in nanosystems, Phys. Rev. Lett. 90, 027402 (1–4), (2003).
- [78] M. I. Stockman, Spasers explained, Nat. Photonics 2, 327–329, (2008).
- [79] M. A. Noginov, G. Zhu, A. M. Belgrave, R. Bakker, V. M. Shalaev, E. E. Narimanov, S. Stout, E. Herz, T. Suteewong, and U. Wiesner, Demonstration of a spaser-based nanolaser. Nature 460, 1110–1113, (2009).
- [80] X. Meng, A. V. Kildishev, K. Fujita, K. Tanaka, and V. M. Shalaev, Wavelength-tunable spasing in the visible, Nano Lett. 13, 4106–4112, (2013).
- [81] J. B. Khurgin, and G. Sun, How small can “Nano” be in a “Nanolaser?” Nanophotonics 1, 3–8, (2012).

- 
- [82] K. E. Dorfman, P. K. Jha, D. V. Voronine, P. Genevet, F. Capasso, and M. O. Scully, Quantumcoherence-enhanced surface plasmon amplification by stimulated emission of radiation. *Phys. Rev. Lett.* 111, 043601 (1–5), (2013).
- [83] P. Ginzburg, and A. V. Zayats, Linewidth enhancement in spasers and plasmonic nanolasers. *Opt. Express* 21, 2147–2153, (2013).
- [84] N. M. Lawandy, Localized surface plasmon singularities in amplifying media. *Appl. Phys. Lett.* 85, 5040–5042, (2004).
- [85] J. A. Gordon, and R. W. Ziolkowski, The design and simulated performance of a coated nano-particle laser, *Opt. Express* 15, 2622–2653, (2007).
- [86] Z. Y. Li, and Y. Xia, Metal nanoparticles with gain toward single-molecule detection by surface-enhanced Raman scattering, *Nano Lett.* 10, 243–249, (2010).
- [87] J. Y. Suh, C. H. Kim, W. Zhou, M. D. Huntington, D. T. Co, M. R. Wasielewski, and T. W. Odom, Plasmonic bowtie nanolaser arrays. *Nano Lett.* 12, 5769–5774, (2012).
- [88] W. Zhou, M. Dridi, J. Y. Suh, C. H. Kim, D. T. Co, M. R. Wasielewski, G. Schatz, and T. W. Odom, Lasing action in strongly coupled plasmonic nanocavity arrays. *Nat. Nanotechnol.* 8, 506–511, (2013).
- [89] R. Marani, A. D’Orazio, V. Petruzzelli, S. G. Rodrigo, L. Martin-Moreno, F. J. Garcia-Vidal, and J. Bravo-Abad, Gain-assisted extraordinary optical transmission through periodic arrays of subwavelength apertures, *New J. Phys.* 14, 013020 (1–16), (2012).
- [90] F. van Beijnum, P. J. van Veldhoven, E. J. Geluk, M. J. A. de Dood, G. W. ’t Hooft, and M. P. van Exter, Surface plasmon lasing observed in metal hole arrays, *Phys. Rev. Lett.* 110, 206802 (1–5), (2013).
- [91] X. Meng, J. Liu, A. V. Kildishev, and V. M. Shalaev, Highly directional spaser array for the red wavelength region, *Laser Photonics Rev.* 8, 896–903 (2014).
- [92] E. K. Keshmarzi, R N. Tait, and P. Berini, Long-range surface plasmon single-mode laser concepts, *Journal of Applied Physics* 112, 063115, (2012).
- [93] A. J. C. Kuehne, and M. C. Gather, Organic Lasers: Recent Developments on Materials, Device Geometries, and Fabrication Techniques, *Chem Rev.* 116(21),12823-12864, (2016).
- [94] E. K. Keshmarzi, R. N. Tait, and P. Berini, Near infrared amplified spontaneous emission in a dye-doped polymeric waveguide for active plasmonic applications, *Opt. Express* 22, 12452–12460, (2014).
- [95] E. K. Keshmarzi, R N. Tait, and P. Berini, Spatially nonreciprocal Bragg gratings based on surface plasmons, *Applied Physics Letters* 105, 191110, (2014).
- [96] E. K. Keshmarzi, R N. Tait, and P. Berini, Parity-time symmetry-broken Bragg grating operating with long-range surface plasmon polaritons, *Applied Physics A* 122 (4), 1-5, (2016).